A Modelling and Imaging Approach to Further Understanding of Pathophysiology in Arrhythmogenic Cardiomyopathy

Peter Marinov

St Hugh's College

University of Oxford

A thesis submitted for the degree of

Master of Research in Computer Science

Michaelmas Term 2020

This thesis is dedicated to the ones who stimulated my enlightenment.

Acknowledgements

I thank my loving girlfriend for her support during the thesis writing, my parents for financial assistance, my broader family and friends for giving me motivation and my supervisors for providing the direction of the research.

Abstract

Background: Arrhythmogenic Cardiomyopathy (ACM) is a potentially lethal form of cardiomyopathy, with a high incidence of mortality. It is prominently characterised by abnormal ventricular anatomy, fibrofatty replacement of the myocardium and the His-Purkinje system, as well as electrophysiological remodelling. It remains unknown how the broad spectrum of ACM-related co-morbidities alter the 12 lead electrogram (ECG). Ventricular activation abnormalities result in QRS complex and terminal activation duration prologation, as well as abnormal R-wave progression and low amplitude signals are diagnosis criteria of ACM on the 12-lead ECG. The pathological remodelling leading to the above electrocardiographic findings can be of electrical, geometrical or structural nature or a combination of substrates. Diagnosis of this clinical entity is challenging and relies on a combination of ECG, non-invasive imaging approaches to access myocardial muscle structrure and geometry as well as genetic testing. Despite the multi-modality diagnosis approach, misdiagnosis is common and some patients are not diagnosed until post-mortem examination is performed. Improvements in diagnosis are much needed and one challenge is understanding the link between ECG manifestations and underlying disease burden. Furthermore, no ACM specific treatments exist to date and life quality of sufferers is greatly reduced as cardiac defibrillators and guidelines to avoid physical activity are the treament norm. Obtaining an accurate diagnosis non-invasively can contribute to better risk stratification and patient management, ultimately improving the life quality and safety of patients.

Aims: It is known that several mechanisms can lead to slow electrical conduction in the ventricles of ACM patients. Plausible single cell electrophysiological mechanisms, such as co-modulation of I_{Na}-I_{K1} ionic channels, leading to tissue level electrical conduction velocity modulation in ACM are explored. This thesis aims to uncover which mechanisms of

conduction slowing prevail in patients with ACM by integrating information from imaging data and performing personalised activation sequence simulations of patients diagnosed with ACM. The scope is to also relate the different conduction abnormalities to signature traits on the ECG, so as to help refine diagnosis and disease burden non-invasively.

Methods: The effect of ACM specific ionic channel joint reduction of conduction is explored via a study relating co-modulation in key ionic channels (I_{Na}-I_{K1}) [1], known to be remodelled in ACM variants[2] and the tissue level electrical conduction velocity in 2D tissue simulations. Personalised models of electrical conduction are created from Magnetic Resonance Imaging (MRI) data of a cohort of ACM patients with 15 definite, 3 borderline and 2 plausible patients according to the 2010 international diagnosis guidelines [3]. Patient ventricular and torso anatomies are extracted from the MRI images and regional fibrotic scar information is extracted from contrast agent enhanced MRI imaging. Different types of remodelling were introduced into graph-based models of sinus rhythm activation, namely localised fibrosis-mediated conduction slowing in the myocardial muscle or in the Purkinje-myocardial fast conduction system, myocardial tissue uncoupling leading to global ventricular tissue conduction slowing, right ventricular (RV) muscle disappearance leading to slowed conduction localised in the RV, RV muscle volume dilation and RV wall thinning. Insights from slab tissue simulations were used to estimate the order of magnitude of conduction velocity modulation due to ionic remodelling, clinical data (contrast enhanced MRI) for scar based conduction anomalies and from other computational studies quantifying conduction velocity modulation in the ACM myocardium [4] were used to find physiological parameter intervals for the computational study. The effects of the above types of remodelling on features of the ECG relating to activation dynamics were quantified.

Results: Slab tissue simulations revealed that ACM-specific ionic remodelling of the I_{Na}-I_{K1} macromolecular complex can result in up to 45% bulk myocardial tissue CV modulation. A computational pipeline was adapted to access the effect of ACM ventricular substrates on conduction properties of the ventricles. The personalised data-driven models of two ACM patients with varying disease burden were used to successfully explain how the underlying whole ventricular remodelling impacted

the clinical patients' ECG recordings. Computer simulations demonstrate that, in ACM, mild QRS prolongation ($>$100 ms), in absence of other QRS abnormalities, is explained by regional myocardial conduction slowing in the areas of MRI-identified fibrosis. However, MRI-segmented myocardial fibrosis and RV dilation alone proved insufficient to recapitulate more severe QRS abnormalities, such as severely prolonged mean QRS duration ($>$120 ms) across precordial leads, mean terminal activation duration across V1-V4 ($>$55 ms), and low QRS mean R-wave amplitude ($<$2 mV) in precordial leads, as well as poor R-wave progression across precordial leads. A 70% decrease in Purkinje-endocardial conduction and 30% RV wall thinning were additionally required to explain these more severe abnormalities.

List of Publications

- Rate Dependence of the INa-IK1 Complex on Human Ventricular Conduction Velocity under Hypokalemia and Hyperkalemia Conditions (conference publication Cinc 2017) Peter Marinov, Blanca Rodriguez, Alfonso Bueno-Orovio

- "MRI-informed modelling and simulation highlight the role of Purkinje and fibrosis on QRS abnormalities in Arrhythmogenic Cardiomyopathy" (in preparation) Peter Marinov, Julià Camps, Ana Mincholé, Ernesto Zacur, Michele Orini, Pier D Lambiase, Stefania Rosmini, Neil Srinivasan, James Moon, Pyotr Platonov, Vicente Grau, Alfonso Bueno-Orovio, Blanca Rodriguez

Contents

Chapter 1

Introduction

In this chapter, the relevant biological concepts underpinning and motivating this work, as well as ACM, the disease of interest, are presented. The evolution of the clinical disease in time is followed by the basic functioning of the heart and the role of ventricular electrophysiology in determining the action potential and maintaining electrical conduction. Then, the ways in which ACM changes ventricular electrophysiology are explained with reference to known genetic mutations leading to the experimentally observed disease manifestations. Hence, a link between extracellular level mechanisms and global structural alterations to the cardiac muscle properties is presented in the context of known genetic mutations of ACM. Finally, the causes of conduction slowing, leading to abnormal ventricular electrical activation found in this disease are summarised.

1.1 Arrhythmogenic Cardiomyopathy - A novel clinical entity

1.1.1 Historical Perspective of the clinical evolution of Arrhythmogenic Cardiomyopathy

Medical practice has continuously updated the definition of the clinical entity of interest, with its currently accepted name being Arrhythmogenic Cardiomyopathy. Back in the 1980s [5], the first reports by clinical doctors were of a muscle disease affecting the right ventricle, ultimately leading to muscle damage and lethal ventricular arrhythmias. Since then, numerous genetic and developmental factors have been outlined and the clinical entity has evolved to encompass both ventricles. Strict diagnosis criteria have been proposed in 1994, which were then updated in 2010 and 2019 respectively. The progression has been towards finding patient subpopulations

and classifying patients in risk categories, based on an extensive, non-invasive clinical examination. Clinical attention has shifted from the right ventricle only to a bi-ventricular disease, whereby either of the two ventricles can be remodelled and an arrhythmic subsrate can be a result of muscle degradation and subsequent fibro-fatty replacement. The name has evolved from Right Ventricular Dysplasia [5] to Arrhythmogenic Right Ventricular Cardiomyopathy (ARVC) [6] to the current name Arrhythmogenic Cardiomyopathy ([7].

1.1.2 ARVC - A right ventricular dominant clinical entity

Sometimes the literature mentions the name Arrhythmogenic Right Ventricular Cardiomyopathy, when referring to a heart disorder that primarily manifests itself in the right ventricle in humans. It affects the muscle tissue in the heart, also known as myocardial tissue. It is characterised by a progressive decoupling of the myocyte network. As a result, micro disarrangements, fatty replacement and fibrosis characterise the muscle tissue and create a pro-arrhythmic layer. Thus, ARVC can lead to ventricular tachycardias, ventricular arrhythmias and/or sudden cardiac death [8] [9] [10]. ARVC is a silent killer as micro-scale structural and localised electrophysiological abnormalities are often not visible in clinical examinations and these can be sufficient to lead to lethal arrhythmias or sudden cardiac death (SCD) in certain patients [11] [12] [5] [13]. In particular, young patients and athletes are at high risk [13] [14]. It is worth noting that ARVC is known as Arrhythmic Right Ventricular Dysplasia in the US. ACM prevalence is between 1:2000 and 1:5000 in the general public in the US [15] and affects men more frequently than women, with a ratio of 2.4:1 [16]. The disease has no specific racial or geograghical predisposition

The disease is diagnosed universally according to the 2010 task force criteria [3], which build and refine the 1994 criteria [6]. A comparison of the criteria as they stood in 1994 and their update in 2010 [3] is included in table 1.1 and 1.2. The most typical clinical diagnosis has 2 main scenarios: (1) electro-cardiographic abnormalities, typically a ventricular tachycardia with left bundle branch morphology and T-wave inversion in leads V1-V3 (2) functional and structural abnormalities mostly of the RV, such as wall thinning, regional wall motion alterations and global dilation. The disease is clinically heterogeneous, occurring with inter-famillial and intra-famillial variability. The left ventricle is frequently involved in the disease and hence ACM is a more useful clinical name for this disease [17]. This is an umbrella term, used to describe both arrhythmogenic left ventricular cardiomyopathy and right sided manifestations of disease. This new clinical entity is currently under investigation, with

leading clinicians currently developing novel scoring systems for diagnosis based on MRI, ECG, histology and genetics [18] [19]. In this thesis, the nomenclature ACM will be used throughout except for in cases when the observations are solely valid for the right ventricular manifestation of disease.

1.2 Basic Function of the Heart

The heart is a mechanical pump and is used to pump blood around the circulation system [20]. This is achieved by the heart muscle doing active work on the blood in the chambers of the heart. The heart is separated in two atrial chambers used for filling and two ventricular chambers used for pumping the blood into the two major arteries. In order to achieve muscle contraction, a wave of electricity propagates along the heart muscle. Physiological propagation occurs when the stimulus is dictated by the right atrial sinus node pacemaker and by the atrio-ventricular node for the ventricles. The atrial node cells have automaticity, meaning they are self-excitng [21]. The propagation then descends the Purkinje network of fibers, which is connected to the endocardium of the ventricles and from there proceeds to reach all parts of the ventricular muscle. This process is illustrated in Figure 1.3. On the mechanical side, atrial contraction pumps blood into the ventricles, which in turn apply pressure to pump it into the Pulmonary artery and the Aorta in a coordinated and timely manner. Once the contraction of the whole heart has been triggered by the electrical stimulus, the heart enters in a relaxation stage when the atrial chambers refill as the four chambers regain their end of contraction volume, also known as the diastolic volume.

The propagation of the electrical wave through the heart muscle, also known as the myocardium, is maintained by a flow of ions between the cardiac muscle cells via a coupling structure known as the gap junction [23]. Heart muscle cells are arranged in fibres [24]. There is intrinsic anisotropy in heart muscle fiber propagation speed. This arises as electrical conduction speed along the fiber direction is higher than speed along the transverse or interfiber directions. As the electrical impulse travels from cell to cell, it causes a cyclic change of ionic concentrations, which give rise to the action potential, a potential difference of the cell with respect to the extracellular space [25].

3

Original Task Force Criteria	Revised Task Force Criteria
I. Global or regional dysfunction and structural alterations*	
Major	
	By 2D echo:
	• Regional RV akinesia, dyskinesia, or aneurysm
• Severe dilatation and reduction of RV ejection fraction with no (or only mild) LV impairment	• *and* 1 of the following (end diastole):
	— PLAX RVOT ≥32 mm (corrected for body size [PLAX/BSA] ≥19 mm/m^2)
• Localized RV aneurysms (akinetic or dyskinetic areas with diastolic bulging)	— PSAX RVOT ≥36 mm (corrected for body size [PSAX/BSA] ≥21 mm/m^2)
• Severe segmental dilatation of the RV	— *or* fractional area change ≤33%
	By MRI:
	• Regional RV akinesia or dyskinesia or dyssynchronous RV contraction
	• *and* 1 of the following:
	— Ratio of RV end-diastolic volume to BSA ≥110 mL/m^2 (male) or ≥100 mL/m^2 (female)
	— *or* RV ejection fraction ≤40%
	By RV angiography:
	• Regional RV akinesia, dyskinesia, or aneurysm
Minor	
	By 2D echo:
• Mild global RV dilatation and/or ejection fraction reduction with normal LV	• Regional RV akinesia or dyskinesia
	• *and* 1 of the following (end diastole):
	— PLAX RVOT ≥29 to <32 mm (corrected for body size [PLAX/BSA] ≥16 to <19 mm/m^2)
• Mild segmental dilatation of the RV	— PSAX RVOT ≥32 to <36 mm (corrected for body size [PSAX/BSA] ≥18 to <21 mm/m^2)
• Regional RV hypokinesia	— *or* fractional area change >33% to ≤40%
	By MRI:
	• Regional RV akinesia or dyskinesia or dyssynchronous RV contraction
	• *and* 1 of the following:
	— Ratio of RV end-diastolic volume to BSA ≥100 to <110 mL/m^2 (male) or ≥90 to <100 mL/m^2 (female)
	— *or* RV ejection fraction >40% to ≤45%
II. Tissue characterization of wall	
Major	
• Fibrofatty replacement of myocardium on endomyocardial biopsy	• Residual myocytes <60% by morphometric analysis (or <50% if estimated), with fibrous replacement of the RV free wall myocardium in ≥1 sample, with or without fatty replacement of tissue on endomyocardial biopsy
Minor	
	• Residual myocytes 60% to 75% by morphometric analysis (or 50% to 65% if estimated), with fibrous replacement of the RV free wall myocardium in ≥1 sample, with or without fatty replacement of tissue on endomyocardial biopsy
III. Repolarization abnormalities	
Major	
	• Inverted T waves in right precordial leads (V$_1$, V$_2$, and V$_3$) or beyond in individuals >14 years of age (in the absence of complete right bundle-branch block QRS ≥120 ms)
Minor	
• Inverted T waves in right precordial leads (V$_2$ and V$_3$) (people age >12 years, in absence of right bundle-branch block)	• Inverted T waves in leads V$_1$ and V$_2$ in individuals >14 years of age (in the absence of complete right bundle-branch block) or in V$_4$, V$_5$, or V$_6$
	• Inverted T waves in leads V$_1$, V$_2$, V$_3$, and V$_4$ in individuals >14 years of age in the presence of complete right bundle-branch block

(*Continued*)

Figure 1.1: The 1994 and 2010 task force criteria for the diagnosis of ACM. The adaptation incorporates the newest imaging techniques in the process of diagnostics.

Original Task Force Criteria	Revised Task Force Criteria
IV. Depolarization/conduction abnormalities	
Major	
• Epsilon waves or localized prolongation (>110 ms) of the QRS complex in right precordial leads (V_1 to V_3)	• Epsilon wave (reproducible low-amplitude signals between end of QRS complex to onset of the T wave) in the right precordial leads (V_1 to V_3)
Minor	
• Late potentials (SAECG)	• Late potentials by SAECG in ≥1 of 3 parameters in the absence of a QRS duration of ≥110 ms on the standard ECG
	• Filtered QRS duration (fQRS) ≥114 ms
	• Duration of terminal QRS <40 μV (low-amplitude signal duration) ≥38 ms
	• Root-mean-square voltage of terminal 40 ms ≤20 μV
	• Terminal activation duration of QRS ≥55 ms measured from the nadir of the S wave to the end of the QRS, including R′, in V_1, V_2, or V_3, in the absence of complete right bundle-branch block
V. Arrhythmias	
Major	
	• Nonsustained or sustained ventricular tachycardia of left bundle-branch morphology with superior axis (negative or indeterminate QRS in leads II, III, and aVF and positive in lead aVL)
Minor	
• Left bundle-branch block-type ventricular tachycardia (sustained and nonsustained) (ECG, Holter, exercise)	• Nonsustained or sustained ventricular tachycardia of RV outflow configuration, left bundle-branch block morphology with inferior axis (positive QRS in leads II, III, and aVF and negative in lead aVL) or of unknown axis
• Frequent ventricular extrasystoles (>1000 per 24 hours) (Holter)	• >500 ventricular extrasystoles per 24 hours (Holter)
VI. Family history	
Major	
• Familial disease confirmed at necropsy or surgery	• ARVC/D confirmed in a first-degree relative who meets current Task Force criteria
	• ARVC/D confirmed pathologically at autopsy or surgery in a first-degree relative
	• Identification of a pathogenic mutation[†] categorized as associated or probably associated with ARVC/D in the patient under evaluation
Minor	
• Family history of premature sudden death (<35 years of age) due to suspected ARVC/D	• History of ARVC/D in a first-degree relative in whom it is not possible or practical to determine whether the family member meets current Task Force criteria
• Familial history (clinical diagnosis based on present criteria)	• Premature sudden death (<35 years of age) due to suspected ARVC/D in a first-degree relative
	• ARVC/D confirmed pathologically or by current Task Force Criteria in second-degree relative

PLAX indicates parasternal long-axis view; RVOT, RV outflow tract; BSA, body surface area; PSAX, parasternal short-axis view; aVF, augmented voltage unipolar left foot lead; and aVL, augmented voltage unipolar left arm lead.

Diagnostic terminology for original criteria: This diagnosis is fulfilled by the presence of 2 major, or 1 major plus 2 minor criteria or 4 minor criteria from different groups. Diagnostic terminology for revised criteria: definite diagnosis: 2 major or 1 major and 2 minor criteria or 4 minor from different categories; borderline: 1 major and 1 minor or 3 minor criteria from different categories; possible: 1 major or 2 minor criteria from different categories.

*Hypokinesis is not included in this or subsequent definitions of RV regional wall motion abnormalities for the proposed modified criteria.

†A pathogenic mutation is a DNA alteration associated with ARVC/D that alters or is expected to alter the encoded protein, is unobserved or rare in a large non-ARVC/D control population, and either alters or is predicted to alter the structure or function of the protein or has demonstrated linkage to the disease phenotype in a conclusive pedigree.

Figure 1.2: The 1994 and 2010 task force criteria for the diagnosis of ACM. The adaptation incorporates the newest imaging techniques in the process of diagnostics.
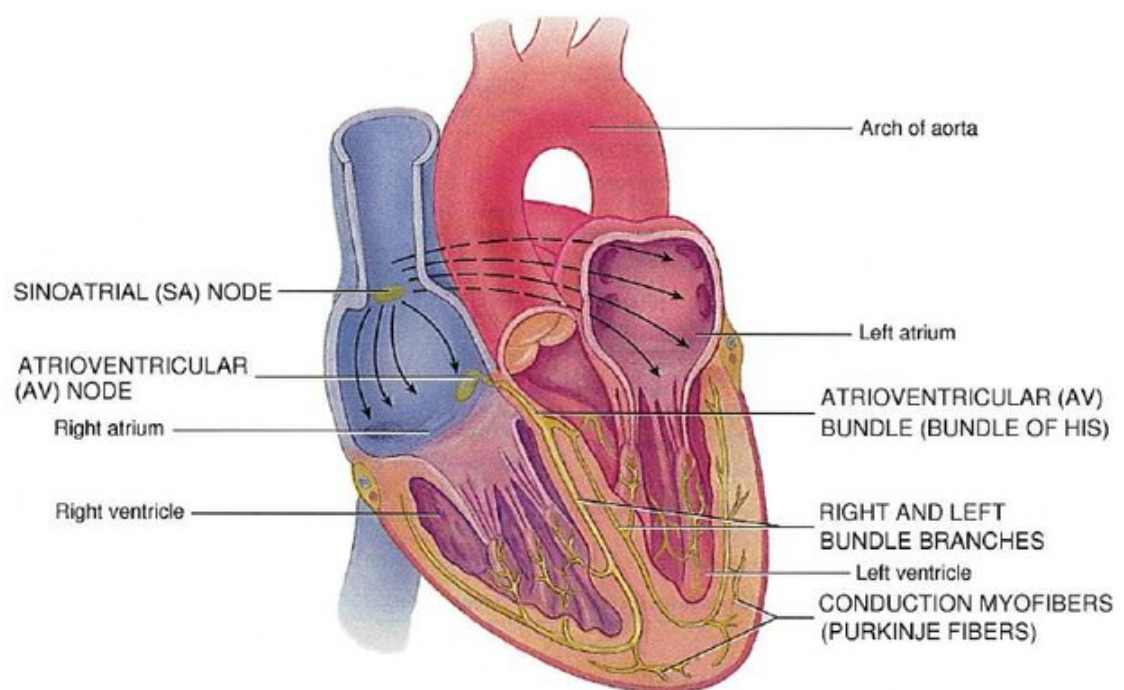
Figure 1.3: The principal components generating and carrying an electrical impulse throughtout the heart are shown, along with the four chambers of the heart [22].

1.3 Single cell-level mechanisms of electrical conduction

1.3.1 Cardiac Action Potential

The electrical wave of excitation illicits a cyclic change in the ionic concentrations of key ions in the cardiac muscle cell or myocyte. More specifically in the ventricles, this generates a cell action potential (AP) with a characteristic curve, as outlined in Figure 1.4. The ventricular myocytes undergo a distinct 4-phase cycle:

- **Phase 0** Upstroke or otherwise known as rapid depolarisation. The membrane voltage shifts to a positive value of +40mV from close to -90mV in resting state as positive ions, Na^+ and Ca^{2+} enter the cell through voltage-gated ion channels.

- **Phase 1** Early rapid repolarisation through the opening of potassium repolarising channels.

- **Phase 2** A plateau phase, dependant on balance of inward Ca^{2+} channels and outward repolarising channels.

- **Phase 3** Final repolarisation that brings membrane potential to its resting, negative value.

- **Phase 4** Resting potential of approximately -90 mV.

The electrical wave first leads to depolarisation comprises of ion dynamics entering the cell is governed by a cascade of channels, initiated by the rapid outward Na^+ channel.

The Na$^+$ Channel

As the neighboring cell depolarises, the potential of the current cell increases to above its resting value of -90 mV as an inward fast Na$^+$, or NaV1.5 channel opens and thus increases the cell's potential further, until the threshold value of -70 mV is reached and a self sustaining inward fast Na$^+$ current onsets. The large Na$^+$ current rapidly brings the trans-membrane potential (TMP) to about 0 mV for a transient period of time called the overshoot. L-type Ca^{2+} open at -40 mV and initiate the calcium cycle described in Section 1.3.1. The fast Na$^+$ channel opening is responsible for the initial upstroke in the action potential, as shown in Figure 1.4. This channel also has a role in conduction velocity modulation, as discussed later in this chapter and in the simulations in Chapter 2.
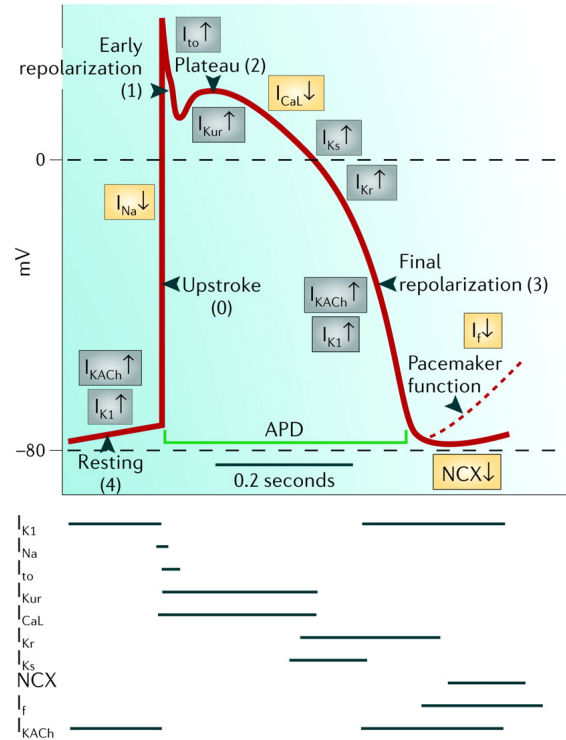
Figure 1.4: A cardiac muscle cell's major ionic currents are responsible for the action potential shape [26], including the delayed rectifier potassium current (I_{K1}), the sodium channel (I_{Na}), the L-type calcium current (I_{CaL}), the transient outward potassium channel (I_{to}), the ultra rapid potassium channel (I_{Kur}), the delayed potassium current I_{Kr}, the sodium-calcium exchanger (NCX), the funny current (I_f) and the muscarinic potassium channel (I_{KCh}).

The characteristic AP curve varies across the myocardial wall. There is disagreement in the literature about the exact pattern governing myocardial AP variability but gradients in the duration of phases 1, 2 and 3 have been observed experimentally [27][28], whilst later wstudies claim that no significant repolarisation gradients exist within a healthy myocardium [29]. The duration of the cardiac muscle cell cycle plays a vital role in arrhythmia initiation and maintenance, especially in the context of AP heterogeneity across one or several of the heart's chambers.

The Calcium Cycle

When a neighbouring cell is excited, the associated potential gradient causes an influx of Ca^{2+} into the T-tubules of the currently resting cell. The voltage gated Ca^{2+} channel opens in the cellular membrane of the tubules and calcium enters the cell. Ca^{2+} induced Ca^{2+} release occurs via the ryanodine receptor channels (RYR2)

[30]. These extra calcium ions rapidly leave the sarcoplasmic reticulum (SR), where they are stored internally to the cell. The abundance of calcium in the cell binds to the troponin and initiates muscle contraction through shorterning of the sarcomeres. Muscle relaxation occurs as Ca^{2+} unbinds from troponin. Ca^{2+} is transferred back into the SR via a Ca^{2+} ATPase, at the expense of ATP hydrolysis. This hydrolysis transforms chemical energy, stored as phosphoanhydride chemical composition, into useful mechanical work. Calcium is stored in the SR until the next contraction. To further reduce the concentration of Ca^{2+}, the remaining intra-cellular Ca^{2+} is exchanged with Na^+ via the sodium-calcium exchanger. As 3 Na^+ ions enter for every expelled Ca^{2+}, this contributes to a buildup of a net positive Ca^{2+} inward gradient of the cell with respect to the extracellular space. Finally, the Na^+ gradient is controlled via the sodium-potassium pump. Na^+/ K^+ pump is a solute pump that pumps Na^+ out and K^+ in, against their concentration gradients. The intracellular Na^+ concentration needs to be smaller than the extracellular Na^+ concentration during resting state, as the inward Na^+ current plays an important role in initiation of muscle contraction [31]. A schematic of the processes above is shown in Figure 1.5.
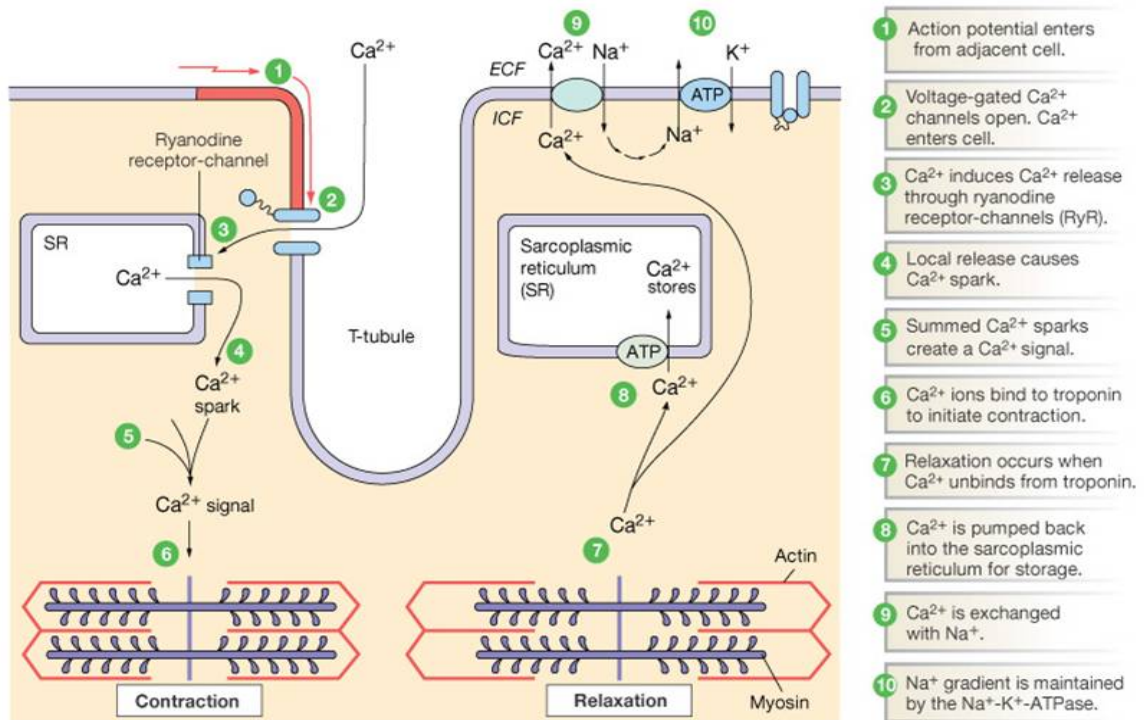
Figure 1.5: The calcium ion cycle is central to the governance of muscle contraction and relaxation. There is an interplay between the difference in the relative intra-cellular and extracellular Ca^{2+} concentrations. This illustration is reproduced with permission from Chapter 9 of the Human Physiology : from cells to systems [32].

T-Type Calcium and L-Type Calcium channels

The L-type calcium channel has a long lasting activation in a cardiac cycle and is part of the high voltage activated family of channels. It is the link between excitation and contraction of myocytes. The inward flow of ions into the cell is responsible for triggering the RYR2 receptor on the SR [33]. Phosphorylation of this channel increases its permeability and consequently the myocyte contractility.

The T-type Ca^{2+} opening is responsible for initiating L-type calcium channels opening and is transient in nature [32]. It opens during membrane depolarisation, mediating Ca^{2+} ion influx via the cell membrane. The T-type channel is activated in the same voltage range as the voltage-gated Na$^+$ channel, at about -55 mV. The large potential gradient induces a considerable flow of ions into the cell. This channel is regulated by dopamine and other neurotransmitters, which block T-type currents [34].

The Ryanodine Receptor 2 channel (RYR2)

RYR2 is a protein involved in the process of Ca^{2+} induced Ca^{2+} release in myocytes. It opens during systole and is located on the SR. It is activated by the binding process of Ca^{2+} to the SR wall, with Ca^{2+} receptors governing the channel open and closed states [35]. Their activation is Ca^{2+} gated and their opening rate and duration is dependent on the intracellular Ca^{2+} concentration.

The Na$^+$/K$^+$ATPase Pump

The resting state potential of the cell is maintained at -90 mV and is controlled by potassium ion dynamics. The Na$^+$/K$^+$ATPase pump moves 2 K$^+$ in and 3 Na$^+$ out at each cycle [36]. It thus contributes to generating a negative resting cell potential by creating an effective outward current, whilst building up a positive K$^+$ gradient between the cell and its surroundings. In the short term, more K$^+$ will exit the cell via this gradient than will enter. A negative trans-membrane voltage grows. This process also builds a negative Na$^+$ gradient across the cell membrane.

Voltage Gated K$^+$ Channels

Voltage-gated K$^+$ channels are trans-membrane channels that respond to voltage changes across the myocyte membrane.

Transient Outward I$_{to}$

It contributes to early repolarisation phase 1 of the AP by moving intracellular K$^+$ to the extracellular space. It has rapid activation and deactivation [37]. It is activated as a result of the fast increase in membrane potential in phase 0.

Ultra Rapid Potassium Channel I$_{Kur}$

This ultra rapid outward channel opens in the plateau phase 2 of the AP [38]. It plays an important role in determining the contractility of the atrium but not that of the ventricles.

Delayed Rectifier I_{Kr}

The delayed potassium rectifier helps to repolarise the cell by expelling K^+ ions from the cell in phase 3. It is activated by the influx of Na^+ during upstroke. It contributes to defining the shape of the plateau in the AP.

Inwardly rectifying potassium channel I_{K1}

This inward rectifying current stabilises the resting membrane potential and switches on during the initial depolarisation and final repolarisation of the AP. Inwardly rectifying K^+ channels conduct ions into the cell at potentials more negative than the Nernst potential, which is the equilibrium potential of this channel, E_K. At equilibrium, the diffusion gradient across the cell membrane exactly opposes the electrical charge density within the cell and thus no charge flows through the channel. By doing so, they contribute to stabilising the resting cell potential of the cell. These inward rectifiers also conduct less outward current, when $V > E_K$, than traditional voltage gated channels.

Na^+/Ca^{2+} Exchanger

The sodium-calcium exchanger, or NCX, is an exchanger protein which removes calcium from the myocyte. It uses the energy stored in the eletrochemical gradient of Na^+, which is built up at the beginning of the AP [39]. This protein takes advantage of the high extracellular concentration of Na^+ and allows Na^+ to diffuse into the cell, in exchange for Ca^{2+} ions out, in the ratio 3:1. Thus, a net increase of positive charge in the cell occurs via this mechanism.

ATP-Sensitive K^+ Channel

K_{ATP} is a potassium channel gated by intracellular nucleotides, ATP and ADP. This channel is found in the plasma membrane or within sub nuclear membranes. Absence of K_{ATP} significantly impairs the myocyte's ability to distribute Ca^{2+}, decreasing sensitivity to sympathetic stimulation [39].

The slow repolarising IKs channel

The IKs channel is a major voltage gated repolarising current in the ventricles, expelling $[K]^+$ ions from the myocyte in phases 2 and 3 of the ventricles [40]. It has slow opening kinetics and has been associated with heterogeneous expression across the myocardial wall.

Sarco/endoplasmic reticulum Ca^{2+} -ATPase (SERCA) Pump

The pump uses ATP (chemical stored energy) to transfer Ca^{2+} ions back into the SR after the contraction has terminated and Ca^{2+} has unbinded from troponin in the cell. It regulates cytosolic Ca^{2+} concentration, SR Ca^{2+} load, and the rate of contraction and relaxation of the heart [41]. It is controlled by the regulatory protein phospholamban in the ventricles and is potentiated under beta-adrenergic stimulation.

Beta adrenergic receptors

An important alteration of calcium handling is mediated by catecholamines (adrenaline and neuradrenalin) belonging to the sympathetic nervous system, which controls the fight or flight response. The catecholamines bind to beta-receptors in the heart. Activation of these receptors increases heart rate, relaxation speed and contractility. The increase in relaxation speed and contractility are thought to be the effect of cAMP dependent protein kinase (PKA)-mediated phosphorylation of proteins involved in Ca^{2+} handling [39]. Three important calcium handling proteins that are phosphorylated are:

- The L-type Ca^{2+} channel, involved in letting calcium into the cardiac cell at the beginning of the contraction. The current is enhanced by increasing the mean channel open time [42].

- RYR2, which controls contractility by gating the flow of sarcoplasmic calcium to the cytosol. When phosphorylated, the SR Ca^{2+} release is amplified.

- The phospholamban (PLB), which normally inhibits the SERCA pump. When phosphorylated, this ability is lost. This enables the excess intracellular Ca^{2+} to be transported back to the SR in diastole.

1.4 Effect of ACM gene mutations on single cell electrophysiology

Overwhelming evidence suggests that electrical abnormalities precede clinically perceivable structural abnormalities in ACM [43] [44] [45]. Examining the genetic basis of ACM can help to shed light on the pathogenesis, in the context of electrical disease progression.

Calcium handling is shown to be disrupted in patients with a PKP2 mutation in human, cellular reprogramming in vitro studies [46] [47] as shown in Figure 1.6. The cells are engineered using patient fibroblasts and the iPSC technique, which is used to

induce pluripotent stem cells from fibroblasts or embryonic cells [48]. Patient specific cells harbouring a PKP2 mutation with various pathogenic conditions were created in an vitro adult like feeding mechanism, with attenuated PPARG expression to produce fatty infiltration conditions. The cells were sustained in this environment, which simulates a system of adult cardiomyocytes outside of the human body [46] in ACM type extracellular conditions. Using this setup, it was shown that the intracellular Ca^{2+} concentration remains abnormally high in PKP2 mutated cells, as in Figure 1.6.
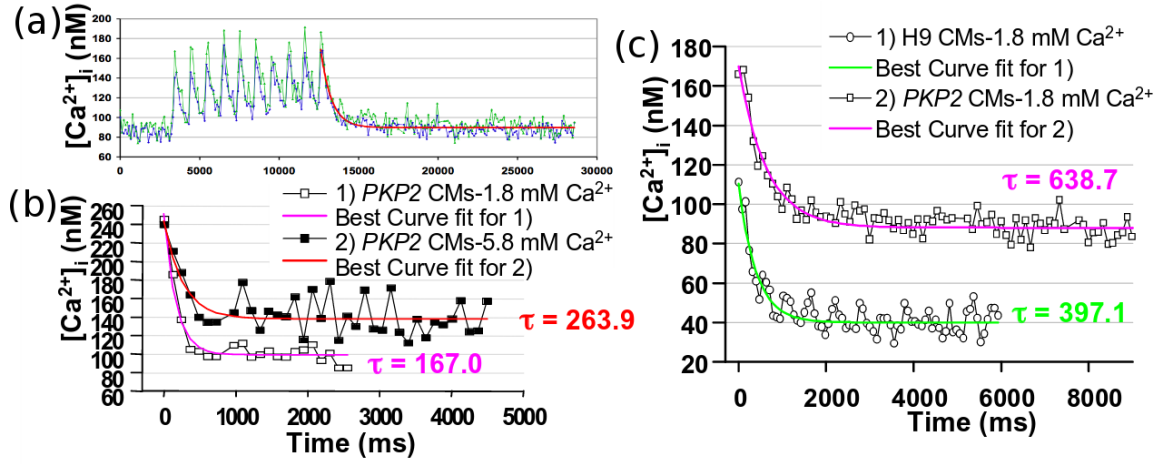
Figure 1.6: Ca^{2+} imaging in a PKP2 mutated human cell line of ACM shows Ca^{2+} cellular overload. (a) The pacing protocol. Myocytes are paced 10 times at 1Hz. (b) The intracellular Ca^{2+} decay is shown for 2 different solutions, one having a normal 1.8 mM concentration of extracellular calcium and one with abnormally high concentration of extracellular Ca^{2+}. Both measurements occur at normal lipogenesis and thus mimic normal PPARG functioning. (c) Healthy myocytes (1) and PKP2 dysfunctioning myocytes (2) were placed in an environment mimicking PPARG dysfunction and high lipogenesis. The Ca^{2+} decay constant for PKP2 modified cells is significantly larger than in healthy myocytes, suggesting a disrupted calcium handling is prominent in ACM [46].

In order to explain the calcium mishandling further, it is useful to look at levels of Ca^{2+} handling proteins. These are shown to be different from healthy myocyte levels and are compared in Figure 1.8.

A cell culture of iPSC-derived cardiomyocytes can be made with an ACM type PKP2 gene mutation. In a particular study, fibroblasts from a 30-year old male were used to populate the cell cultures and the cells were voltage clamped. The L-type channel's current response to a fixed voltage is measured and shown in Figure 1.7. An in vitro analysis of protein expression shows several signalling proteins of ionic

channels are disrupted in this mutation, which makes up to 2% of all ACM mutations worldwide. The protein expressions change in a fatty environment and can be seen in Figure 1.8. In particular, the protein expression of the L-type calcium channel is overexpressed.

A PKP2 knock out mouse model showed a prolongation of Ca^{2+} transient duration at 30% recovery and at 50% recovery from peak Ca^{2+} by 25% and 10.5% respectively [49]. The APD90 was also increased by 25% in the PKP2 mouse model and reflected the increase in Ca^{2+} transient duration. Major Ca^{2+} handling dysruption is caused by the lowered I_{CaL} peak current associated with an increase in its inactivation time.
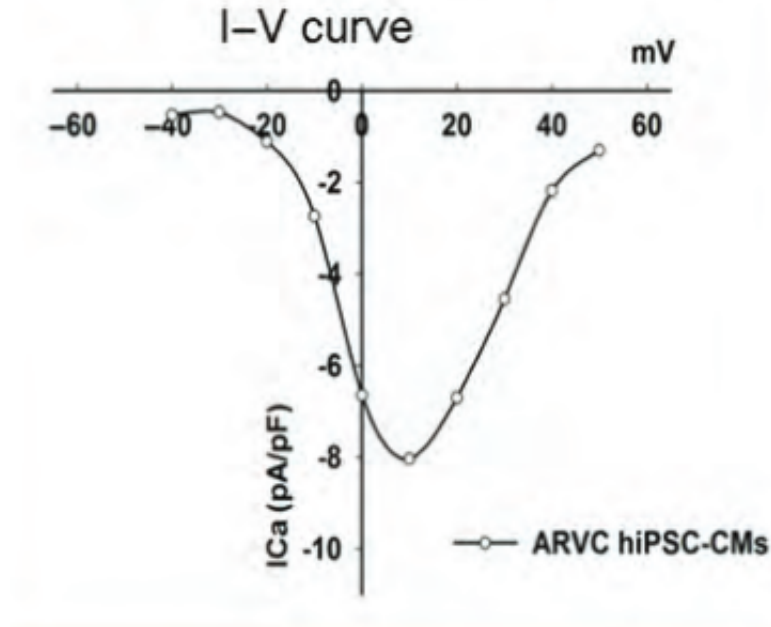
Figure 1.7: A representative current vs fixed voltage clamp response of I_{CaL}. The test voltage pulses in the range from -40 to +50mV. The cell response is that of a genetically engineered ACM mutation in the PKP2 gene, a prominent ACM mutation. This response is deemed similar to a healthy ventricular myocyte [47].

(a) 60D *PKP2* iPSC-CMs vs. 60D H9 hESC-CMs

Normalized to control H9 60D CMs (%)

(b) *PKP2* CMs after 5F vs. H9 CMs after 5F

Normalized to H9 hESC-CMs after 5F (%)
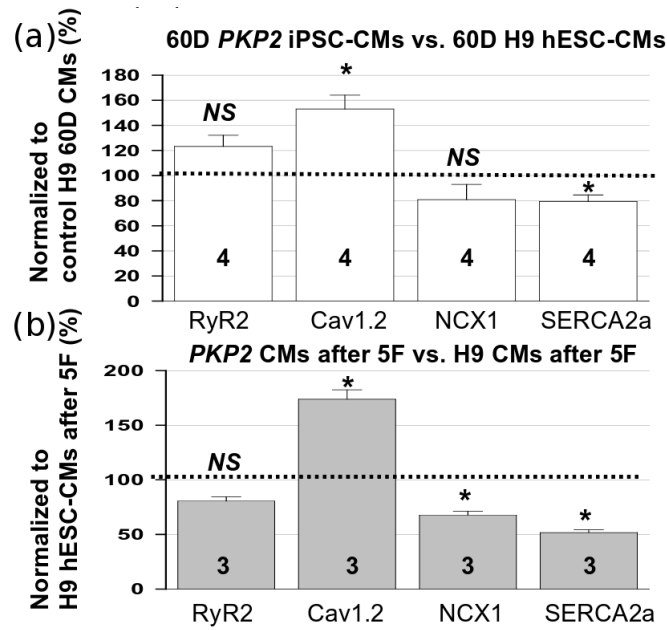
Figure 1.8: The same preparation protocol is used as in Figure 1.6. (a) In a normal PPARG environment, the RYR2 and Cav1.2 handling proteins are over expressed in PKP2 mutated cells, where as NCX1 and SERCA2a are under expressed. Note that these are merely the proteins handling the channels and not the channel currents themselves. (b) In a fatty environment, the protein levels follow a similar trend to the one in (a) with a reversal in tendency for the RYR2 protein. Furthermore, the change in channel protein expression between healthy and mutated myocytes grows in this environment. (* implies $p \leq 0.05$)

15

I_{Na} is targeted by ACM genetic mutations. In particular, a mutation of the DSG2 gene in transgenic mice is reported to decrease Na^+ current density. This results in a reduction in the AP upstroke velocity, slower conduction and increased arrhythmia susceptibility at disease stages prior to fibrotic replacement and necrosis [50]. The corresponding mouse model ionic behavior is illustrated in Figure 1.9. A similar behaviour is recorded in genetically engineered human cells, plagued by a SCN5A mutation and presented in Table 1.10.

To further quantify the degree of sodium channel reduction in ACM patients and electrophysiological consequences, AP biomarkers from a PKP-2 ACM human mutation, studied in iPSC in vitro human cells are included in Figure 1.1.

Cell Type	Vmax (V/s)	APA (mV)	MDP (mV)	cAPD90	n
H9 hESC-CMs	16.9±2.2	60.8±2.5	-43.7±1.8	291.8±3.9	43
ARVD iPSC-CMs	7.9±1.8	49.4±4.0	-37.5±3.0	265.6±15.0	16
ARVD iPSC-CMs+3F	4.3±0.6	44.0±4.3	-32.0±3.0	348.0±18.9	12
ARVD iPSC-CM+5F	3.1±0.4	39.2±3.7	-33.9±2.5	317.6±13.9	25

Table 1.1: The electrophysiological parameters measured in an iPSC human study of single cell electrophysiological ACM remodelling are summarised [46]. These cells present with downregulated subunits of the INa channel. The max upstroke velocity (V_{max}) and the peak action potential amplitude are governed by the sodium channel. As we can see, PKP2 mutation alone (2nd row) and increasing levels of fatty infiltration (3rd and 4th rows) lead to a decrease in AP upstroke velocity and peak amplitude. The values of the minimum resting potential did not change significantly from the baseline values, nor did the corrected APD values at 90% repolarisation, indicating the predominantly a depolarisation disturbance.

In ACM, the RYR2 receptor is shown to be the cause of leak of Ca^{2+} in diastole, leading to Ca^{2+} depletion, arrhythmogenesis and heart failure or SCD [53]. What ends the calcium induced calcium release is an open debate. A few ideas are put forward, namely stochastic attrition, RYR2 adaptation, RYR2 inactivation and SR depletion [35]. Let's look more closely at the mechanisms which lead to heart failure and result from a leaky RYR2 channel.

Heart failure can be an advanced phenotype of ACM and can stem from inadequate cardiac pump function, which does not meet the metabolic requirements of the organs in terms of blood flow. Initially, failing cardiac function can be offset by increased beta adrenergic stimulation and catechomic signalling, whose mechanisms are outlined in Section 1.3.1. However, chronic adrenergic stimulation or prolonged stimulation during exercise are associated with defects in the functioning of the SR Ca^{2+} release.
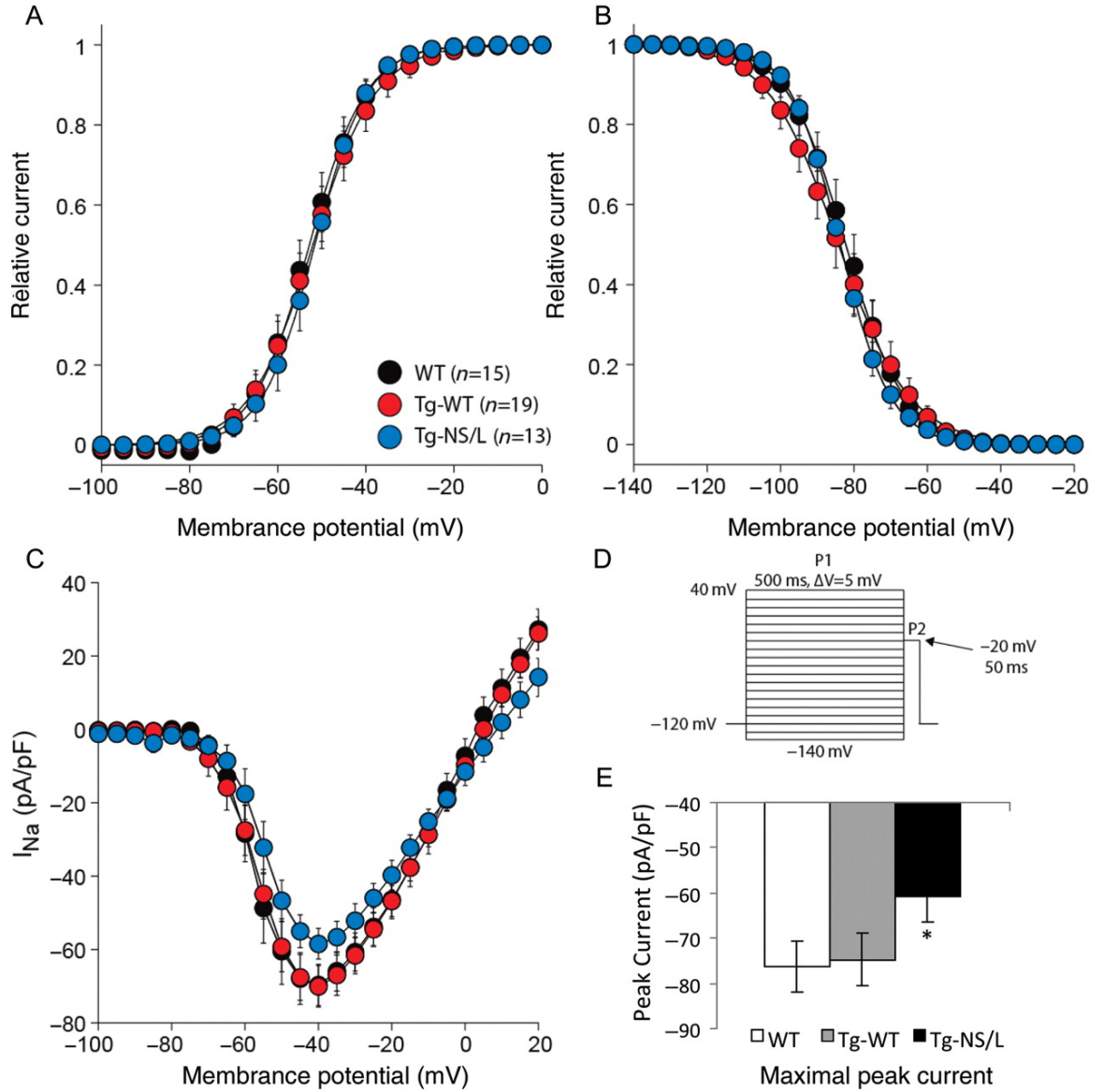
Figure 1.9: The differences between the Na$^+$ channel in controls (WT and Tg-WT) and over-expressed Dsg2 gene are shown in mice. The ion channel of the mutants shows a reduced peak negative potential (C) and reduced peak current (E) [50]. This gene mutation has been strongly associated with ACM development. An independent voltage clamp study of murine hearts confirmed these findings [51].

One such defective adaptation is a PKA hyperphosphorylation of the RYR2 channel [54] [55]. This makes the RYR2 channel exhibit a pathologically high level of open probability under resting conditions. Over time, this can lead to a reduction in the SR Ca^{2+} content, with less available calcium and consequently weaker contractions.

Above we have shown that a mechanism of spontaneous RYR2 opening in diastole can occur in particular physiological conditions. This results in a premature release
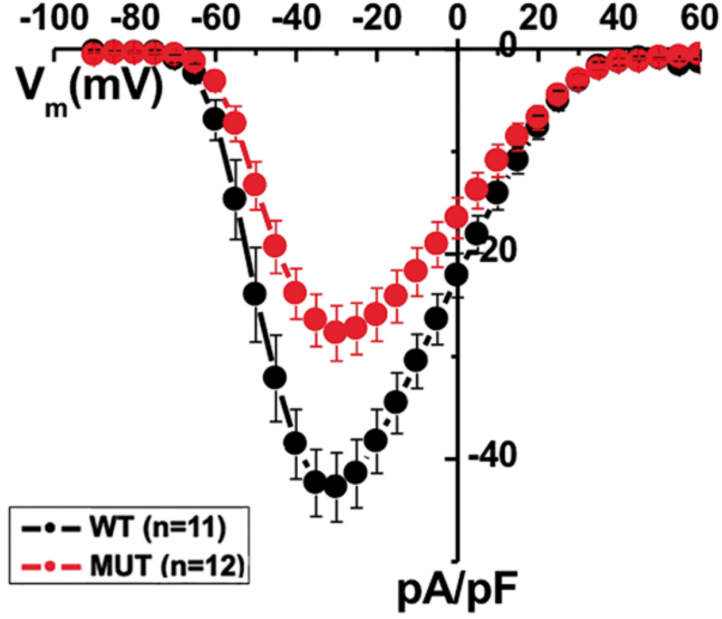
Figure 1.10: I-V relationship of I_{Na} in SCN5A mutant (red) and wild-type cells, derived from human embryonic kidney cells. Peak sodium is considerably reduced, $I_{Na,peak} = -27.7 \pm 2.7 pA/pF$ (mutant) and $I_{Na,peak} = -42.7 \pm 3.4 pA/pF$ [52].

of SR Ca^{2+}, activating the forward mode of the sodium calcium exchanger. If the threshold to activate fast Na^+ is reached, an action potential will be triggered in this cell with the potential to lead to premature contraction of part or the whole ventricle [56] [57]. If the cell is in a region within the vulnerability window, this cell can become an ectopic or a re-entry circuit can be formed in its vicinity, leading to asynchronous activation of the ventricle. The same phenomenon was confirmed to lead to ventricular tachycardia in mice as a result of late RYR2 hyperphosphorylation during exercise [58].

1.4.1 Repolarisation abnormalities

The I_{K1} channel has been found to be remodelled in ACM zebrafish, exhibiting a mutation in the plakoglobin JUP gene. The I_{K1} peak current is reduced by 30% as can be seen in Figure 1.11A, alongside a concommitant decrease in peak I_{Na} current (Figure 1.11B).

cAMP levels are reportedly lower than controls in an ACM in vivo human study [59], suggesting an impaired beta-adrenergic response in ACM. Given that the beta-adrenergic cascade shortens the APD in control patients, it is expected that the APD will not shorten to as great an extent when ACM patients exercise.
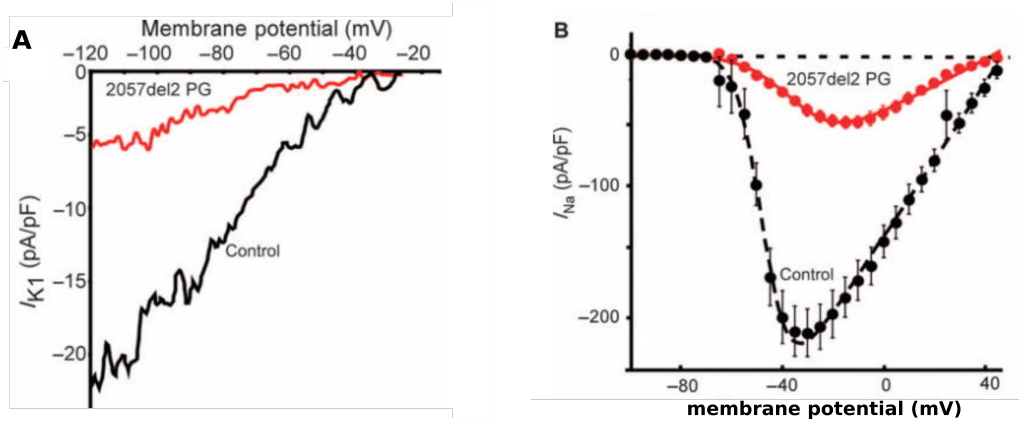
Figure 1.11: Single cell ventricular zebrafish electrophysiology is recorded using patch clamping, in the context of a human mutation [2]. (a) Significant reduction in the I_{K1} zebrafish trace, shown on a current vs voltage plot. (b) I_{Na} peak current is concommitantly reduced in this mutation.

Also known as PLN or PLB, phospholamban is a protein encoded by the PLN gene. It is a membrane protein, controlling the Ca^{2+} pump in myocytes [60]. PLN is found to be a substrate for the cAMP-dependent kinase (PKA) in cardiac muscle. PLB is an inhibitor of the SERCA channel in the unphosphorylated state but inhibition ceases upon phosphorylation. Beta agonists limit the suppression of the SERCA pump so that Ca^{2+} can be efficiently transported back into the SR during diastole. Studies show a mutation of the PLN gene is found in ACM patients, [61] suggesting ACM is also a disease of the calcium handling system under intense beta-adrenergic stimulation.

A summary of key electrophysiological findings related to ACM and confirmed experimentally is included in Figure 1.12.

Platelets

Platelets, also known as thrombocytes, are a component of the blood which co-agulates blood vessel injuries. They do so by releasing a cocktail of substances, in the vicinity of the injured site. Some of these substances are believed to be arrhythmogenic and a comprehensive list of qualitative effects is summarised by Flores et al [62]. Recent dog [63] and human ex-vivo [64] studies have shown that platelet activity is enhanced in ACM conditions. Due to their potential arrhythmogenic nature, platelet activity on electro-physiology (EP) needs further investigation, especially in the context of ACM.

A list of the most physiologically important substances secreted by platelets is given here.

Main Finding	Species	Cohort	Prep Protocol	Recording	Authors (DOI)
DSG2 mutation and INa current. Reduced upstroke velocity. Slow CV and fibrosis.	Mice	unspecified	in vivo ex vivo	ECG/TEM Immunofluo.	Rizzo et al. 10.1093/cvr/cvs219
PKP2 knockout Quantifies differences in I_{Na} and conductance between healthy and PKP suppressed hearts	Mice	transgenic	V clamp Langendorff	epicardial map	Cerrone 2012 10.1093/cvr/cvs218
SCN5a mutation and reduced INa current and N-cadherin. Prolonged QRS.	Human iPSC	6	Patch clamp in vitro	fluo ecg	Te Riele et al. 10.1093/cvr/cvw234
INa downregulation ICaL upregulation SERCA downreg NCX downreg. due to PKP2 mutation	Human	2	iPSC engineering	in vitro, immunochem, 37C temp qRT-PCR protein analysis imaging with Fura-2AM	Kim 2013 10.1038/nature11799
IK1 downregulation due to human 2057del2 mutation	mutant zebrafish rats	100	Embryo study	patch clamp immuno-fluo western blot	Asimaki et al. 10.1126/scitranslmed.3008008
ICaL traces and ARVC electrophysiology	Human iPSC	1	in vitro	patch clamp	Dongrui et al. 10.1093/eurheartj/ehs226
desmoglein 2 mutation leads to rapid ARVC type phenotype with myocardial lesions, myocyte death, aseptic inflammation fibrotic replacement and in the later stage, arrhythmia and permanent cardiac impairment	Mice	10	DSG2 ablation	protein expression E-microscopy	Kant 2012 10.1007/s00441-011-1322-3
Quantified cardiac conduction velocities as fcn. of cell shape and gap junction remodelling	Human (Computational)	Virtual	Linear strands of ARVC cells	NA	Wilders 2012 10.3389/fphys.2012.00168

Figure 1.12: Summary of animal and human studies of electrophysiology focussing on ACM.

- ATP is released, partially inhibiting the K_{ATP} channel. [65]. ATP is also reported to increase transient and resting cytosolic Ca^{2+}.

- Platelet activating factor (PAF): In dog and pig studies, intracoronary injection reduces blood pressure, myocardial contractility and coronary blood flow [66], [67].

- Arachidonic acid: It is reported to disrupt calcium handling, increasing intra-cellular calcium and transient calcium influx across the sarcolemma. [68]. Pro-longed exposure to these acids leads to intracellular Ca^{2+} overload in neonatal rat cardiomyocytes [69].

1.5 Effect of ACM gene mutations on structural heart muscle integrity

Malicious genetic mutations have been discovered in desmosomes, a junctional network responsible for cell to cell adhesion [70] [71]. Genetics has suggested a new model for pathogenesis, hypothesising that impaired functioning of the cell junctions under stress leads to myocyte detachment and cell death, as well as inflammation. The body's response is to provide a fibro-fatty replacement as repair. According to previous studies [6] [70] [72], at least 3 mechanisms contribute to the pro-arrhythmic substrate:

- patches of myocarditis, or other local mechanisms, leading to cell death, fibrosis and cavities [73]

- fibrous and adipose infiltrates within the myocardium

- gap junction remodelling leading to structural disarrangement of the lattice of myocytes

Several genes, responsible for the structural integrity of the ventricles, have been found to be related to ACM. The normal function of these genes regulates gap junction formation, cellular communication and cell coupling to the extracellular matrix. A summary of the sphere of influence of these genes is illustrated in Figure 1.13.
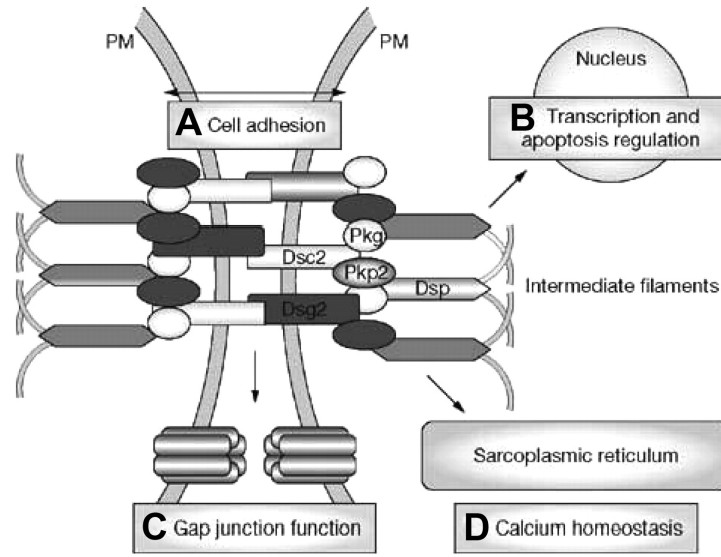
Figure 1.13: The cardiac desmosome and its proposed roles in (A) supporting the structural stability by ensuring cell-cell coupling (B) regulating the adipogenesis and apoptosis by controlling the transcription of the associated genes, maintaining smooth electrical conductivity through regulation of (C) gap junctions and (D) calcium homeostasis. Figure adapted from previous genetics review on ACM [71].

1.5.0.1 Desmosomes

Desmosomes couple adjacent myocytes together. This type of protein resists mechanical stress and can take 2 states, namely a strongly adhesive and hyper-adhesive state. The latter is characterised by a calcium independence, meaning that the mechanical properties of desmosomes are not influenced by the abundance of extra cellular calcium [74]. By contrast, the weaker state's adhesion property is calcium dependent. Desmoglein-2 is a protein localised to the intercalated disk, responsible for mechanically and electrically coupling adjacent myocytes. It is encoded by the DSG2 gene, which is known to mutate in ACM. Studies on mice showed that mutations of this gene lead to lesions in muscles early on, followed by dying myocytes with calcification in the lesion areas. This led to widening of the inter cellular cleft, dissociation of intercalated discs around the lesions and a disturbed sarcomere structure. The disease progresses into fibrosis and arrhythmias [75]. The main idea is that the mutated desmosomes are no longer able to support the mechanical stress of the contracting myocytes, leading to inflammation, induction of repair, fibrotic replacement, disconnection of myocytes, permanent disarrangement of the myocardium and altered force distribution. The disease progression is outlined in Figure 1.14 and has a striking resemblance to human ACM progression [76]. Another Dsg2 mouse model of ACM

recapitulates the human phenotype of RV wall thinning, as a result of myocardial injury, extending transmurally and involving fibro-fatty repair and progressive disappearance of the myocardial muscle tissue [77].

DSP Gene

Desmoplakin is a desmosomal protein encoded by the DSP gene. It enhances intracellular structural stability and its mutation is linked to cell disarray and fibro-fatty replacement in human variants of ACM [78]. A decrease in levels of desmoplakin and connexin-43 proteins at the intercalated disc was observed. A global inflammation the ventricles, known as myocarditis, has been observed to be a symptom of ACM in 100% of patients in a cohort harboring a DSP mutation and may accelerate intracellular degeneration processes, myocyte death and fibro-fatty infiltration [79].

DSC2 Gene

DSC2 encodes the Desmocollin-2 protein in cardiac myocytes. The protein is used in linking adjacent cells together in desmosome regions, much like the DSG2 gene. It is also shown to be involved in desmosome formation. Strong evidence suggests mutations are associated with ACM [80] [81], including mutations with a recessive inheritance [82]. Another mouse model found that a mutation in DSG2 leads to uncontrolled necrosis or muscle tissue disappearance [83] affecting both ventricles and involving concomitant fibro-fatty replacement.

JUP Gene

Plakoglobin is a protein encoded by the JUP gene. Plakoglobin is the cytoplasmic component of the desmosomes and adherens structures. Plakoglobin is essential for the development of intercalated discs and stability of cardiac muscle. More specifically, it is the only stabilising link between calcium dependent cadherins and the actin cytoskeleton. If the beta-catenin and plakoglobin proteins are suppressed in mice, this results in gap junction remodelling and arrhythmogenesis [84]. Additionally, dysfunction of plakoglobin results in a mutation of the heart progenitor cells, which could lead to adipocyte formation [85].

Connexins Connexins are a family of proteins forming gap junctions between cardiomyocytes. The connexin 43 (Cx43) protein is heavily expressed in the myocardial ventricular tissue and its abundance is associated with gap-junctional ion channel conductance levels, conduction velocity and structural gap junction stability [86]. Lack of this protein leads to significant dispersion of conduction, increased incidence of spontaneous arrhythmias, and loss of ventricular systolic function with only minor reductions in overall Cx43 expression in a murine model [87], particularly in
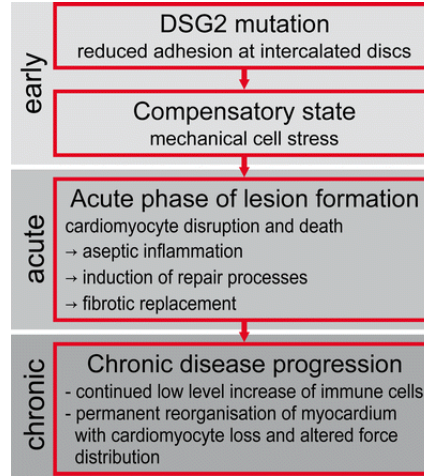
Figure 1.14: The hypothesis of disease progression in mouse as a result of DSG2 mutation is outlined and figure is reported from [75]. Early phase is fully developed within 2 weeks of gene modification, acute phase phenotypes are visible by week 4 and a much slower, chronic phase of the disease onsets from week 8 onwards.

the context of the His Purkinje ventricular conduction system [86]. Cx43 is reportedly decreased in mutations associated with ACM [88].

1.5.0.2 Non-desmosomal mutations and structural manifestations

AnkyrinG or AnkG

AnkyrinG is a member of a family of adaptor proteins that mediate the attachment of the integral membrane proteins to the spectrin-actin based cytoskeleton [89]. AnkG is required for maintaining a polarised distribution of many membrane proteins including the Na^+/K^+ATPase Pump, the voltage gated Na^+ channel and the Na^+/Ca^{2+} exchanger. A physical association between AnkG and PkP2 has been observed recently [90]. A loss of AnkG expression leads to relocalisation of PKP2.

PKP2

PKP2 is a gene, whose mutation is known to be strongly associated with ACM [91] [92] and is one of the most frequently remodelled genes affecting cardiac structure, as shown in Figure 1.15. Mutations of this gene have repercussions on both electrophysiology and muscle structure, hence it is included herein. It encodes the protein Plakophilin-2, whose function is to link cadherins to intermediate filaments in the cytoskeleton, as can be seen in Figure 1.13. A loss of PKP2 expression leads to I_{Na} remodelling [90], a decrease and redistribution of the connexin 43 protein as well as an overall decrease in coupling between adjacent myocytes. Furthermore, there is experimental evidence in mice suggesting that plakophilin-2 binds to the ATP-sensitive

potassium channel, reducing its current density by 60% and introducing regional heterogeneity in the channel [93]. Thus, the PKP2 gene and its associated protein can be thought of as a link between intracellular junction and cell excitability.
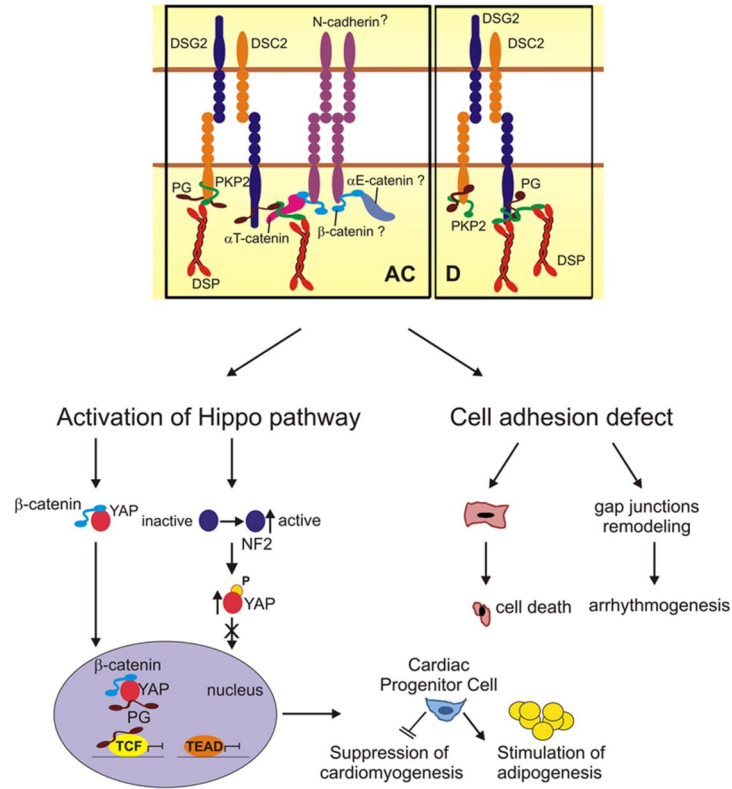
Figure 1.15: Gene mutation to macroscopic heart imbalances in ACM [94]. The gene mutation either influences the cardiac myocytes internally or externally. These effects combined lead to arrhythmogenesis.

Silencing of PKP2 in cultured cardiomyocytes reduces the electrical conduction velocity [95]. It remains an open debate whether this reduction in velocity is due to reduced electrical coupling at gap junctions or decreased sodium current availability or due to both factors.

The extra and intra-cellular mechanisms of cell binding and adhesion are explained in Figure 1.13. As the genes associated with structural integrity of the desmosomes mutate, they trigger a chain reaction, outlined in Figure 1.15. Either the gene mutation suppresses the intra-cellular process of cardiomyogenesis or it hits the extra-cellular network, comprising of ionic channels and gap junctions. The former leads to suppression of myogenesis, stimulating adipogenesis and the latter leads to cell death and decoupling/disarrangement of myocyte strands. A structural phenotype can include mild to severe, localised and global RV dilation [92]. The combination of

these effects results in arrhythmogenesis at heart level.

Gene	Locus	Protein	% of Disease
PKP2	12p11	Plakophilin 2	25%–40%
DSG2	18q12.1	Desmoglein 2	5%–10%
DSP	6p24	Desmoplakin	2%–12%
DSC2	18q12.1	Desmocollin 2	2%–7%

Figure 1.16: An international consensus paper on ACM and other diseases outlines 4 main genes are involved in the ACM mutation. PKP2 has the highest incidence [96].

PPARγ

Although not a gene, peroxisome proliferator-acitvated receptor gamma (PPARγ or PPARG) is a glitazone receptor, encoded by PARG gene in humans [97] involved in structural remodelling of the ACM heart. It is involved in the production of adipose tissue. Mice, which are genetically engineered to overexpress this gene, are found to develop dilated cardiomyopathy like symptoms [98], including heart dilation, reduced ejection fraction and increased levels of failure biomarkers. Human tissue sample assays also found a link between PPRAGγ, intracellular lipid overload, fatty production and contractile dysfunction [99]. Interestingly, this pathway is overexpressed in the RV yet is found to be functioning normally in the LV of patients studied, suggesting another mechanism may be at play in the LV fat generation process [100], which remains to be elucidated.

SCN5A

This gene has been shown to affect the structural muscle integrity in the heart, via its interaction with N-cadherin [52]. Depending on the protein interaction affected, genetic changes in NaV1.5 may thereby cause a predominantly structural phenotype (e.g. dilated cardiomyopathy), predominantly electrical phenotype (e.g. Brugada Syndrome, Long QT syndrome), or mixed electrical and structural phenotype (e.g. ACM). As such, the affected protein interaction, more than the exact gene mutation, may determine the phenotype. The biochemical mechanism governing the structural alterations due to SCN5A are yet unclear. This gene has originally been associated with control of the sodium channel [101]. Several mutations in this gene are observed to reduce peak I_{Na} availability and prolong recovery from inactivation. This is one of the genes which impacts both muscle structure and single cell electrophysiology.

1.5.0.3   Non-genetic contributions to structural disease

Intense physical exercise

Competitive sport is observed to increase disease penetrance [102]. It promotes mechanical and oxidative stress. Areas of the ventricles show reduced reuptake of norepinephrine leading to chronic stimulation of adrenergic receptors, which in turn has been related to cardiac fibrosis. Fibrosis is known as the result of overactive fibroblasts, proteins which change the extracellular matrix properties of the tissue and result in a replacement of myocardial tissue into non-conducting scar [103]. It can result from inflammation, act as a reparative process when there is uncontrolled cell death, thus avoiding cardiac rupture or appear as a result of an overexpression of the TGF-β gene. Fibrosis can take different shapes and affect heart muscle electrical and contractile function [104].

A major diagnostic criterion for ACM, RV dilation can be a result from intense physical exercise in mice with a PKP2 ACM mutation [105]. In this model of disease, connexin 43 delocalization at intercardiomyocyte gap junctions occurs in trained mice presenting with RV dilation.

1.6   Mechanisms of conduction modulation in ACM

There is an established interplay between conduction velocity and the balance of ions in cardiac muscle. There is an observed anisotropy of conduction in the longitudinal and transverse directions relative to myocyte strand orientations. Conduction velocity is shown to be higher along the muscle fibers than across them [106]. Anisotropy of repolarisation has also been identified along the transmural direction of the ventricles and is of the order 20-25 ms [107]. This is physiological behaviour yet pathophysiological levels of the conduction velocity of the depolarisation wave in the ACM ventricles has been associated with low sodium channel conductance [108]. Conduction velocity is modulated by the I_{Na} channel dynamics. It has been shown to be reduced in human and mice [50] tissue samples due to a lower density of sodium channels at the level of the intercalated disk. Mutations in the PKP2 and SCN5A genes associated with ACM can lead to decreased peak sodium current, as discussed in Section 1.4.1 of the thesis. An iPSC baseline model of ACM exhibited a 53% reduction in peak AP gradient upstroke, as observed in Table 1.1. This leads to a slowing of the electrical wave, as each cell will take longer to reach its peak potential and trigger the opening of the neighbouring cell's voltage-gated I_{Na} channels. Patch clamp experiments in a mice PKP2 mutation of ACM [49], data from which are shown in

Figure 1.17, show a reduced peak I_{NaL} and I_{K1} currents. The qualitative effect of this mutation on AP morphology is an increased time to peak voltage and a less negative resting membrane potential. The combination of this electrophysiological remodelling on human ventricular tissue level conduction velocity is explored via a computational study by modulating I_{Na} and I_{K1} and studying the CV response in a fiber of human tissue, which can be found in Chapter 2. Moreover, in a human study on explanted ACM hearts [109], biological tissue analyses further showed disturbed distribution and significantly reduced expression of Connexin 43. A 50% reduction in this molecule has been recorded to severely impair conduction velocity in both the longitudinal and transverse fiber directions in mice [110] by tracking the electrical wave using an optical mapping technique, discussed in the imaging section of Chapter ??. These results are presented in Figure 1.18. The exact mechanism via which Cx43 influences conduction slowing remains unclear yet it is heavily expressed near gap junctional channels, suggesting it causes a disruptance to the passage of Na^+ ions between neighboring cells by affecting the conduction properties of the gap junctional ionic channels and delaying the electrical activation wave [111]. Connexin 40 and 43 are heavily expressed in the fast conduction system of the ventricles, also known as the Purkinje network. This expression is known to increase conduction speed of the electrical wave in the Purkinje fibers [112] and a decrease in their abundance can lead to conduction slowing or conduction block in a recent mice study [113].
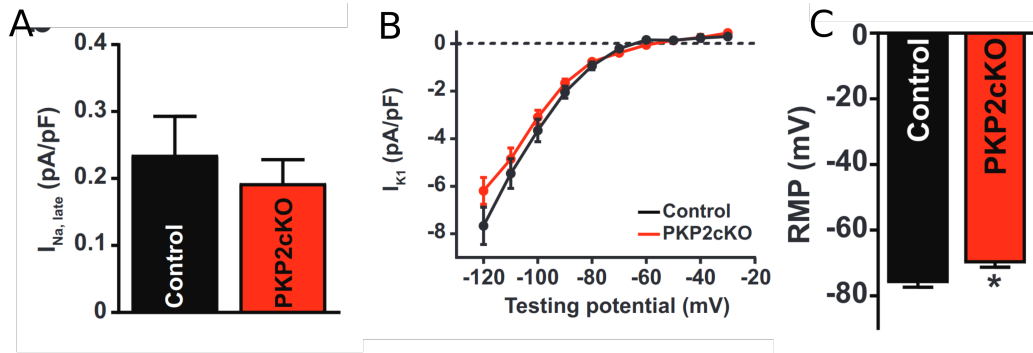
Figure 1.17: A. 21 day old mice with a PKP2 mutation present with reduced peak late I_{Na} current, when undergoing patch clamp I-V protocol. The data presented are the mean values for all the animals studied. B. The same experimental protocol revealed a decrease in peak current through the I_{K1} repolarising channel. C. The shape of the AP was altered as a result of these electrophysiological changes, inducing a less negative resting mebrane potential (RMP) during phase 4 of the AP in the PKP2 mice model [49] .
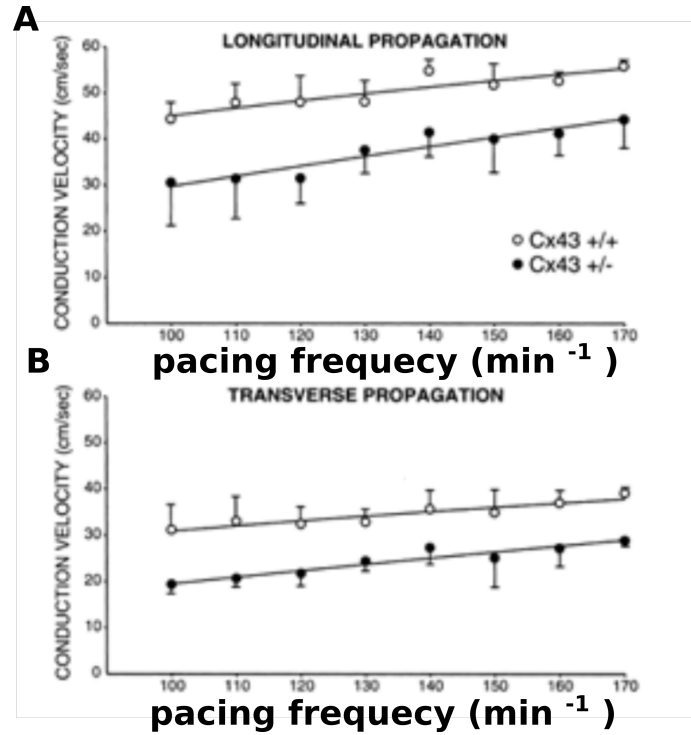
Figure 1.18: A. Conduction velocity in the principal fiber direction is plotted against pacing frequency for control mice (white circles) and 50% induced Cx43 abundance mince (black). Notice that the percentage difference in CV increases for higher pacing rates. B. Conduction velocity in the tranverse muscle fiber direction is plotted against pacing frequency for control mice (white circles) and 50% induced Cx43 abundance mince (black). Notice that the percentage difference in CV increases for higher pacing rates also in this case [110].

In ACM, the number of gap junctions may be significantly decreased, while at the same time sodium current is down regulated. A study by Sato et al. [95] shows that the sodium current density can decrease by up to 50% in ACM human patients. It is not yet certain if there is a causal link between the two effects.

As discussed earlier in this chapter, fibrosis may arise as the body's healing response to myocardial degradation. It is another substrate which can alter the electrical properties of the myocardium. As a non-active conductor of electricity, the fibrotic scar's electrical conductivity coefficient is lower than the surrounding myocardium [114]. The actual extent of conduction slowing may depend on the type of fibrotic infiltration, the extent as well as density of surviving myocardium within the scar region [115]. Fibrofatty replacement of the His-Purkinje system, affecting both its bundle branches, has been reported post-mortem in ACM [116]. This can lead to major conduction abnormalities of the ventricles as the Purkinje network is the highway

of conduction of the ventricles and contributes to uniform initiation of the ventricular activation sequence in the endocardium. Fat infiltration is another substrate likely to be a barrier to planar, smooth conduction. Fat is an insulator and is observed to produce conduction abnormalities in human patients imaged [117]. Cell disarray is also observed in human patient tissue samples and is associated with poor ventricular conduction [78]. A quantification of the contribution of these substrates to conduction slowing is missing in the above mentioned studies and computer modelling of the ventricles can help to access the degree of conduction delay in regions where these substrates exist.

1.7   Conclusion

ACM is a rare form of potentially lethal inherited cardiomyopathy. Since the right-sided form of the disease was first defined in the 1980s, significant progress in understanding the functioning of the disease has been made. Unfortunately, this has not led to successful umbrella treatments for the disease and patients have been treated using strategies developed for other forms of cardiac disease, such as anti-arrhythmic drugs, implanted defibrilators and lifestyle restrictions. Significant basic science efforts have contributed to undestanding the link between genes mutated and protein expression, with downstream effect on electrical and structural disease manifestation. A summary of key manifestations of ACM in the ventricles is given below.

- Rupture of the intracellular myocyte coupling due to gap-junction remodelling leading to increase in RV chamber volume.

- Fibrotic scars creation as a reparatory response to muscle degradation in the ventricular myocardium and in the fast Purkinje network of fibers.

- Fatty infiltration as the body attempts to maintain the structural stability of the ventricles.

- A decrease in peak sodium current depolarising the myocyte as well as decrease in peak action potential gradient dV/dt and a concommitant decrease in peak conductance of I_{K1} channel, leading to resting membrane depolarisation.

- Contractility alterations as a result of Ca^{2+} ion imbalances during the cell cycle.

- Disarray of the fibers and cells within the muscle fibers.

- Myocardial muscle thinning due to uncontrolled cell death and consequent RV wall thinning.

As can be seen, ACM affects the ventricles in several ways. The computational experiments performed for this thesis will aim to address how the electrical propagation during sinus rhythm in the ventricles changes as a result of ACM-induced remodelling. Shedding light on the dynamics involved will help understand disease function and increase our working understanding of this complex clinical entity.

Chapter 2

Conduction Velocity Modulation due to Co-Expression of I_{Na}–I_{K1} in ACM

2.1 Abstract

Conduction velocity (CV) heterogeneities are a long established pro-tachicardic substrate in cardiac disease, including ACM. One mechanism for generating dispersion of electrical conduction is conduction slowing in myocardial tissue. Both the I_{Na} and I_{K1} ionic channels are known to have concommitant reductions of their conductances in given mutations of ACM in zebrafish [2] and human studies [49]. The I_{Na} channel is implicated in several ACM genetic mutations [118] [51]. The main role of I_{K1} in influencing CV may be via a co-modulation of the I_{Na} channel conductance yet this effect is yet to be quantified in human experiments.

The rate dependent interactions of the $I_{Na} - I_{K1}$ ion channel complex on human ventricular CV are studied using an in-silico model. Two response domains of the myocardial tissue are found. There exists a slow frequency of pacing domain (1 Hz), where CV is largely governed by the I_{Na} channel alone. In the fast frequency domain (3.3 Hz), I_{K1} plays a marginal role in determining ventricular CV. The simulation results suggest that, under arrhythmogenic conditions, the upper limit of the CV is governed by the $I_{Na} - I_{K1}$ conductivity ratio. The simulations put an upper limit of 45% conduction velocity modulation in ACM myocardial tissue, which is attributable to $I_{Na} - I_{K1}$ electrophysiological remodelling. Certain loop diuretics are known to induce severe hypokalemia in ACM patients [119] and this is suspected to lead to an increased count of arrhythmia. Another type of diuretic used in treating ACM, a potassium-sparing diuretic such as spironolactone, is known to prevent potassium excretion from the body and can lead to hyperkalemia if poorly managed [120] [121]. The role of the potassium extracellular concentration in promoting CV changes in

ACM ventricles is modelled and the findings discussed with respect to arrhythmia risk.

2.2 Introduction

Several cardiac diseases exhibit dispersion of electrical conduction velocity (CV), including atrial fibrillation [122], Brugada Syndrome [123], hypertrophic cardiomyopathy [124] and ACM [125]. Slow and heterogeneous CV, in combination with appropriate anatomical substrates, translates into an increased risk of re-entry. Even in the absence of structural heart changes, such as in early-stage ACM patients with ion channel remodelling but otherwise healthy hearts [125], CV abnormalities have been shown to cause sudden cardiac death in young individuals [126]. Cardiac voltage-gated sodium channels (I_{Na}) are transmembrane proteins responsible for regulating the flow of sodium ions. Mutations in the SCN5A gene, which reduce peak I_{Na} current in ACM [52], have been shown to lead to lethal arrhythmias [31]. The inward rectifier current (I_{K1}) stabilises the resting membrane potential in phases 3 and 4 of the action potential (AP) cycle. I_{K1} has been experimentally shown to contribute to the creation of regional differences in cardiac excitability [127]. The role of I_{Na} on governing CV in the context of ACM is well established experimentally. A study by Sato et al. [128] shows that the sodium current density can decrease by up to 50% in ACM human patients leading to alterations in CV. Similar results were obtained by optical voltage mapping in guinea pig ventricle, when altering the conductance of I_{K1} [129]. The co-regulation of I_{Na} and I_{K1} is shown to occur in a plakoglobin ACM mutation, with data indicating a decrease in the conductance of both channels, as shown in Figure 2.1. Understanding the effect of co-modulating two important ionic currents, known to be responsible for CV modulation in isolation, is important in the context of ACM, as it can provide additional information on whether CV modulation is additive when both I_{Na} and I_{K1} are downregulated and help inform whether I_{Na} and I_{K1} have similar quantitative effect on CV when co-modulated in human tissue simulations.

Emerging experimental evidence suggests ionic channels are not regulated independently and are organised in macromolecular complexes [130]. The I_{Na}-I_{K1} ionic channels form one such complex, which was shown to control cardiac excitability and arrhythmia by Milstein et al [1]. Their inter-species study concluded that an increase in functional expression of one channel reciprocally modulates the expression of the other, in order to maximise cardiac excitability. The same effect was observed when

the mechanism was one of reducing the maxiumum channel densities by infecting cells with an aderovirus.

The extracellular potassium concentration $[K^+]^o$ is another governing factor of CV in the myocardium. An elevated concentration of $[K^+]^o$, known as hyperkalemia, is experimentally shown to globally induce I_{Na} inactivation and I_{K1} opening [131], promoting longer refractoriness of myocytes. Equally, low levels of $[K^+]^o$ are thought to lead to hyperpolarisation or an overall decrease in the resting cell potential. Both of these effects have repercussions on conduction. In the context of ACM, clinical reports have shown that ACM patients with structurally compromised hearts have more arrhythmic episodes in hypokalemic conditions [119].An investigation into the way hypokalemia affects CV can shed light on whether the arrhythmia generation mechanisms in ACM can be due to alterations in tissue CV. Hyperkalemia is experimentally known to induce arrhythmias, even without the presence of a pro-fibrotic structural substrate due to interaction with I_{Na} channel dynamics and APD shortening [132]. Furthermore, hyperkalemia inducing kidney disease be found as a comorbidity to ACM [133] and commonly prescribed diuretics such as spironolactone, used for the management of ACM symptoms [120] are known to increase $[K^+]^o$, can also lead to hyperkalemia. A quantification of CV modulation due to hyperkalemia can give order of magnitude estimates of the involvment of hyperkalemia in CV governance in the context of ACM patients. With this premise in mind, we set out to investigate the interplay between I_{Na} -I_{K1} on ventricular CV and upstroke time in 1D fibres. We focus on the rate dependence of the interaction by studying several pacing rates.

2.3 Methods

2.3.1 The Human Ventricular Cell and Tissue Model

This in silico study was performed using a state of the art electrophysiological single cell model of the human ventricular cardiomyocyte, the Comprehensive in vitro Proarrhythmia Assay updated O'Hara Rudy dynamic (ORd) model [134]. It is an extensively validated human cardiac electrophysiological model, incorporating the main ionic channels and sub-cellular processes involved in the myocyte AP cycle. It is used in the context of the bidomain formulation, in order to couple the cells in a tissue simulation. The bidomain formulation is a mathematical framework for describing the flow of charge within the myocardium. The assumption is that charge flows between an extracellular and intracellular domain through ionic channels or due to a
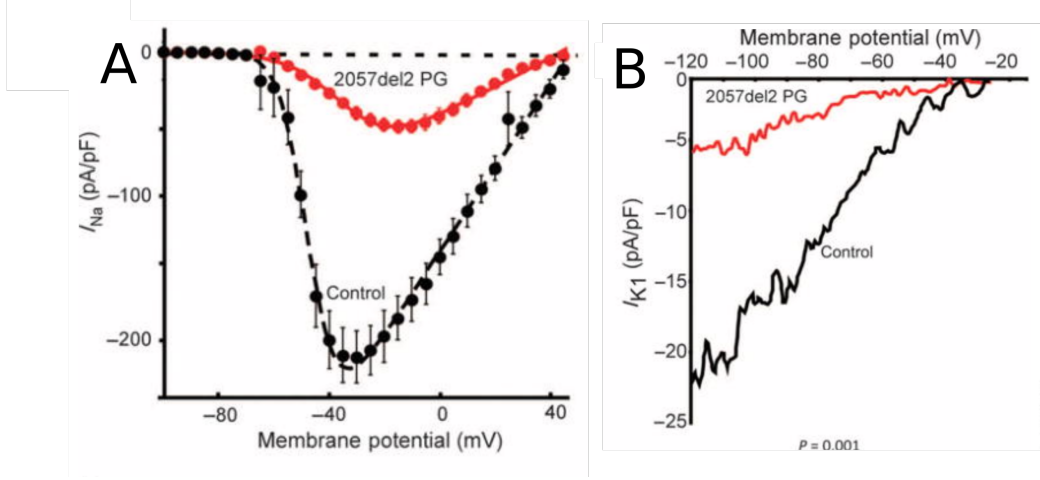
Figure 2.1: Co-modulation of I_{Na}-I_{K1} peak current densities in zebrafish cardiomyocytes when a plakoglobin gene ACM human mutation is introduced. A. Modulation of I_{Na} peak current by (red trace) relative to a control I_{Na} black trace, in a voltage clamp experiment. B. Concommitant modulation of peak I_{K1} current in the same cell as in A (red trace), compared with a control zebrafish cell (black trace).

potential gradient and can be described mathematically in Equation 2.1. A no flux boundary condition is imposed, meaning charge cannot leak out of the myocardium, as described by Equation 2.2.

$$\nabla.(\sigma_i \nabla v_i) + \nabla.(\sigma_e \nabla v_e) = \chi C_m(\frac{\partial v}{\partial t} + I_{ion}) \tag{2.1}$$

$$\nabla.(\sigma_0 \nabla v_0) = 0 \tag{2.2}$$

Where σ_i is the intracellular and σ_e the extracellular electrical conductivities, v_i the intracellular potential, v_e the extracellular potential, χ is the the surface to volume ratio of the cell membrane, C_m is the capacitance per unit area of the cell membrane and I_{ion} the contribution from the cell ionic dynamics to the transmembrane current.

2.3.2 In silico experimental setup

Nodes are set up in 1D fibres, the simplest possible coupled system. The nodes are 0.4mm in length and each node represents an ensamble of cardiac cells. The overall length of the fibre is 2cm, comprising of 50 nodes. The model is paced into steady state initially before recordings take place, in order to ensure an equilibrium state of the model is reached. The 5 leftmost cells, situated at one end of the fibre, are excited simultaneously. Activation times (ms) are recorded by analysing the transmembrane potential, V, across each node. The activation time of the cell is defined as the

time point of maximum gradient of the transmembrane voltage. Activation times are recorded for a range of individual channel conductances, G $[\frac{\mu S}{\mu F}]$, via a parameter sweep for the 2 channels of this study, I_{Na} and I_{K1}. The CV was subsequently calculated by the gradient of the least squares linear fit of the resulting plot of activation times of the cells. Simulations were conducted for a range of [0.1,1] scaling factors of the I_{Na} and I_{K1} channel conductances, G_{Na} and G_{K1} $[\frac{\mu S}{\mu F}]$, where 1 represents average current density and 0.1 is equivalent to 10% of the maximal current density. In order to measure if the I_{Na} - I_{K1} interaction is rate dependent, the fibres are paced using square waves of 1ms width, amplitude of -120000 pA/pF, at different periods or beat cycle lengths (BCLs). The 100 and 200 beats per minute cases are shown, where the first scenario mimics a resting heart rate in the upper limit of a control subject and the latter a fast ventricular tachychardia [135]. The healthy concentration of extracellular potassium ions in the model is $[K^+]^o$ =5.4 mM. A scaling factor is applied to $[K^+]^o$ in order to study the effect of abnormally high and low concentrations on ventricular CV.

2.4 Results

2.4.1 Low frequency pacing limit

The CV at low pacing rates ($>$ 600 BCL), was found to be almost entirely controlled by the I_{Na} conductance scaling factor. As one blocks a larger portion of the I_{Na} channel, the CV also decreases, as illustrated in Figure 2.2. The CV varies by less than 1% within the range of I_{K1} scaling factors studied, implying a weak dependence of the CV on G_{K1} in the low frequency pacing mode, equivalent to sinus rhythm. An ACM mutation is shown to reduce peak I_{Na} conductance by 84% and peak I_{K1} conductance by 71% [2] due to intercallated disk remodelling. By looking at the results in Figure 2.2B, it can be concluded that an upper limit for conduction velocity modulation due to this effect is 45%, as the combined decrease in conductance of I_{Na}-I_{K1} leads to a decrease of conduction velocity from 0.4m/s to 0.22 m/s. The above limit to ionic channel-caused CV modulation can be used to inform whole ventricular models of ACM, setting a lower limit for a possible ion channel-based CV slowing in myocardial tissue. The plots also suggest I_{K1} has a less dominant role in modulating CV in human tissue than murine models predict [129]. Using modulation factor values of I_{Na}-I_{K1} from an ACM zebrafish model with a plakoglobin mutation [2] to constrain the human ventricular analysis, suggests a decrease in tissue CV by up to 20% at slow pacing in human subjects, as per Figure 2.2(a).
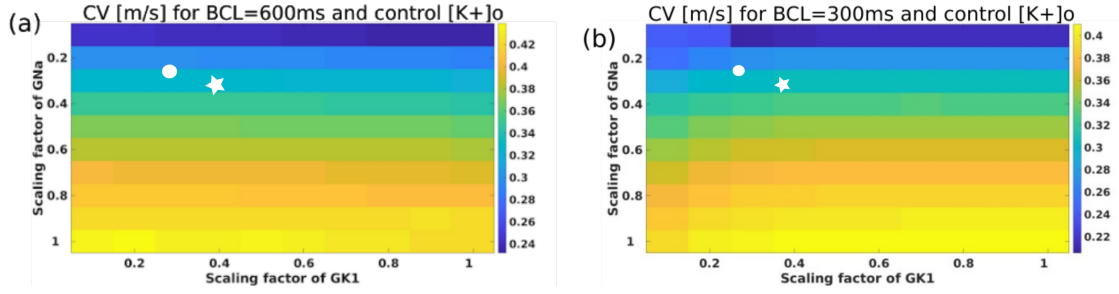
Figure 2.2: The CV along a 1D ventricular fiber [m/s] in case of (a) fast sinus rhythm pacing (600 ms BCL) and (b) tachycardic pacing (300 ms BCL) for different scaling factors of the original conductances, G_{Na} and G_{K1}. The CV is constant when varying the I_{K1} conductance and is governed by the sodium channel dynamics. The experimentally measured co-modulation of maximum current densities is plotted using a circle for a plakoglobin ACM mutation in a zebrafish model [2] and with a star for a rat model [1] not harbouring a specific ACM mutation.

2.4.2 High frequency pacing limit

The high frequency pacing range is not reachable in sinus rhythm and is presented here to simulate a tachicardic scenario. At fast pacing frequencies (BCL $\leq$ 300 ms), the CV was found to be dependent on I_{Na} - I_{K1} interactions. The CV exhibited a positive correlation with G_{Na} and a mild positive correlation with G_{K1} scaling factors, as illustrated in Figure 2.2(b), only at low values of G_{K1}<0.3. The I_{K1} in isolation is found to not have a major effect on CV in human tissue simulations. These results are relevant in the context of ACM as some patients with a PKP-2 mutation [49] will still mostly have conduction velocity of the electrical wavefront depend on I_{Na} and only marginally on I_{K1}. Yet, a co-modulation of I_{Na} - I_{K1} may result in I_{K1} indirectly influencing CV by its modulating effect on I_{Na}. Using modulation factor values of I_{Na}-I_{K1} from an ACM zebrafish model [2] with a plakoglobin mutation to constrain the human ventricular analysis, suggests a decrease in tissue CV of up to 25% at fast pacing in human subjects, as per Figure 2.2 (b). Whilst experimental evidence for this process exists in murine non-ACM [136] and ACM specific zebrafish studies [2], it is yet to be quantified in human subjects. If this is the case, ACM mutations involving I_{K1} will have dangerous effects of reducing global CV and increasing heterogeneity of conduction as well as arrhythmogenesis in ACM patient hearts.

2.4.3 High extracellular potassium reduces global CV

ACM patients in advanced disease stages are prescribed spironolactone, a potassium sparing diuretic, which can cause hyperkalemia [137]. Furthermore, reports of ACM

patients developing kidney disease exist [133], which also has a consequence of increasing extracellular potassium levels. For this reason, the effects on tissue CV due to hyperkalemia are studied. Hyperkalemia features abnormally high extracellular concentrations of the potassium ion, denoted by $[K^+]^o$. It results from a high intake of $[K^+]^o$ or kidney disease. It can be shown from the Nernst equation that an increase of extracellular K^+ concentration raises the ion's equilibrium potential. This is because the electrical potential opposes diffusion gradients across the cell membrane. Increasing $[K^+]^o$ results in a smaller diffusion gradient and also a less negative equilibrium potential [138]. In turn, the resting membrane potential becomes less negative. As the recovery from inactivation of the I_{Na} channel is voltage dependent, a more depolarised resting membrane potential inhibits a full sodium channel recovery. Furthermore, as $I_{K1} \sim \sqrt{[K^+]^o}$ in the ORd model, an increase in $[K^+]^o$ implies a more abundant maximum I_{K1} repolarising current and hence a shortening of the APD. The same mechanism holds for the fast delayed repolarising potassium current I_{Kr}, which is potentiated under hyperkalemia as its activity is dependent on $[K^+]^o$.

The simulations confirm this mechanism, as shown in Figure 2.3. Hence, I_{Na} peak availability is reduced and CV is slow in a hyperkalemic setting, as captured by Figure 2.4. Qualitatively similar behavior was observed at a higher BCL of 600 ms. An ACM patient experiencing a hyperkalemic episode have further marginal reduction in CV, on top of any pre-existing conduction abnormalities due to substrate or ionic channel deficiencies. As the disease progresses with age, associated co-morbidities such as kidney disease, which has a hyperkalemic effect, have been reported in ACM [133]. This extra CV modulating factor will increase the likelihood of arrhythmogenesis also due to a shorteing of the action potential [124]. ACM patients are known to have a high ectopic burden[139] and an already slow and inhomogeneous ventricular propagation, hence the time window for ectopic-triggered reentrant arrhythmias will be even larger given a slower CV and a shorter action potential duration under hyperkalemia [140].

2.4.4 Low extracellular potassium illicits biphasic response of CV

Hypokalemia, or an abnormally low concentration of $[K^+]^o$ in the blood is a well established pro-tachicardic factor. Recent animal studies show it can lead to prolongued ventricular repolarisation, slowed conduction and conduction block [141]. We have investigated the effect of hypokalemia on cardiac electrophysiology and CV. Competing effects are observed and illustrated in Figure 2.4.
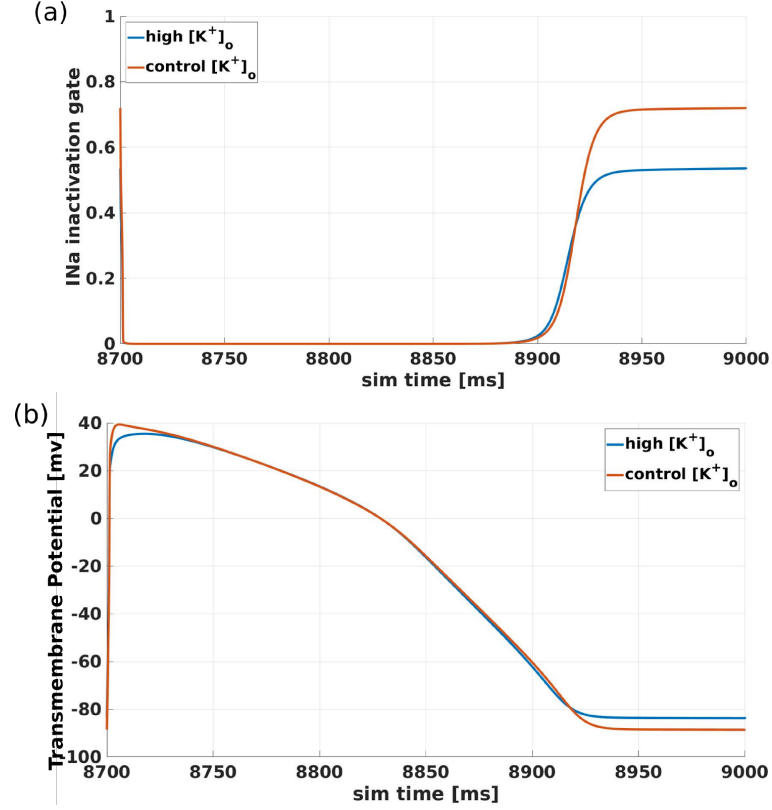
Figure 2.3: (a) A high extracellular $[K^+]^o$ equivalent to 20% above control (6.48 mM) has the effect of hindering full recovery from inactivation of the I_{Na} gate. This is the governing factor behind the slower CV observed. Notice that the resting membrane potential in (b) is higher due to the reduced diffusion gradient.
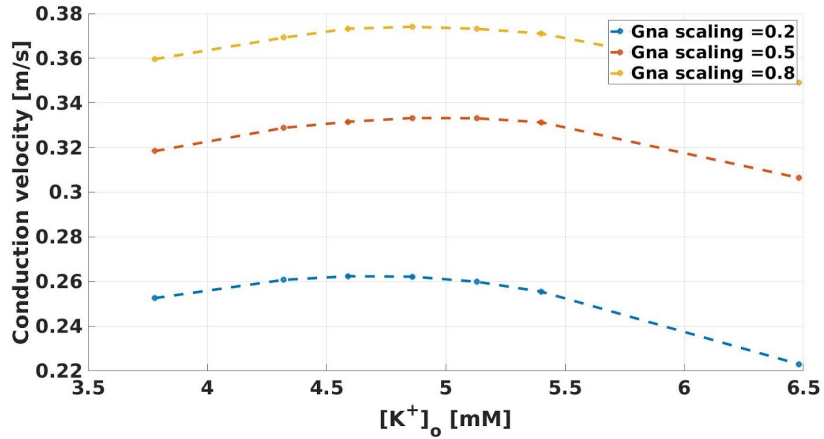
Figure 2.4: CV in a 1D fiber at BCL=300ms, at different concentrations of extracellular potassium. A scaling of 1 represents a control $[K^+]^o$=5.4mM. Notice that a hyperkalemic scenario rapidly decreases the CV for all combinations of the (G_{Na} , G_{K1}) ionic complex studied.

The CV can be increased due to an increased I_{Na} availability due to an enhanced recovery from inactivation. A low $[K^+]^o$ increases the diffusion gradient across the cell membrane and hence a more negative equilibrium potential is required to balance the flux of ions out of the cell, resulting in hyperpolarisation (Figure 2.5a). Contrary to the effect of hyperkalemia, hypokalemia fully opens the voltage-dependent I_{Na} inactivation gates, once the cell has recovered (Figure 2.5b). Furthermore, the lower $[K^+]^o$ availability directly reduces the function of the fast delayed potassium rectifier current I_{Kr} (Figure 2.5c). This, in combination with a more prominent I_{Na} spike and more negative resting membrane potential, increases the repolarisation time of the ventricular myocyte, leading to a prolonged APD, as experimentally confirmed in hypokalemia [141]. An ACM patient with already low CV in certain areas of the ventricle, owing to low I_{Na} availability, connexin protein density and/or structural barriers to conduction is likely to experience a cardioprotective CV increase in the case of mild hypokalemia in the blood. Increasing conduction velocity is likely to reduce the risk of lethal arrhythmias [124], provided the increase in CV is globally homogeneous for the whole organ. This cardioprotective hypothesis can potentially explain thes reports of ACM patients recovering from persistent arrhythmias once their $[K^+]^o$ values were raised back from severe hypokalemia (2.5mM) to approximately 4mM [119].

The system shows a biphasic response to low $[K^+]^o$. At very low $[K^+]^o < 4.6mM$, the delay in conduction due to lower resting membrane potential outweighs the speed up due to higher I_{Na} availability in our simulations, ultimately resulting in a slower CV for hypokalemic ventricular 1D fibers. This effect will be pro-tachicardic for the ventricles of an ACM patient [124], as it will increase heterogeneity of depolarisation times in the ventricles, which is shown to lead to increased arrhythmogenesis in 2D tissue simulations, when a structural scar substrate is already present [142]. The APD prolongation due to lower I_{Kr} activity, mediated by a low $[K^+]^o$ concentration is likely to be cardioprotective as it will reduce the number of possible re-entry combinations available to the wavefront as a larger part of the myocardium will be unexcitable at any one time. Confirmation of these hypotheses warrants a whole organ simulation study.

2.5   Discussion

Emerging electrophysiological consensus is that ion channels coexist in their macro-molecular multiprotein complexes [143] and alterations to genes and protein expres-
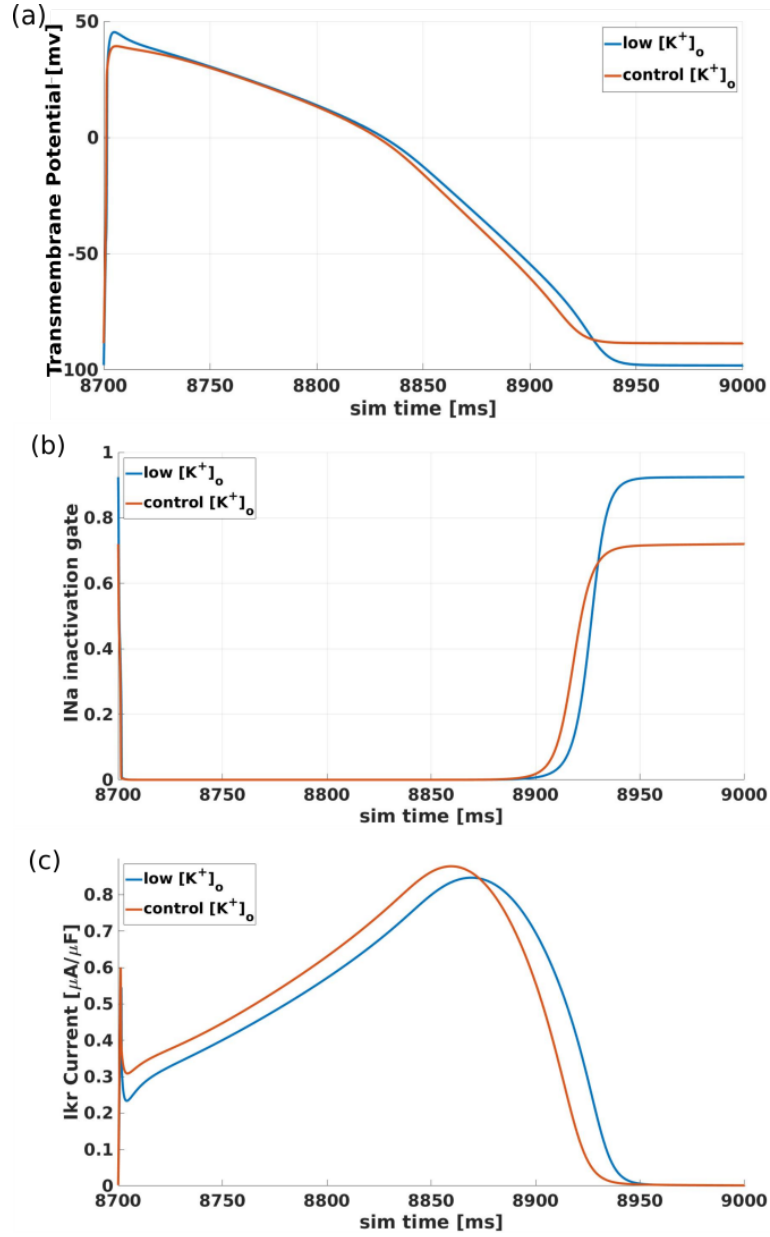
Figure 2.5: (a) The AP shape of a myocyte belonging to hypokalemic human ventricular single cell, parametrising $[K^+]^o = 3.78$ mM or 30% less than the healthy control. Notice the higher peak amplitude of the hypokalemic simulation, due to an increased availability of I_{Na}, as shown in (b), as well as prolonged repolarisation stage and lower resting membrane potential. The APD prolongation is due to the decreased I_{Kr} current, whose output is negatively impacted throughout the cell cycle by the low $[K^+]^o$ and shown in (c).

sion leads to co-adaptation of the channels in the complex. It is important to understand the mechanistic link between genetic mutation and an electrophysiological manifestation of disease in ACM, namely CV slowing, as it is one of the disease

phenotypes present amongst many ACM genetic mutations in the ventricular human myocardium [118] [51]. In ACM, strong experimental evidence shows remodelling of the I_{Na} channel at single cell [144] and whole organ level [118]. Few studies have performed patch clamping and protein expression analysis on the I_{K1} channel yet data in zebrafish ACM models suggest combined modulation of I_{Na}-I_{K1} conductances [2]. Mean 1D fibre human ventricular CV was computed for a set of 3 parameters (INa_{fast}, I_{K1} , $[K^+]^o$). The I_{Na}˘I_{K1} ionic channel complex was confirmed to have an effect on global CV. This in silico study found that a positive correlation between I_{K1} conductance and CV velocity is present only at short cycle lengths ($<$300 ms) and is very marginal. At higher BCLs, the CV was found to be governed entirely by the I_{Na} channel conductance. A finding is the biphasic response of the CV under hypokalemic conditions is preserved in an updated version of the O'Hara Rudy model [134]. The original dependence of CV on $[K^+]^o$ was shown computationally in a sheep Purkinje strand study [145], where the inverse parabolic CV profile with respect to $[K^+]^o$ was first shown. The dependence of CV on I_{Na} alone was also previously studied computationally and the two were found to be intimately linked and that the L-type calcium current supports conduction only for values of G_{Na} below 30% of control [146]. A speed up in CV is observed for mild hypokalemic episodes and a slow down of CV in acute episodes, indepedent of (I_{Na}, I_{K1}) conductances. Based on experimental data in rat patch clamp experiments [1], the peak conductance co-modulation factor of G_{Na} when G_{K1} is reduced is 1.4, meaning a reduction of 50% in G_{K1} peak inward conductance will induce a 70% peak conductance reduction in G_{Na}. Data on the reciprocal relationship was not found. Currently, there is no data in the literature to validate these findings in human cells, yet experimental work can pave the way for co-modulation being incorporated in computational human ventricular models. The work is contextualised with regards to ACM ventricular dynamics, namely that a reduction in I_{Na} conductance and/or I_{K1} via an indirect influence on I_{Na}, a hyperkalemic or hypokalemic episode are all likely to increase susceptibility to life threatening arrhythmias in ACM patients given that they will reduce conduction velocity and increase heterogeneity of depolarisation times [147]. The only exception is in the case of mild hypokalemia ($<$10% change in baseline $[K^+]^o$) , where the CV is expected to increase by a few percent.

Chapter 3

MRI-informed modelling and simulation highlight the role of Purkinje and myocardial fibrosis in QRS abnormalities in Arrhythmogenic Cardiomyopathy

3.1   Abstract

The goal of this study is to investigate the electrophysiological and structural re-modelling explaining distinct QRS complex phenotypes in ACM. Human anatomical torso-biventricular models were constructed from cardiac MRI of ACM patients, with different degrees of QRS abnormalities. Computer simulations were conducted to dissect the contribution of ACM abnormalities such as 55% increase in RV end diastolic volume, 30% reduced wall thickness, conduction slowing in myocardium and in the Purkinje-endocardial layer. QRS complexes were reconstructed from the simulated sinus rhythm activations and assessed based on their ability to reproduce ACM-specific QRS features, namely prolonged QRS > 100 ms, terminal activation duration (TAD) > 55 ms, low R-wave amplitudes < 2 mV, and loss of R-wave progression across precordial leads.

Computer simulations demonstrate that, in ACM, mild QRS prolongation (>100 ms), in absence of other QRS abnormalities, is explained by regional myocardial conduction slowing in the areas of MRI-identified fibrosis. However, MRI-based fibrosis and RV chamber dilation alone proved insufficient to recapitulate more severe QRS abnormalities, such as severely prolonged mean QRS duration (>120 ms) across precordial leads, mean TAD across V1-V4 (>55 ms), and low QRS mean R-wave

amplitude (<2 mV) in precordial leads, as well as poor R-wave progression. A 70% decrease in Purkinje-endocardial conduction and 30% RV wall thinning were required to explain these more severe abnormalities. An analysis of additional substrates on the QRS complex shows the effects of global myocardial conduction slowing, RV myocardial conduction slowing, regional fibrosis-mediated conduction slowing and Purkinje-endocardial conduction system slowing all have distinct effects on the QRS complex features of an ACM patient.

3.2   Introduction

The diagnosis of ACM is challenging and requires complex scoring systems, combining multiple diagnostic modalities, namely the electrocardiogram (ECG) and magnetic resonance imaging (MRI) amongst others. Risk stratification is also complex due to the wide range of phenotypes affecting both ventricles and guidelines remain generic without addressing specific ACM phenotypes [148]. In the context of the evolving paradigm of precision medicine, identification of the pathophysiological mechanisms underlying different disease phenotypes in ACM is therefore critical to enable more patient-specific treatment recommendations and refine diagnosis.

Diverse QRS abnormalities are clinically recognised in ACM, including prolonged QRS duration, QRS fragmentation, reduced QRS amplitudes, poor R-wave progression, or prolonged S-wave terminal activation duration (TAD) in the absence of complete right bundle branch block [149]. Prolonged TAD has been included in the 2010 Task Force criteria for diagnosis of ACM [3], and confirmed as one of the most discriminatory ECG features, used for differentiating ACM from other clinical entities in the latest 2019 expert consensus report [19]. Yet, the mechanisms underlying specific QRS abnormalities in ACM remain elusive. Several electrophysiological and structural components of the disease have been postulated as causal factors, including sodium channel dysfunction [144], right ventricle (RV) dilation [150], RV wall thinning [17], fibrofatty replacement of the myocardium [151] and/or of the fast conduction system [116]. Dissecting the contribution of each factor is challenging using clinical or animal studies, due to concomitant effects and current technical limitations. In particular, fibrofatty replacement, as identified by late gadolinium enhanced (LGE) MRI, is a diagnostic hallmark and collocalises with conduction slowing in ACM in ECGI studies [139].

Computer simulations using cardiac MRI-informed human torso-heart models allow the quantitative assessment of the contribution of each electrophysiological and

structural factor on the ECG, as recently shown in hypertrophic cardiomyopathy [152]. Other in silico studies have shown the contribution of anatomical heart-torso variability on QRS morphology [153], the contribution of mechanical deformation on the ECG during systole [154], have assessed how acute ischemic events translate into deviations of the ST-segment and arrhythmic risk [155] and have investigated the contribution of heterogeneity in the activation sequence on the ECG in heart failure patients [156]. Whilst some computational studies investigating pump function in ACM exist [157] [158], no previous work has used in silico modelling and simulation to elucidate the origin of QRS abnormalities in this disease.

The goal of this mechanistic study is to relate the key structural and electrophysiological ventricular remodelling to the QRS abnormalities identified in ACM patients using MRI-informed computer modelling and simulation. We quantify the implications on the QRS complex of ACM-related remodelling, including RV dilation, wall thinning and fibrotic infiltration, as well as slow propagation in the myocardium and the Purkinje-endocardial layer, providing links between the underlying remodelling and the measured clinical QRS features. We hypothesise that, in ACM, myocardial conduction slowing in areas of LGE MRI-identified fibrosis can explain QRS and TAD prolongation, without introducing changes in QRS morphology, whereas morphological QRS abnormalities such as low amplitude R-waves and abnormal R-wave progression, alongside severe QRS and TAD prolongation in the precordial ECG leads, are caused by abnormal Purkinje-endocardial activation and anatomical dilatation. Simulations using MRI-informed human torso-biventricular models highlight a prominent role of abnormal Purkinje-endocardial conduction in mediating morphological QRS interval abnormalities in ACM.

3.3 Methods

3.3.1 Clinical Data

Twenty subjects, including 15 definite, 3 borderline and 2 possible ACM diagnosed patients following the 2010 ACM Task Force criteria [3] underwent a complete assessment at the Heart Hospital (London, UK), including high resolution, motion corrected 1.5 Tesla cine MRI, LGE-MRI, ECGI, and genetic testing. Informed consent and local ethical approval were obtained for the study. LGE-/MRI based intensity thresholding was used to extract regions of fibrosis from the ventricles of the patients. A summary of the anatomical, structural and electrocardiographic evaluation of the cohort is presented in Table 3.1. The data was published in full in a previous study [139]. 12-lead

ECGs were reconstructed from the body surface potentials, recorded in standard lead positions. The ECG features of a separate cohort of 42 definite ACM patients, according to the 1994 Task Force Diagnosis Criteria, were used to contextualise our ACM cohort [159].

3.3.2 MRI-based heart-torso models for ECG simulation

MRI-based anatomical torso-biventricular models were reconstructed as illustrated in Figure 3.1, based on the MRI datasets [139], as described in more detail in the Appendix Section A.1.2 of this thesis. In brief, MRI images of the heart/torso were aligned to correct for breathing artefacts, and LV/RV endocardial, LV epicardial and torso surfaces were contoured. Initially, a uniform wall thickness of 3 mm was assigned to the RV, given the limitations of MRI to resolve the RV epicardial surface. The inability to resolve the RV wall thickness on all of the MRI stack is shown in the Appendix Figure A.2. Uncertainty in the location of the RV epicardial surface grows as the scanner moves from the RV base to the apex of the ventricle. The contours were used to fit 3D finite-element meshes of the ventricles and torsos of the subjects. The above geometry extraction pipeline was developped by Ernesto Zacur and adapted to ACM meshes by the candidate. The process involved testing and debugging the pipeline for new patient geometries, as well as working with the creator to devise algorithm and code improvements.

Simulated activation sequences were computed on the constructed ventricular geometries using the Eikonal equation [160]. This simplified model of electrical propagation computes the time at which each microscopic muscle volume in the ventricles was excited, based on a shortest path algorithm. As in previous studies [152] [161] [162], the activation sequence was initiated using a phenomenological description of the ventricular trifascicular conduction system, by stimulating the inceptions (root nodes) of the free-running Purkinje system with the ventricular myocardium, then rapidly propagating on the endocardial surface. A conduction speed within physiological range (170 cm/s) was imposed on the endocardial layer, as calibrated in a previous study to obtain realistic QRS complexes [161]. LV locations of the root nodes were selected to correspond to the same anatomical locations producing a healthy reconstructed QRS sequence and validated against ex-vivo human activation sequence experiments [163]. A larger variability in the locations of the end points of the trifascicular conduction system in the RV was observed by identifying the sites of earliest epicardial breakthrough on the ECGI epicardial surfaces. Hence, the root nodes in the thinner RV were adapted for each patient to obtain RV epicardial breakthroughs at the same

Patient ID	Age	Gender	LV/RV Dilation	LV/RV Wall Thinning	LV/RV LGE +	QRS Prolongation	TAD Prolongation	Absence of R-wave progression
1	59	M	No/Yes	No/No	Yes/No	Yes	No	No
2	63	M	No/Yes	No/No	No/No	No	Yes	No
3	54	F	No/Yes	No/No	No/No	No	No	No
4	44	M	No/No	No/No	No/No	Yes	Yes	No
5	55	M	No/Yes	No/No	No/Yes	Yes	Yes	No
6	63	M	No/Yes	Yes/Yes	No/Yes	Yes	Yes	Yes
7	59	M	No/Yes	No/No	No/Yes	Yes	No	No
8	69	F	No/No	No/No	No/No	No	No	Yes
9	61	M	No/No	No/No	No/Yes	No	No	No
10	41	F	No/No	No/No	No/No	Yes	No	No
11	49	F	No/Yes	No/No	Yes/No	Yes	No	No
12	60	M	No/Yes	No/No	NA	Yes	Yes	No
13	26	M	No/No	No/No	No	Yes	Yes	Yes
14	66	M	No/Yes	No/Yes	Yes/Yes	Yes	No	No
15	54	M	No/No	No/No	Yes/No	Yes	Yes	Yes
16	74	M	No/No	No/No	NA	Yes	Yes	No
17	24	M	No/No	No/No	No/Yes	No	No	No
18	54	M	No/No	No/Yes	Yes/Yes	Yes	No	No
19	39	M	Yes/Yes	No/No	No/Yes	Yes	Yes	No
20	75	M	No/No	No/Yes	Yes/Yes	Yes	No	No

Table 3.1: Anatomical and structural evaluation of our clinical cohort of 20 ACM patients. The patients highlighted were analysed in more detail using personalised ventricular simulations.
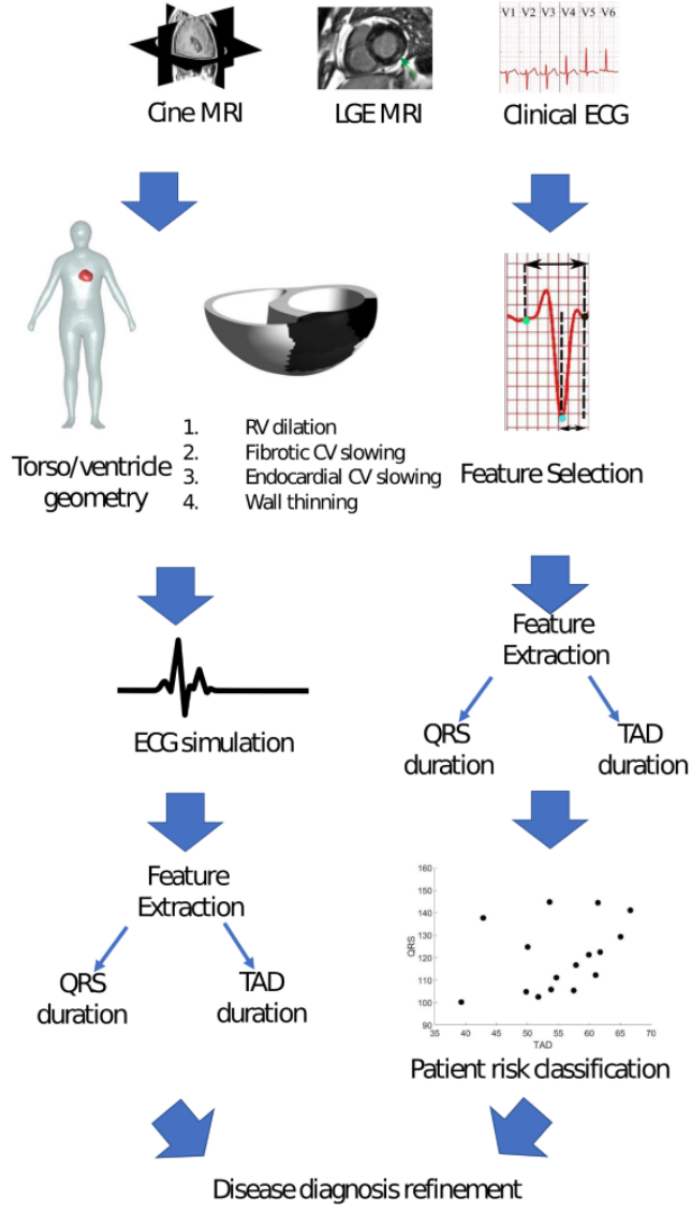
Figure 3.1: (left column) Computational pipeline for activation sequence and QRS complex simulations from MRI-informed torso/biventricular models was used to test hypotheses about the nature of remodelling in ACM patients' ventricles. The effect of anatomical (RV dilation and wall thinning), structural (myocardial LGE and Purkinje-endocardial layer fibrosis) and ionic (global and ventricle specific CV slowing) ACM remodelling on the QRS complex were studied. (right column) The clinical ECG data were post-processed and features of the signals were extracted, namely QRS, TAD and signal amplitudes. Patients were clustered in feature space. Features values and ECG morphology were compared between the clinical and simulation based ECGs on a patient basis in order to assess the validity of the substrate hypotheses in the simulations.

location as in the corresponding ECGI dataset. A more detailed description of the model parametrisation is provided in the Appendix Section A.2.2. The implementation of the solution of the Eikonal equation was developed by Julia' Camps, with the contribution to the method development of the candidate being the incorporation of fibrosis into the models and the distributed computing (parallelisation) setup of the code, which led to a 64 times speedup in computation time.
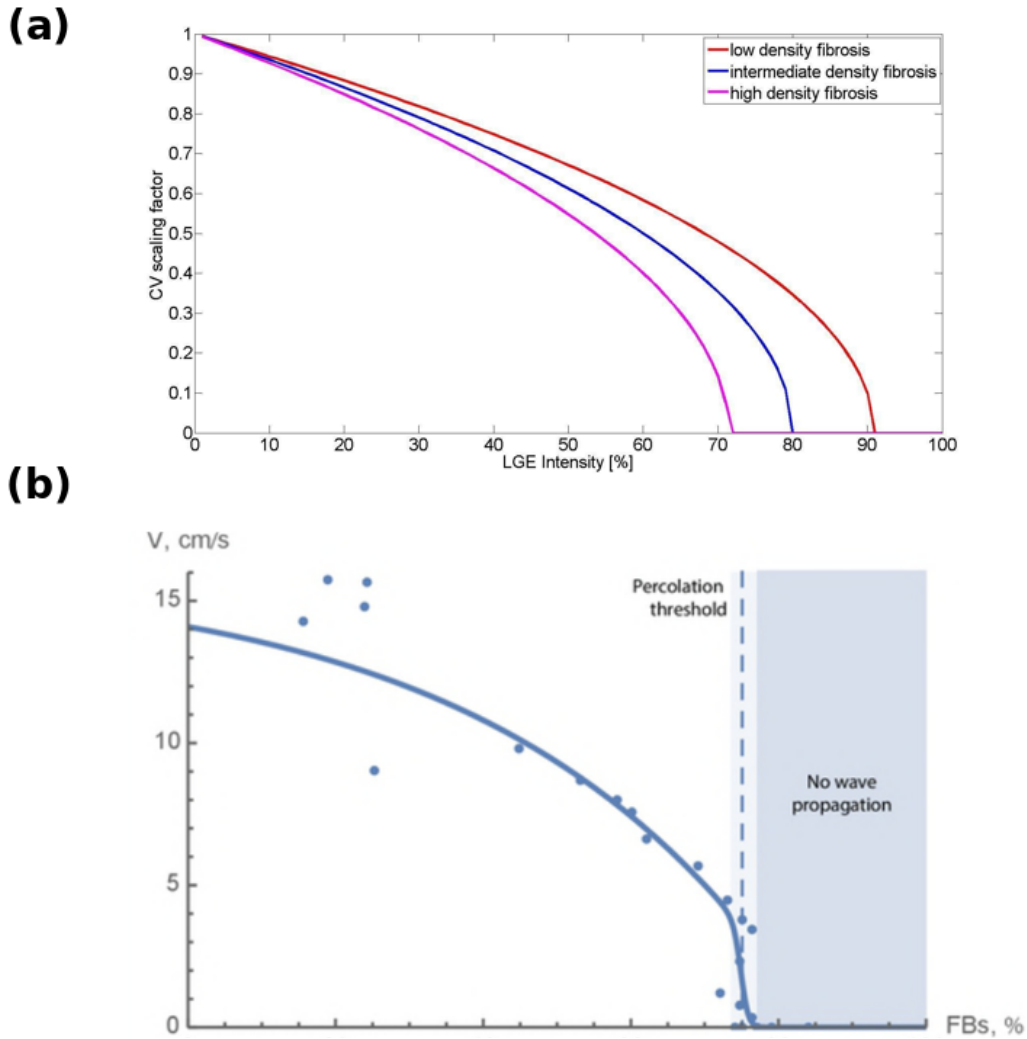
Figure 3.2: Modulation of conduction by fibrosis. A. Scaling of conduction velocity in LGE-regions for the three densities of fibrosis tested. No LGE-regions had a fibrotic intensity greater than 65% in our ACM patients, and hence conduction block was never modelled. B. Experimental modulation of conduction velocity in the presence of increasing fibroblast content [164]. Reproduced under CC-BY 4.0 Open Access license.

Once the activation sequence was simulated in the torso-biventricular anatomical model, the 12-lead ECG was computed at standard lead locations placed on the torso, as explained in Appendix Section A.1.3. In all figures, grid resolution for ECG visualisation is 40 ms/1 mV.

3.3.3 MRI-informed modelling of ACM-related structural and electrophysiological abnormalities

The effects of fibrosis, as identified by LGE MRI, on myocardial propagation were introduced by decreasing the conduction velocity (CV) in the patients in American Heart Association style regions of the ventricle affected (LGE+) [165]. For each subject, three different fibrotic density curves were used for their LGE-MRI informed models in order to account for uncertainty in conduction properties and given the large variability in fibrotic composition. If the region of fibrosis affliction extended up to the endocardial layer, CV in the fast propagation layer was equivalently reduced.

Different models of fibrosis were tested in our study to account for the effect of varying degrees of fibrotic remodelling onto the 12-lead ECG, as illustrated by the different curves of modulation of conduction velocity by fibrosis content shown in Figure 3.2A. The shape of the tested curves was informed by established theoretical results on the square-root modulation of conduction velocity with respect to myocardial conductivity [166], as well as by experimental data on fibroblast-modulated conduction slowing [164], presented in Figure 3.2B. Hence, the uncertainty of conduction modulation via fibrotic scar tissue was explored by testing several strengths of fibrosis in our simulations and evaluating their impact on the QRS complex. To incorporate this information into the Eikonal model of conduction, the following approach was used. The Eikonal model is solved using a non-directed graph-based method [160], where the activation follows the shortest path through the graph. Each edge in the graph is originally assigned a weight based on the Euclidean distance between the two points it connects. An additional distance scaling factor was added between nodes in fibrotic regions, slowing the signal propagation between them.

ACM is also known as a disease of the desmosomes [144], in which cell-cell decoupling and other genetic causes can potentially lead to a slower global conduction in the myocardium. This was considered in the models by scaling the global tissue CV by factors in the range 25-95%. The results from tissue-level simulations in Chapter 2 suggest that up to 45% CV velocity modulation can be attributed to I_{Na}-I_{K1} imbalances at cellular level. Further reductions can be attributed to structural gap junction loss of integrity, cell-cell uncoupling, changes in cell shape [4] and density

of channel forming connexin proteins [88]. Reductions of CV of more than 70% are thought to be unlikely in living patients yet are included to ellucidate the effect of CV modulation on QRS features more clearly.

Furthermore, the effect of fibrofatty replacement affecting of the fast conduction system [116] was investigated by considering up to 70% reduction in Purkinje-endocardial layer speed. This is supported by 3D electroanatomical mapping recordings in ACM [159] showing that total endocardial activation times were significantly prolonged in ACM.

Finally, ACM-related gene mutations lead to uncontrolled myocyte inflammation and subsequent apoptosis, where the myocardium is progressively replaced by a fibrofatty substrate. This effect is especially prominent in the relatively thinner RV wall [167], where wall thinning can be very severe, with little surviving myocardium present at post-mortem examination. This effect was incorporated by reducing the thickness of the RV wall from 3 mm to 2 mm, in agreement with RV wall thickness reported for a cohort of 30 ACM patients [167]. The factors of ACM remodelling accounted for in this study are summarised in Figure 3.1b.

3.3.4 ECG Features

The simulated and clinical QRS complexes were compared focusing on ACM-related abnormalities, namely QRS duration, TAD, R-wave progression and R-S amplitude ratio, as highlighted in the clinical diagnosis guidelines [3]. The R-wave peak is defined as the maximum point on the curve when an R-wave is present. The Q-point on the precordial leads of the ECG is defined as the first point of negative gradient before the R-wave upstroke. The nadir of the S-wave is the minimum voltage of the QRS complex. TAD is defined as the mean across V1-V4 of the time interval from the nadir to the end of the S-wave, the point at which the voltage returns to the isoelectric value for the first time after the S-wave nadir [168]. QRS duration is the mean time elapsed between the Q wave start and S-wave end point across precordial leads. Clinically, a TAD of over 55 ms in the precordial leads and filtered QRS duration greater than 114 ms are both minor ACM diagnosis criteria. The QRS features are labelled on the QRS complex in Figure 3.3A. A healthy R-wave progression across precordial leads is present when the R-wave amplitude grows steadily from V1 through the precordial leads, reaching a maximum before V6, then decreasing marginally. We propose the following criteria for the quantitative categorisation of the absence of R-wave progression (R+) in ACM: (i) low amplitude R-waves of less than 2 mV in all

precordial leads; (ii) R-wave to S-wave amplitude ratio less than 0.5 in V1-V4; and (iii) absence of inverse parabolic progression in R-wave amplitudes across V1-V6.
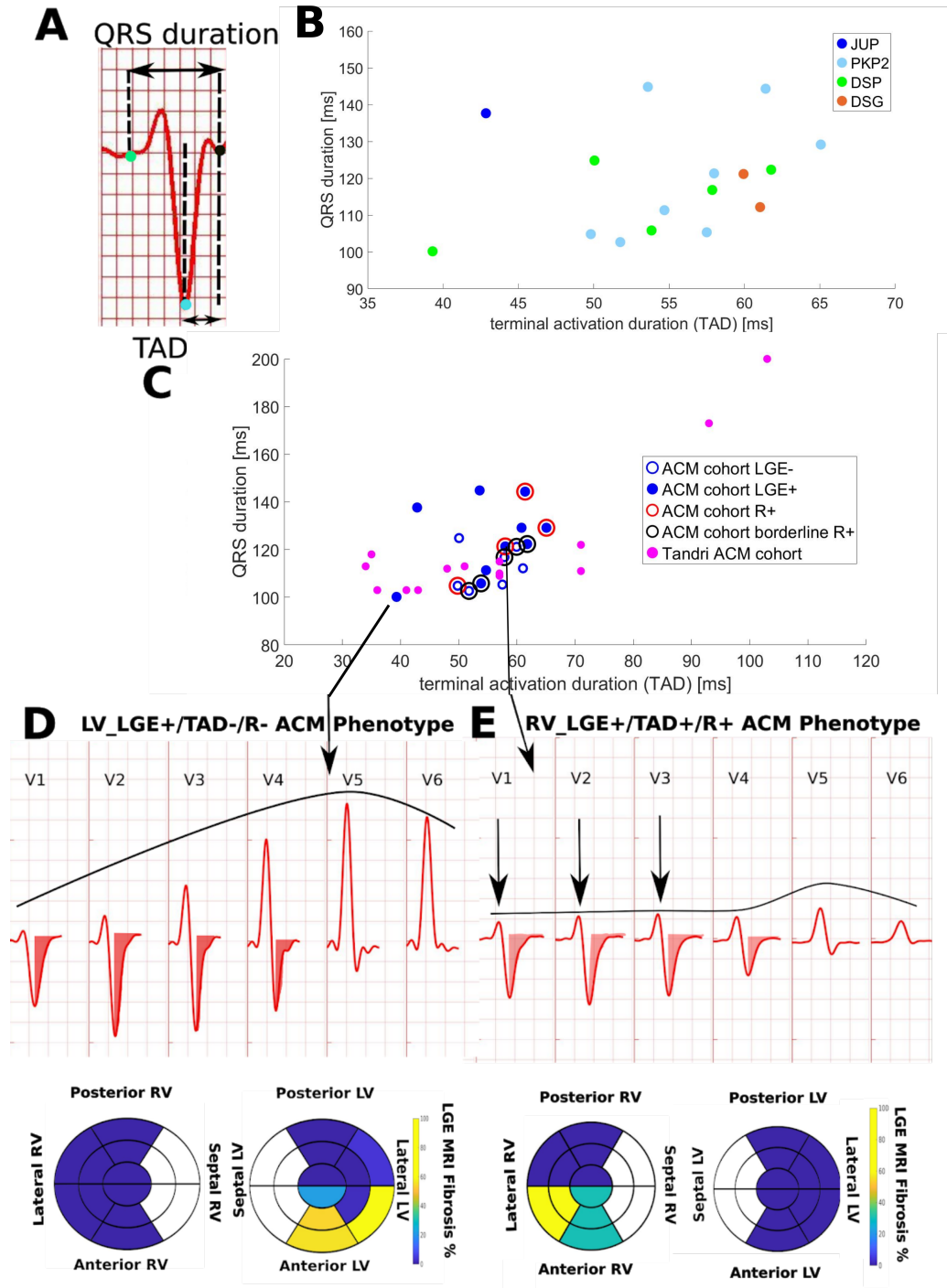
Figure 3.3: A. Example of QRS feature extraction. The QRS complex is defined as the time interval between the start of the Q wave (green circle) and the end of the ventricular activation, when the potential returns to the isoelectric value (black circle). TAD is measured from the nadir of the S-wave (turquoise circle) and the end of the QRS complex. B. QRS features in our ACM cohort do not cluster by genetic provenance (different colours). Patients with no genetic mutation were excluded from this plot.

Figure 3.3: C. Distribution of QRS features in different ACM cohorts. Open/filled blue symbols indicate LGE negative/positive (LGE-/LGE+) patients in our ACM cohort, respectively. Three patients did not exhibit evident S-waves and were excluded from visualisation. Patients with definite (red circles) and borderline (black circles) loss of R-wave progression appear in the upper quadrant of protracted QRS width and TAD values. Results are presented for comparison against an independent ACM cohort (filled magenta symbols, no LGE data available). D. QRS complex in precordial leads of ACM LGE+ patient with moderately prolonged QRS duration and TAD<55 ms (TAD-) and LGE transmural fibrosis in the LV anterior/anterolateral AHA segments. E. QRS complex in precordial leads of ACM LGE+ patient with prolonged QRS duration of 120 ms and TAD≥55 ms (TAD+), low amplitude signal (downward arrows), absence of R-wave progression and transmural LGE fibrosis in the RV anterior and anterolateral free wall in AHA plot. Grid resolution: 40 ms/1 mV. Black lines highlight R-wave progression pattern.

3.4 Results

3.4.1 QRS-based phenotypes of ACM in LGE positive patients

QRS duration versus TAD feature values for our ACM cohort are presented in Figures 3.3B and 3.3C. Genetic mutations did not cluster in the feature space, and hence could not explain differences in feature values (Figure 3.3B). Regardless of LGE classification, both QRS duration and TAD features progress from moderately prolonged to significantly protracted values, spanning the entire feature space, and highlighting an absence of correlation between LGE+/LGE- evaluation and QRS-derived features (Figure 3.3C, filled vs open blue symbols). The same distribution of QRS biomarkers was also observed in an independent ACM cohort [159], as shown in Figure 3.3C (magenta symbols). An absence of R-wave progression phenotype, spanning the entire range of the QRS duration and TAD feature space, was found in several of the ACM patients. Two very distinct QRS phenotypes, presented in Figures 3.3B-C, were taken from the feature space of LGE+ patients and studied in detail.

On the one side of the spectrum is an ACM LGE+ phenotype having no apparent QRS abnormalities. This phenotype presents a QRS duration of 100 ms across precordial leads, which is in the upper limit of the healthy range, and TAD<55 ms (TAD-). This was regardless of fibrotic replacement diagnosed by LGE-MRI, which was observed to coexist with delayed activation (high isochrones density) in fibrotic regions in ECGI examination [139]. Conversely, on the opposite side of the spectrum is an ACM LGE+ phenotype with multiple QRS abnormalities, involving prolonged QRS duration, TAD≥55 ms (TAD+) as ACM Task Force 2010 criteria, and absence of R-

wave progression. The patient was LGE+ in the RV anterior free wall, also revealing marked RV dilation and RV wall thinning in MRI examination. For completeness, the clinical presentations of both phenotypes will be referred to as LV_LGE+/TAD-/R- and RV_LGE+/TAD+/R+, as outlined in Figures 3.3D-E.

3.4.2 The role of right ventricular dilation on QRS features

The role of RV dilation was examined by mapping an identical start of ventricular activation in positive and negative RV dilated patients, then allowing cardiac conduction to proceed under healthy myocardial conditions, as detailed in the Appendix section A.2.

The simulated activation sequences for the LV_LGE+/TAD-/R- and RV_LGE+/TAD+/R+ phenotypes are presented in Figures 3A and 3B, respectively demonstrating similar total activation times, except for delayed activation in the RV base of the dilated ventricle. Despite similarities in activation sequences, the inherently different geometries resulted in substantially different QRS complexes (Figure 3.4C). The non-dilated ventricles gave rise to a normal QRS complex in all precordial leads, with regular R-wave progression (increasing from V1 to V5, and decreasing in V6), and QRS width and TAD in the normal range. On the contrary, activation on the dilated RV ventricles produced S-wave overshoots in V1-V3 and reduced R-wave amplitudes in V3-V4. This is explained by the dilation around the RV septal insertion point (Figure 3.4B, white arrows), and the fact that leads V3-V4 reflect septal activation. Hence, although RV dilation can produce significant QRS abnormalities in precordial leads, it was insufficient to explain the characteristic QRS features exhibited by the RV_LGE+/TAD+/R+ ACM phenotype. For reference, a simulated activation map and the associated QRS complexes of a control subject are included in Figure 3.4D and E respectively, illustrating a healthy activation sequence and R-wave progression, as no dilation or conduction abnormalities are present.

3.4.3 LGE-MRI informed modelling explains clinical QRS features of the LV_LGE+/TAD-/R- ACM phenotype

We hypothesised that borderline QRS duration, in the upper limit of the normal range, is attributed to the late activating fibrotic region in the LV anterior wall, given a healthy ventricular anatomy in Figure 3.4A. In order to model fibrofatty replacement, LGE+ regions were imposed by introducing conduction slowing and testing different levels of conduction modulation, in order to account for uncertainty in the translation
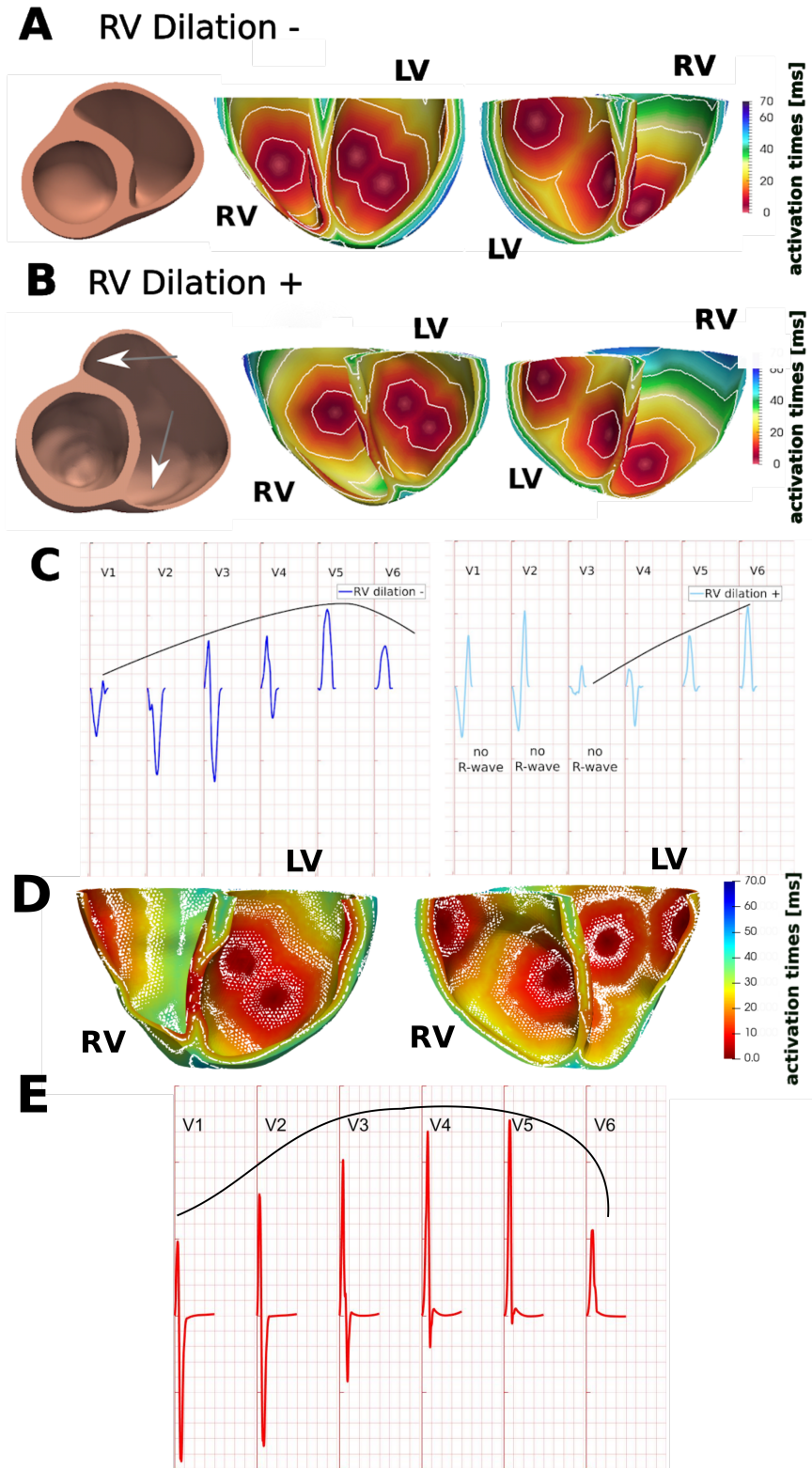
Figure 3.4: Role of ventricular dilation on QRS complex. A. Control simulated activation sequence for LV_LGE+/TAD-/R- ACM phenotype, presenting no anatomical abnormalities.

Figure 3.4: B. Control simulated activation sequence for RV_LGE+/TAD+/R+ ACM phenotype, presenting marked RV dilation. Arrows indicate regions of prevalent dilation at RV septal insertion. C. Reconstructed QRS complexes from results in panels A and B. The non-dilated geometry showed healthy QRS and R-wave progression (left panel), while the dilated geometry (right panel) produced an abnormal S-wave overshoot and an absence of R-wave in leads V1-V3D. The activation sequence for a subject with control geometry. The root nodes are placed in standard locations, mimicking experimental findings by Durrer [163] for earliest epicardial breakthroughs. E. The simulated QRS complex precordial leads for the activation sequence shown in D , showing good R-wave progression across precordial leads with R-waves increasing from V1-V5 and decreasing in V6. . Isochrones separation: 10 ms. Black lines highlight the R-wave progression pattern.

of LGE-MRI measurements into conduction properties. Simulated QRS complexes in precordial leads for low (40% slowing, light blue traces), intermediate (50% slowing, green traces) and high (60% slowing, orange traces) fibrotic densities are shown in Figure 4A. LGE-MRI informed models exhibited increasingly prolonged TADs (and therefore QRS widths) for increasing values of conduction slowing, still preserving a normal R-wave progression up to a conduction slowing of 50%. If this threshold was exceeded (orange trace), QRS morphology deviated from the clinical phenotype.

The corresponding epicardial views of ventricular activation for control, low, intermediate and high fibrotic densities are presented in Figure 3.5C, exhibiting areas of increasingly dense isochrones at the LV base. Additionally, Figure 3.5D quantitatively summarises the derived QRS complex features for all the fibrotic densities investigated. Of note, the low density fibrotic region, located transmurally in the LV anterior/anterolateral free wall, correctly recapitulates a QRS duration of c.a. 100 ms across precordial leads, whilst only mildly prolonging TAD in anterior leads V2-V4. Therefore, the LV_LGE+/TAD-/R- ACM phenotype could be explained by introducing LGE-MRI information into the model, and this directly translates into mild prolongation of QRS width and TAD in precordial ECG leads. Accessing the difference between the simulated and clinical QRS complexes as mean absolute error between pairs of signals was trialed. It was found to be a metric very dependent on the amplitudes of the signals and hence QRS feature analysis was the preferred way to access similarity between recorded and simulated QRS complexes.
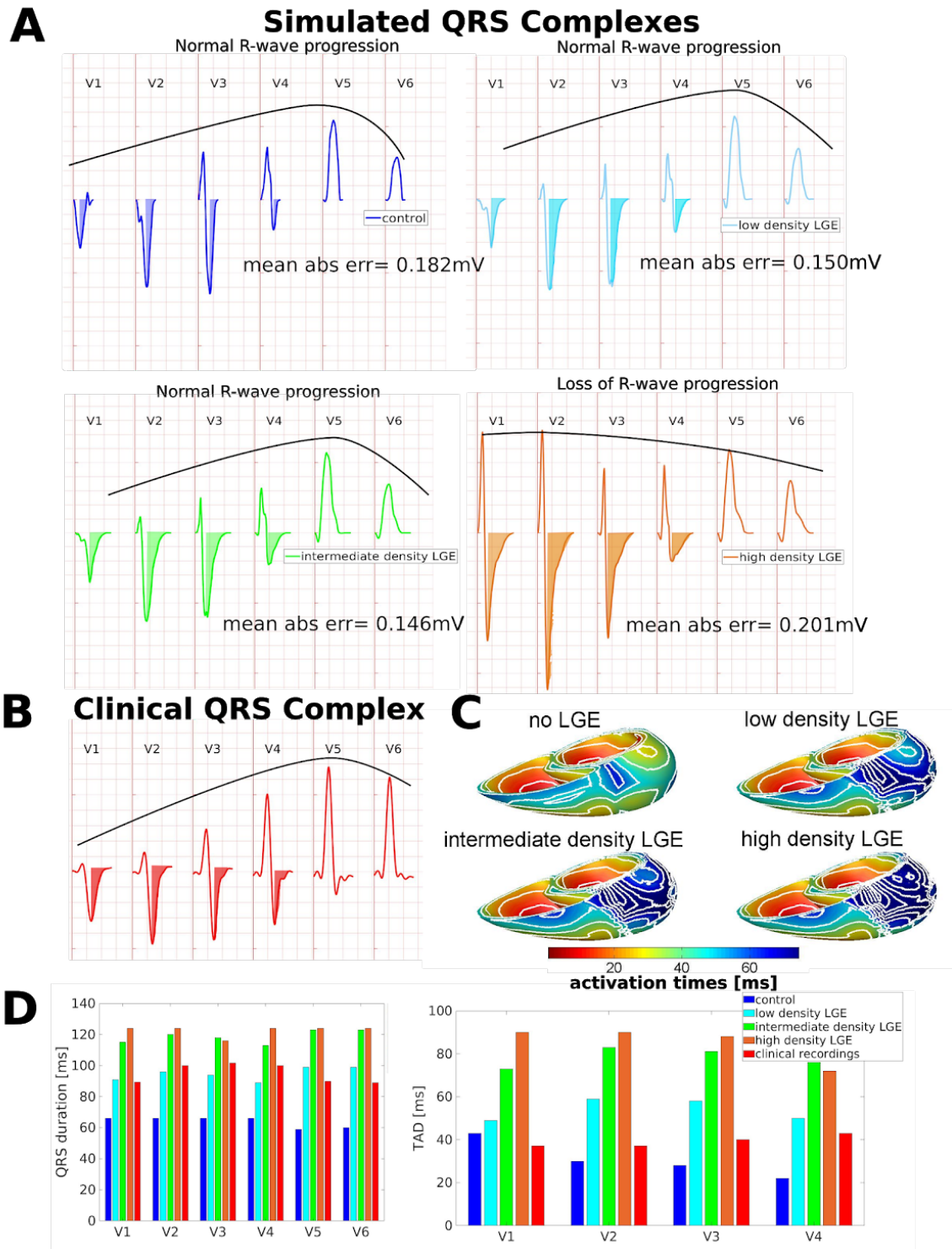
Figure 3.5: A. Effects of fibrofatty replacement, present transmurally in the LV anterior/anterolateral segments, in the LV_LGE+/TAD-/R- ACM phenotype.

Figure 3.5: A. QRS complexes in precordial leads for control versus low (light blue trace), intermediate (green trace) and high (orange trace) density fibrotic patches, located in the LV anterior and anterolateral free wall. Only the most dense fibrotic patch leads to loss of R-wave progression. Black lines highlight the R-wave progression pattern. The mean absolute error is with respect to the clinical QRS. B. Clinical QRS complex of the LV_LGE+/TAD-/R- patient. C. Activation maps for the same conditions as in A. D. Quantification of QRS duration and TAD for different fibrotic densities in LGE+ regions. The difference between the simulated (A) and clinical (B) QRS complexes was reported as mean absolute error between pairs of signals.

3.5 LGE-MRI informed modelling alone is insufficient to reproduce the QRS morphology of the RV_LGE+/TAD+/R+ ACM phenotype

Next, we assessed whether LGE-MRI information is also sufficient to explain the RV_LGE+/TAD+/R+ ACM phenotype, in terms of reproducing its characteristic, extremely prolonged QRS width in all precordial leads, protracted TAD in V1-V4 (including lateral leads V5-V6), low amplitude R-waves, and abnormal R-wave progression.

We translated the LGE+ information, indicating a large transmural fibrotic patch in the anterior/anterolateral RV, into the personalised anatomical model, following the same methodology as for the LV_LGE+/TAD-/R- ACM phenotype. In addition, we personalised the Purkinje inceptions on the RV endocardium in order to replicate the epicardial breakthroughs observed on ECGI. Introducing LGE-MRI information into the model delays activation in the RV anterior and lateral free walls, as highlighted by the activation sequences in Figure 3.6C, eliminating the S-waves in leads V1-V4 (Figure 3.6A). This significantly deviates from the clinical phenotype (Figure 3.6B), where wide and deep S-waves in leads V1-V4 are observed. Hence, LGE-MRI information alone is not sufficient to explain the QRS abnormalities of this phenotype.

The capacity of dysfunctional sodium channels to account for the QRS abnormalities observed in this ACM phenotype was also tested by reducing global conduction speed in the LV and/or RV, as well as in isolation or concomitantly to fibrofatty replacement [144] [101]. No combination of global conduction slowing and/or fibrosis could account for the QRS features of the RV_LGE+/TAD+/R+ ACM patient phenotype, as summarised in Figure .
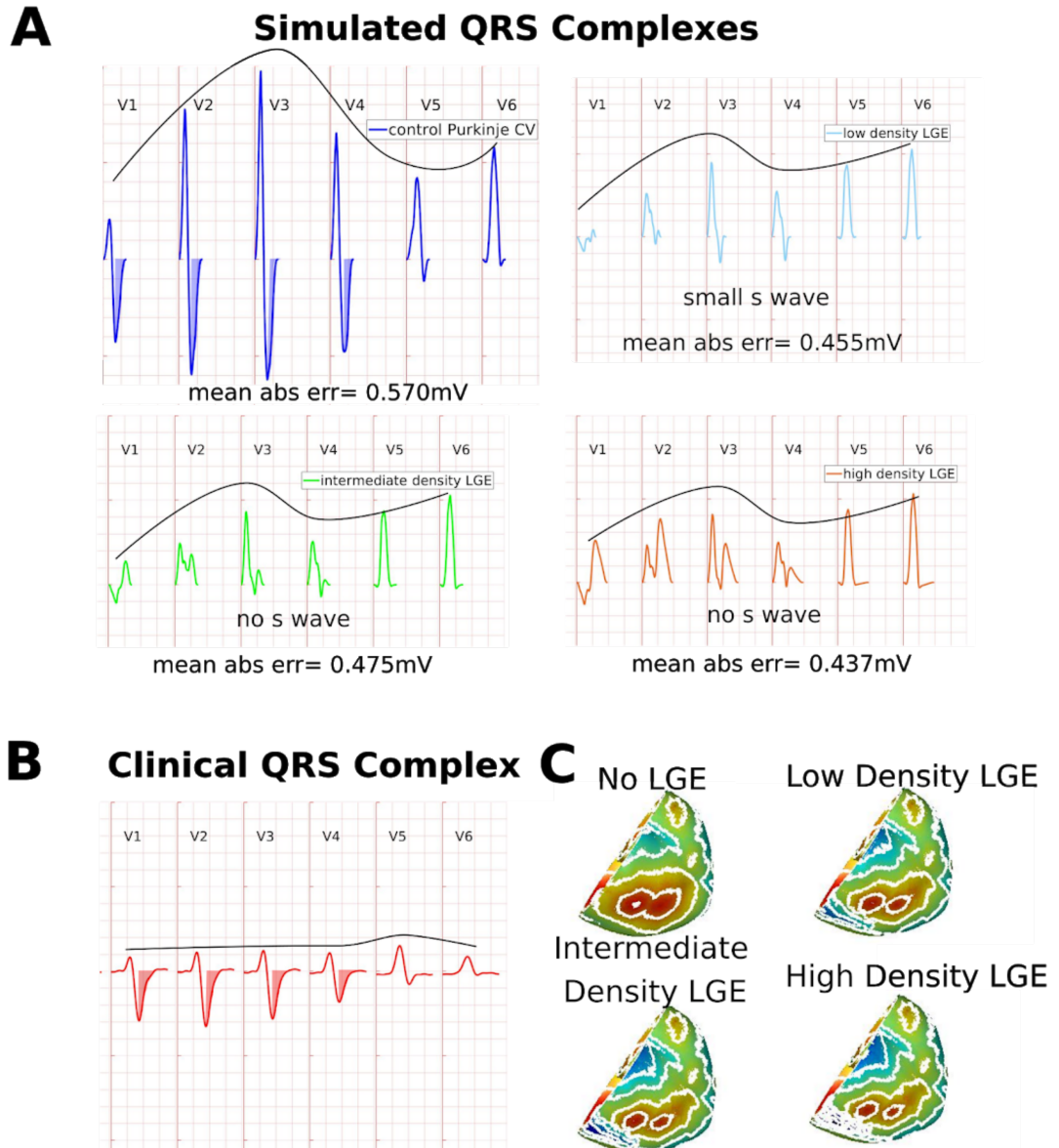
Figure 3.6: Effects of fibrofatty replacement in the RV_LGE+/TAD+/R+ ACM phenotype. A. Simulated QRS complexes for control versus low, intermediate and high density fibrotic patches, located in the anterior and anterolateral RV. The black lines indicate the R-wave progression pattern. The mean absolute error is given with respect to the clinical QRS.

Figure 3.6: B. The clinical QRS complex for the RV_LGE+/TAD+/R+ phenotype. C. Activation time maps for the same conditions as in A. In the absence of additional factors, LGE+ information alone produces QRS complexes which deviate from the clinical phenotype in leads V1-V4. The difference between the simulated (A) and clinical (B) QRS complexes was reported as mean absolute error between pairs of signals.

3.5.1 Fibrofatty replacement of the fast conduction system explains prolonged TAD and absence of R-wave progression of the RV_LGE+/TAD+/R+ ACM phenotype

Fibrofatty replacement of the His-Purkinje system, affecting both its bundle branches, has also been frequently reported post-mortem in ACM [116]. However, it remains overlooked as a causal mechanism of the disease, possibly due to current limitations in LGE-MRI resolution and lack of noninvasive assessment.

In order to ascertain the repercussions of fibrofatty replacement in the fast conduction system on QRS features, the Purkinje fast endocardial layer conduction speed was reduced in both ventricles, mimicking cellular uncoupling and fibrosis in the Purkinje-endocardial layer, while keeping the bulk tissue conduction speed unaltered. The resulting QRS complexes and activation sequences for a range of Purkinje conductions speeds are shown in Figures 3.7A and 3.7C, respectively. A reduction in R-wave amplitude was identified as a result of the decrease in the Purkinje-endocardial layer speed, together with increases in QRS duration and TAD. The clinical phenotype of R-wave progression loss (Figure 3.7B) was reproduced by a 70% slowing in the Purkinje-endocardial layer (Figure 3.7A, green trace). A functional Purkinje-endocardial layer results in an almost instantaneous activation of the endocardium, followed by transmural propagation, and finally activation of the epicardium (Figure 3.7C, control). Slowing the Purkinje-endocardial layer results in a slowed activation of both the endocardium and epicardium (Figure 3.7C, slow Purkinje CV). In particular, a marked slow conduction in the Purkinje-endocardial system reproduced most of the QRS abnormalities exhibited by the RV_LGE+/TAD+/R+ ACM phenotype, namely QRS duration of over 120 ms, TAD$\geq$55 ms across leads V1-V4, and absence of R-waves in leads V1-V4, yet was unable to match the reduced R-wave to S-wave amplitude ratio observed in the precordial leads QRS complexes of the clinical ECG.
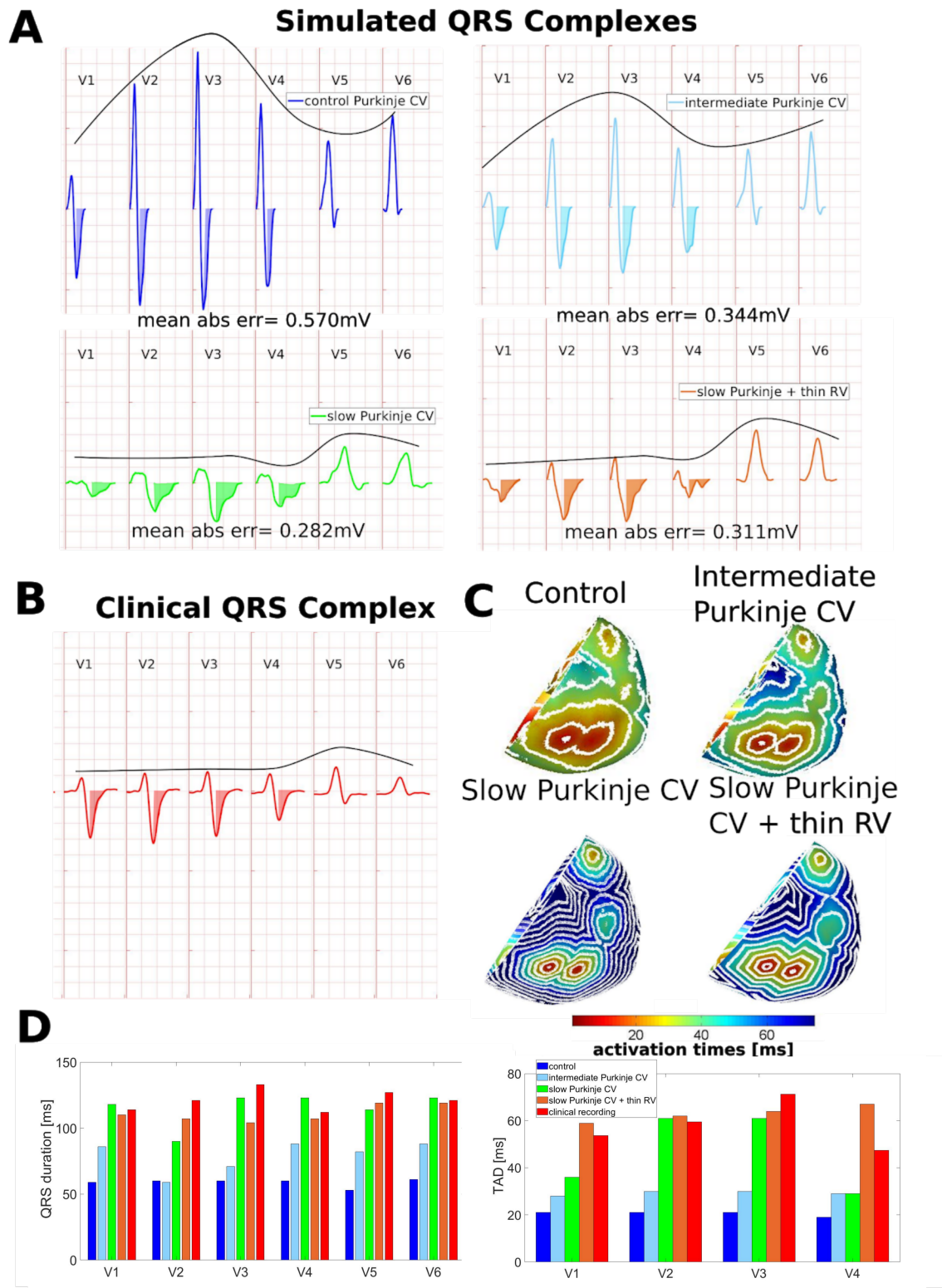
Figure 3.7: Effects of fibrofatty replacement of the His-Purkinje system in the RV_LGE+/TAD+/R+ ACM phenotype.

Figure 3.7: A Simulated QRS complexes in precordial leads for varying Purkinje conduction speeds (control: 0% reduction; intermediate: 35% reduction; slow: 70% reduction) in an otherwise healthy myocardium. The orange trace shows how a reduction in RV wall thickness translates into sharper R-waves, deeper S-waves in V1-V4 and smaller TAD with respect to the slow Purkinje QRS. The black lines show R-wave progression. B. The clinical QRS complex for the RV_LGE+/TAD+/R+ phenotype. C. Activation time maps for the same conditions as in A. D. QRS features of the models in A. Marked slow conduction in the Purkinje system recapitulates the clinical phenotype, including low R-wave amplitudes, absence of R-wave progression, prolonged QRS width and TAD in leads V1-V4, and a prolonged QRS duration in V5-V6. The difference between the simulated (A) and clinical (B) QRS complexes was reported as mean absolute error between pairs of signals.

3.5.2 RV wall myocardial thinning produces deeper S-waves on the anterior/anterolateral leads

The only remaining QRS feature of the RV_LGE+/TAD+/R+ ACM phenotype unexplained by a combination of anatomical and fibrotic remodelling is the observed reduced ratio of R to S-wave amplitudes in anterior/anterolateral leads. Quantitatively, the mean R-wave to S-wave amplitude ratio in leads V1-V4 was 0.42 in the clinical ECG, whilst for the slow conduction Purkinje scenario (Figure 3.7A, green traces) it remained 0.58, suggesting less deep S-wave deflections than in the clinical recordings.

The RV wall thinning observed in the clinical evaluation of the patient was incorporated at this point in the ventricular reconstruction. A reduction of the RV wall thickness from 3 to 2 mm resulted in significantly deeper simulated S-waves and the subsequent decrease in R-wave to S-wave amplitude ratio to 0.37, otherwise preserving the rest of QRS complex features, as shown in Figure 6A (orange trace). This is explained as follows. The transmural activation of the RV wall translates into positive deflections on the ECG as the depolarisation front travels towards the recording electrodes from the endocardial to epicardial layers, producing less prominent R-waves in the thinner myocardium [168]. Once the activation reaches the epicardial surface, it translates into negative deflections as the depolarisation front travels away from the recording electrode. The thicker the RV wall, the longer the transmural depolarisation, effectively contributing to reduce the overall S-wave amplitude because transmural wave propagation will be occurring at the same time as epicardial propagation in different parts of the ventricle. This secondary opposing effect is thus reduced when the RV is thinner, leading to a deeper S-wave morphology. A thin RV

resulted in a shorter QRS complex when the Purkinje conduction was slowed (Figure 3.7D, orange column quantifying QRS duration). The QRS features quantification showed that both the 70% reduced Purkinje-endocardial slowing alone (green bar) and in combination with RV wall thinning (orange bar) lie close to the clinical QRS features (red bar) in Figure 3.7D. The QRS complex duration produced with the slow Purkinje-endocardial layer and thin RV (Figure 3.7 D, orange trace) is reduced in V1, V2 and V4 with respect to when only a slow Purkinje-endocardial layer is considered. This is because some of the latest activating regions appear in the base of the right ventricle, hence reducing the thickness of the RV slightly shortens the total activation time.

3.6   Effect of CV slowing substrates on QRS features

In order to assess the role of each type of remodelling considered on the clinical QRS biomarkers, we compute the Spearman's partial correlation coefficient between model inputs and outputs. By performing a grid search over the degree of Purkinje-endocardial coupling conduction velocity, myocardial LGE scar velocity, whole myocardial tissue conduction velocity and RV tissue conduction velocity and quantifying the precordial QRS complex reconstructed from the simulations, it is possible to infer what is the isolated effect of each of these substrates on the QRS complex and TAD, as well as on the R to S wave amplitudes ratio. The RV was considered as an isolated target for remodelling, as we hypothesise that the anatomical remodelling in the thin RV could translate into cellular uncoupling and reduced conduction velocity due to gap junction dysfunction. Differences in sodium channel densities between the two ventricles have also been highlighted in recent canine studies [169].

The correlations are summarised in Figure 3.8A. When analysing a control simulation without CV slowing substrates for patient RV_LGE+/TAD+/R+, a mean QRS complex duration of 58.9ms across precordial leads is simulated with mean TAD of less than 29.3ms and a mean R-S wave ratio in leads V1-V4 of 0.91. The clinical mean QRS complex duration is 121.3ms across precordial leads, mean TAD is 58.0ms and R-S ratio is 0.43 across V1-V4. A type or combination of remodelling is sought to concommitantly increase QRS complex and TAD, whilst decreasing R to S-wave amplitudes ratio, in order to reproduce the clinical features of the RV_LGE+/TAD+/R+ patient. The simulation results show that reducing myocardial bulk tissue conduction velocity (CV) increases both QRS duration and TAD (Figure 3.8B(left panel)),

yet also increases R-to-S-wave ratio (Figure 3.8C(right panel)). This therefore deviates from the investigated RV_LGE+/TAD+/R+ phenotype (characterised by a low R-to-S-wave amplitude ratio). A reduction in the Purkinje-endocardial layer CV prolongs both the QRS and S-wave TAD duration of the precordial leads, whilst decreasing the R-to-S-wave amplitude ratio. Introducing either LGE-informed or global RV conduction slowing increases QRS duration, yet decreases TAD and increases R-to-S-wave amplitude ratio, deviating from the clinical RV_LGE+/TAD+/R+ QRS phenotype.

In summary, all the types of CV modulating remodelling tested increase QRS duration when a reduction in CV was applied to this specific patient, yet only a reduction of the Purkinje-endocardial CV concomitantly increases TAD and decreases R-to-S wave amplitude ratio. Hence, only the reduction of Purkinje-endocardial layer CV at control levels of bulk myocardial CV could reproduce the RV_LGE+/TAD+/R+ QRS phenotype.

3.7 Discussion

ACM is a complex disease involving desmosomal and gap junction uncoupling, sodium channel downregulation, followed by fibrofatty replacement, leading to conduction delays in the myocardium. The mechanistic basis of the QRS features in this disease remain unclear, especially the factors determining different QRS phenotypes in ACM. This translational modelling study, combining anatomical and structural data from LGE-MRI, explores the mechanistic link between tissue pathophysiology and clinical QRS phenotypes. The main findings of this study are:

- The LV LGE+ ACM phenotype can be fully explained by introducing myocardial fibrosis as informed by LGE-MRI into personalised models of ACM ventricular anatomy. This directly translates into the upper limit of normal QRS duration and TAD in precordial ECG leads.

- The RV LGE+ ACM phenotype, on the contrary, is not explained by myocardial LGE-MRI information alone. This more complex phenotype, characterised on the ECG by severely prolonged QRS width, prolonged TAD, and absence of R-wave progression, further requires a model presenting with fibrotic Purkinje-endocardial conduction system and RV wall thinning to recapitulate its clinical signatures.
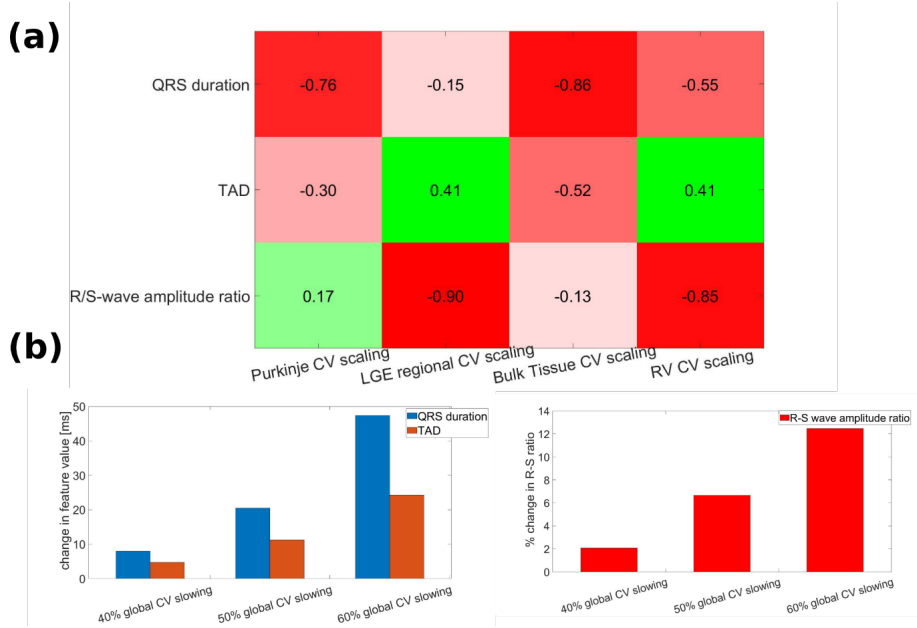
Figure 3.8: Correlation between remodelling and QRS biomarkers. A. Pearson's correlation coefficients between different CV scaling factors and QRS biomarkers. CV was scaled by the factors [0.4, 0.6, 0.8, 1] in each of the types of remodelling, giving rise to a total of 256 bi-ventricular models considered. B. Change in mean QRS duration and mean TAD across precordial leads (left panel), and R-wave to S-wave amplitude ratio (right panel) across leads V1-V4. Results are shown for slowing of the bulk tissue CV in the RV_LGE+/TAD+/R+ ACM ventricular geometry, while keeping the rest of CV scaling factors constant to 1. The left panel shows the increase in QRS duration and TAD as bulk myocardial tissue CV is decreased. The right panel shows that R-to-S-wave amplitude ratio increases when global myocardial CV velocity is decreased, deviating from the RV_LGE+/TAD+/R+ clinical phenotype, which has a lower R-to-S-wave amplitude ratio than the control model.

Conduction abnormalities in ACM are well reflected in the QRS complex, including alterations in its duration, morphology or amplitude [170]. In particular, QRS duration is markedly prolonged in ACM especially in V1-V3, in up to 64% of patients [171]. Within the QRS complex, a protracted TAD has received special attention for diagnosis, as it is present in 47-71% of ACM patients [172] and was confirmed as highly discriminating from other clinical entities [19]. Indeed, both the 2010 Task Force ACM diagnostic criteria [3] and the latest 2019 ACM expert consensus statement [19] consider a TAD≥55 ms as an established ECG diagnostic criteria of ACM. In our results, presence of fibrosis directly translated into moderately protracted QRS duration and TAD in precordial ECG leads.

Poor R-wave progression in precordial leads, in the absence of bundle branch block, is found in 22% of ACM patients [173], and is highlighted as one of the hallmarks of

66

the RV_LGE+/TAD+/R+ phenotype. In this study, we introduce quantitative criteria for diagnosing the absence of R wave progression (R+ phenotype) in ACM, and observe that span the phenotype spectrum of QRS width and TAD values. Our results highlight that a slow Purkinje-endocardial conduction in ACM leads to the loss of precordial R-wave progression. The remodelling of the fast Purkinje-endocardial layer was indeed the only mechanistic factor able to replicate the loss of R-wave progression, low R-wave amplitudes, and extremely prolonged QRS duration and TAD, characterising the RV_LGE+/TAD+/R+ phenotype. Importantly, the Purkinje conduction slowing was found to affect both ventricles equally in the RV_LGE+/TAD+/R+ phenotype. This remodelling is in agreement with previous clinical studies on endocardial activation, suggesting severely prolonged total RV endocardial activation in ACM patients, as measured by 3D electroanatomical mapping [159]. In a separate study, endocardial activation was delayed by 70% with respect to the mean of controls in an ACM cohort without significant structural disease [125], suggesting that Purkinje-endocardial remodelling may precede myocardial fibrosis. Moreover, a dysfunction of the His-Purkinje system was reported in 68% of the hearts (54% with fibrous, 8% with adipose and 5.6% fibrofatty infiltration) in post-mortem studies of 200 ACM-related sudden cardiac deaths [116], which could also explain the endocardial conduction slowing in the electroanatomical mapping studies. In fact, the authors of that study note that Purkinje dysfunction in ACM may have been overlooked and that two thirds of deaths involve Purkinje remodelling, while the main focus so far has been on the RV wall. Different genetic mutations in ACM have been also shown to reduce the expression of connexins 40 and 43 [174] [175], both highly expressed in the His-Purkinje conduction system. This may provide a molecular explanation of the reduced Purkinje-endocardial conduction identified in our study as causal factor for this phenotype.

Finally, RV wall thinning reproduced the low R-wave to S-wave amplitude ratio observed in the RV_LGE+/TAD+/R+ phenotype at the expense of reducing QRS duration. This may be a confounding factor at diagnosis, as patients with increased disease severity, including RV wall thinning, may present with only mild QRS prolongation.

Chapter 4

Conclusions

This study set out to investigate the mechanisms of disease underlying Arrhythmogenic Cardiomyopathy with the idea of furthering mechanistic understanding of disease function using computational and imaging techniques. A vast literature review revealed that few computational studies had investigated ACM and that even going beyond the computational work and into clinical or basic science approaches, ACM remains an understudied entity. Diagnosis is challenging in this clinical entity, with a complex scoring system being employed to diagnose patients. The 12-lead ECG is heavily relied upon for diagnosing ACM and several other diseases such as Brugada Syndrome, Hypertrophic Cardiomyopathy and other Cardiomyopathies have overlapping clinical presentation [176]. Risk stratification is even more difficult, as the disease involves several electrophysiological, structural and geometrical substrates with overlapping features on the QRS complex. The study set out to quantify the contribution of ventricular remodelling to organ level conduction abnormalities and their consequent manifestation on the 12-lead ECG patterns. Ventricular types of remodelling considered in the simulation study include combined effects of channel conductance alterations $I_{Na} - I_{K1}$ on global ventricular conduction velocity, geometrical effects such as RV wall thinning due to uncontrolled apoptosis and RV enlargment on activation sequence dynamics and fibrosis-mediated conduction slowing of the Purkinje-endocardial fast conduction system and of the bulk myocardial tissue. Preliminary simulations in 1D strands setup found that a co-modulation of $I_{Na} - I_{K1}$ in ACM could reduce conduction velocity in tissue by up to 45%. Additional decreases in conduction velocity would therefore be the result of additional coexisting types of remodelling. Patients were assessed in terms of their QRS complex features, namely magnitudes of QRS, TAD and state of R-wave progression across precordial leads. Two distinct ACM patient phenotypes were identified in the medical cohort and their QRS complex features were explained in terms of combinations of different types of

ventricular remodelling. This was achieved by running simulations of sinus rhythm ventricular activation sequence on a personalised ventricular anatomy extracted from MRI images of the patient's ventricles.

The study found that a patient presenting with a long yet physiological QRS complex duration (<100ms) and normal values of TAD (<55ms), as well as with an LGE-MRI localised fibrotic scar in the anterior left ventricular wall was recapitulated by in-silico simulations when introducing 40% conduction slowing in the LV area presenting with fibrotic remodelling and personalising the contact points of the fast running Purkinje tree on the RV endocardial surface. The fibrotic-scar mediated conduction velocity slowing resulted in an increase of the precordial leads QRS complex duration by 25ms and a prolongation in TAD in leads V2-V4 by a similar amount. A more advanced QRS phenotype involving loss of R-wave progression, extremely protracted QRS duration (>120ms) across precordial leads, prolonged TAD (>55ms) across V1-V4 and low R to S-wave amplitudes ratio could not be reproduced in the simulations by introducing only an LGE-informed fibrotic scar, present in the RV anterior wall and RV chamber dilation in this patient. Fibrotic infiltration-mediated conduction slowing of 70% in the fast Purkinje-endocardial conduction layer, alongside 30% RV wall thinning and RV chamber dilation were the substrates required to produce the aforementioned QRS abnormalities in the simulated QRS complexes. Furthermore, the effects on the QRS features as a result of introducing several different types of remodelling were studied using the advanced patient geometry. It was found that reducing global myocardial conduction velocity increased QRS and TAD values yet also increased R to S-wave amplitudes ratio in precordial ECG leads. Decreasing conduction velocity only in the RV led to increases in QRS duration and R to S-wave amplitudes ratio but decreased TAD as it resulted in progressive disappearance of the terminal S-wave. Decreasing conduction in the fibrotic patch in the RV anterior wall was found to increase QRS complex yet also led to disappearance of the S-wave and hence a reduction in TAD and an increase in R to S-wave amplitudes ratio. A global conduction velocity reduction mimicking cell-cell gap juctional remodelling and low $I_{Na} - I_{K1}$ availability was found to increase QRS complex, TAD and R-S wave amplitudes ratio. Merely introducing RV chamber dilation alone resulted in loss of R-wave progression across precordial leads and a complete loss of R-wave in leads V1-V3.

In summary, graph-based personalised ventricular simulations of electrical activation were used to explain two distinct ACM precordial QRS complex phenotypes. The

role of individual and combined tissue level ventricular substrates on the QRS complex features was explored. The computational pipeline presented herein can be used to refine diagnosis non-invasively and quantify the extent of ventricular remodelling present in the ACM ventricles of patients. The work can be embedded into clinical pipelines to stratify risk and guide therapy in ACM and adds confidence in the added value provided by the use of computer simulation techniques in bio-medicine.

Appendix A

Appendix A

A.1 MRI Processing

A.1.1 Construction of MRI-based biventricular meshes

Recently, we presented a computational pipeline for the generation of personalised torso-biventricular meshes from clinical MRI datasets [153] [177]. The first step is to create a surface ventricular mesh from sparse, non-parallel, cross-sectional, non-coincidental, endocardial and epicardial contours, as published in our previous work [153]. The approach uses a composition of smooth approximations towards the maximisation of the data fitting, ensuring a good matching to the input data as well as optimal interpolation characteristics. The pipeline can choose between degree of data fitting and smoothness of the final meshes. The meshes used in this study were produced following the pipeline, presented in Figure A.1 and briefly described below, were obtained using a high degree of Laplacian smoothing in order to mimic heart muscle texture.

The LV epicardium and endocardium, as well as the RV endocardium, were semi-automatically segmented using a digital drawing board and pen. The RV epicardium could not be resolved at this resolution and a uniform wall thickness of 3 mm of the RV wall was assigned, based on a large ex-vivo study of 30 ARVC hearts [167]. This is because the RV wall epicardial surface could not be distinguished from the pericardium in the MRI scans. As the scanner moves towards the apex of the ventricle, the uncertainty in the location of the RV epicardial surface grows as can be seen in Figure A.2. The mean RV wall thickness was reduced to 2 mm when investigating the effects of RV wall thinning. The short axis derived contours were aligned with the horizontal long axis and vertical long axis contours, by minimising the distance at expected intersection points in the plane of the short axis slices.
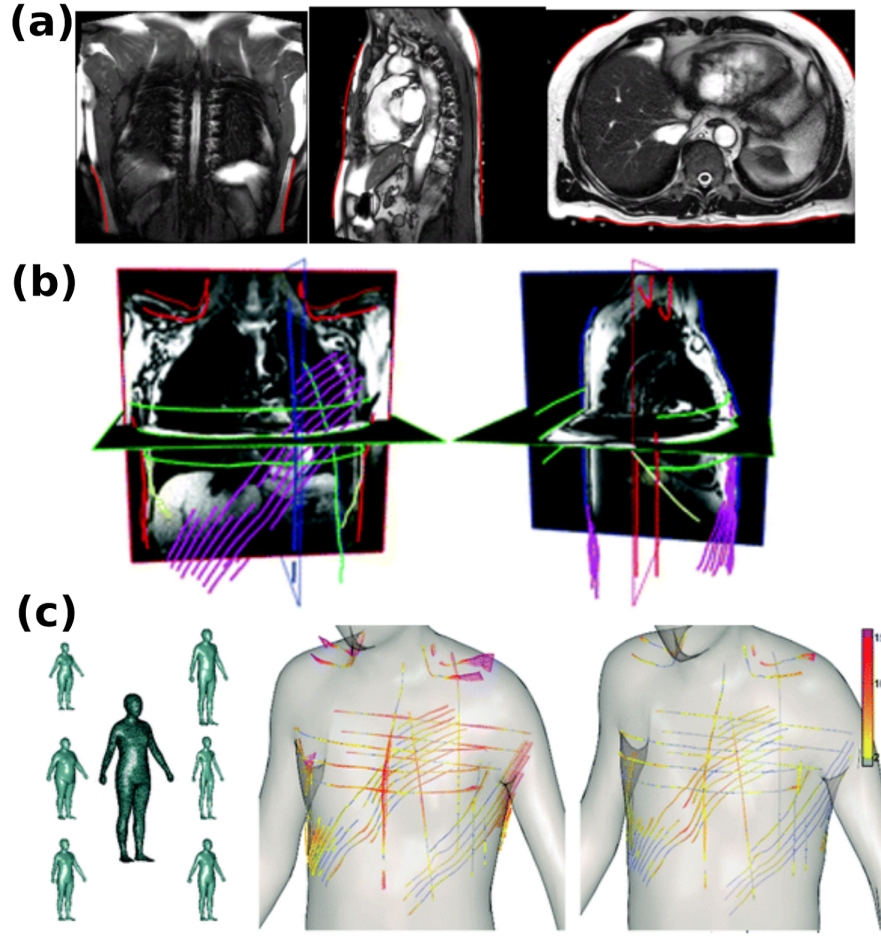
Figure A.1: Computational pipeline from MRI to personalised torso-biventricular meshes. A. Torso segmentation from MRI. The torso of an ACM patient was segmented semi-automatically (in red) by iso-intensity, selecting all points with the same intensity as the torso point selected, then removing any outlier points. B. Distribution of torso contours for an ACM patient, colour-coded by acquisition view (coronal view in red, axial view in green, and short axis view in purple), and overlayed on two MRI images. C. Volumetric torso reconstruction. The original statistical torso model is shown (left), together with the maxima ($+3\sigma'$) and minima (-3σ) of its first 3 principal components, where σ indicates standard deviation. The reconstructed torso is shown after the initial gradient descent fit, and after the subsequent thin plate splines deformation (middle and right panels, respectively). The distance between the mesh and contours was halved as a result. Contours are colour-coded by distance to the nearest mesh point (in millimetres).

Three initial tubular meshes were then created for the LV endocardial, RV endocardial and whole epicardial surfaces. These initial meshes were fitted to the contours using a Thin Plate Splines algorithm [178] [179] which in brief applies small deformations to the mesh and then measures the mean distance between each coarse mesh
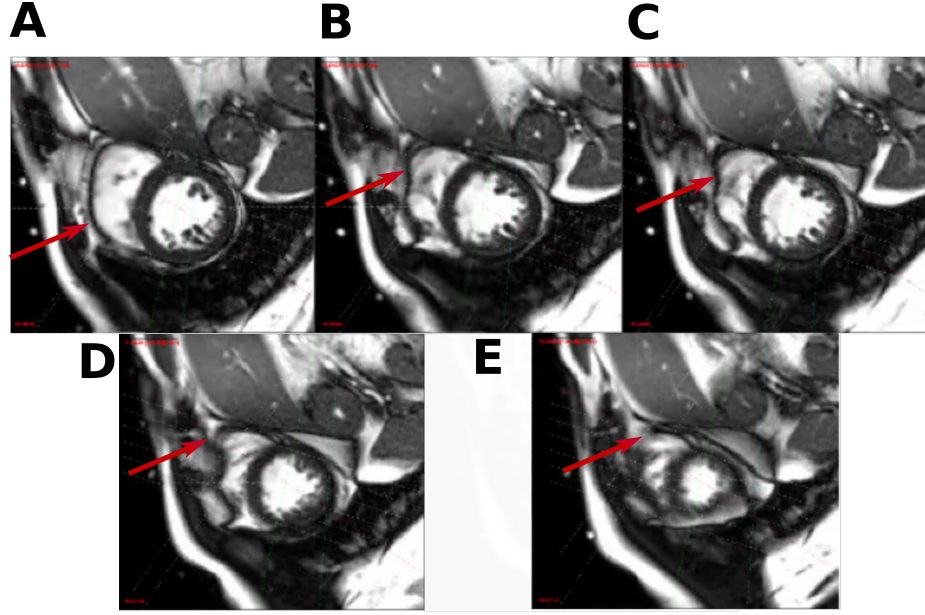
Figure A.2: A-E. Increasing uncertainty in the location of the RV epicardial surface as the scanner moves from the base to the apex of the RV. The red arrow shows the location of the RV wall, visible in A-C in black and the RV wall and surrounding tissue merging in images shown in D-E.

node and the closest contour point. The independent generation of the three surface meshes can lead to intersections of epicardial and endocardial surfaces in certain cases, especially in the thin RV. In that case, the intersecting surfaces are separated using an adaptation of the attractor-based mesh deformation algorithm. Attractor points were added near the intersection between the two surfaces. Epicardial surface points, which lie on the inside of the endocardial surface, become attractor points for the endocardial surface and viceversa. If this process, repeated twice over all intersecting points, was not sufficient to separate the two surfaces, then the endocardial surface still lying on the outer side of the epicardial wall became the epicardial surface and vice versa. Subsequent Laplacian smoothing, decimation and affine transformations ensured the new surface patches are well embedded in the surfaces.

The space in between the surfaces is filled with tetrahedra once the three non-intersecting surfaces were generated. The goal is to achieve regular tetrahedra as this decreases numerical simulation errors [180]. An assessment of two of the most popular tetrahedra-making libraries, namely Gmsh [181]. The space in between the surfaces is filled with tetrahedra once the three non-intersecting surfaces were generated. The goal is to achieve regular tetrahedra as this decreases numerical simulation errors [180]. An assessment of two of the most popular tetrahedra-making libraries, namely

Gmsh [181] and Tetgen [182] was performed. The libraries performed similarly in most quality measures with the exception of the regularity of the tetrahedra created, measured by the ratio between the radii of the smallest possible sphere encompassing a tetrahedron and the largest sphere fitting entirely in it. Using this metric, Gmsh produced more regular tetrahedra and was used for volumetrisation.

There are two major potential sources of uncertainty in the mesh creation pipeline. The first is the introduction of observer bias into the contours. The second source of uncertainty is the accuracy of fitting surfaces to a sparse set of contours. The second source of error was quantified using local uncertainty, defined as the maximum distance between a contour and its nearest mesh surface area element. For our ACM cohort analysed, the mean contour point to mesh node discrepancy was 1.12 mm across the 20 patients. This accuracy of the fitting is illustrated in Figure A.3 for a representative ACM patient, evidencing minimal discrepancy between the contours of two intersecting acquisitions. This discrepancy was minimised by the surface generating algorithm, by choosing the middle ground between contours.
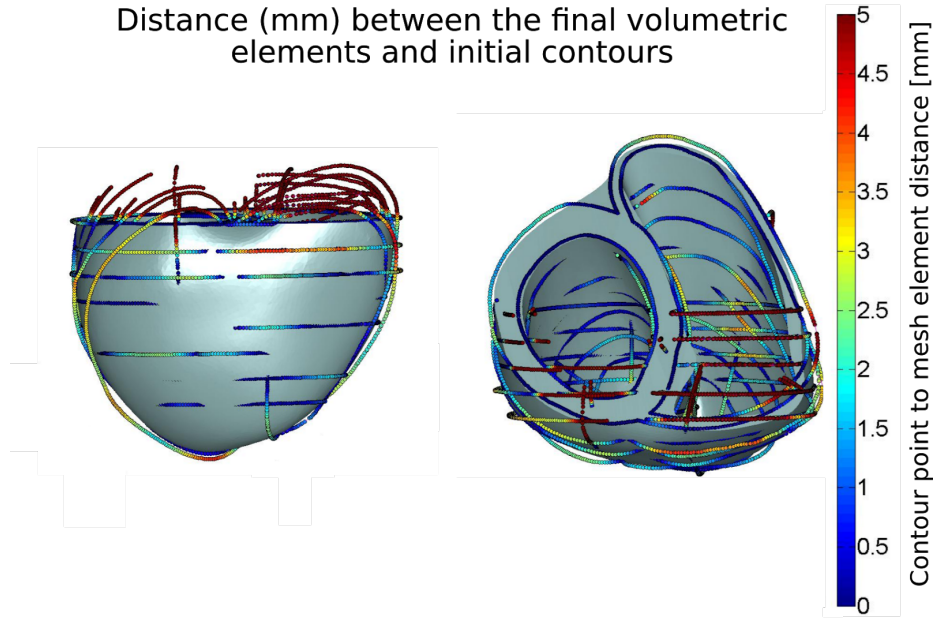

Figure A.3: Final volumetric mesh and initial contours for a representative ACM patient. Contours are colour-coded by distance to the nearest node in the mesh. All contours lie within 5 mm from the final mesh. The mesh is cut at the level of the most basal short axis slice contoured.

A.1.2   Construction of MRI-based torso meshes

Images from the MRI cine stack, as well as the initial localiser slices, were selected and used in the torso contouring process. Slices were segmented in the areas of the shoulders, neck and the torso trunk beneath the arms. A subset of contoured images can be seen in Figure A.1A. Since MRI provides only a sparse set of images, volumetric reconstruction of the torso is challenging. Note the sparsity of the contours in Figure A.1B, which shows the complete contour set for a given patient.

The proposed volumetric construction problem of the torso was solved using previously developed methods [153] [183], by fitting a statistical male torso model (SMTM) generated from 4300 subjects [184] to the contours. After a rigid transformation, the first 40 principal component variations of the SMTM were used to fit the model to the contours. The initialisation of the torso position is in accordance with the position of the previously reconstructed heart from the patient. The optimisation used is a gradient descent-based algorithm, using the root mean square (RMS) distance between contour points and torso as a target function. Following this step, the result of the optimisation algorithm is further deformed by a thin plate spline algorithm, resulting in a halving of the RMS distance, as illustrated in Figure A.1C.

A.1.3   Location of 12-lead ECG electrodes

The electrode locations corresponding to the standard positions of the 12-lead ECG (used in the reconstruction of the QRS complex) were found by mapping the known electrode locations of a torso reconstruction onto the new reconstructed torso of each patient [161]. The mapping between the new patient torso and the torso with known electrode locations was found by means of a co-registration using thin plate splines deformation [185]. Using this mapping, the electrode positions were transferred onto the new torso of the patient.

A.2   Simulation of the electrical activation sequence

A.2.1   Eikonal model of electrical propagation in tissue

In the Eikonal equation, wavefront arrival times t_a in the myocardium ω are described based on a spatially heterogeneous orthotropic velocity function, V(x), and initial activations t_0 at locations γ, which are the connections of the His-Purkinje free running tree (not modelled explicitly here) with the endocardial ventricular surface in our model. The Eikonal equation is given by

$$\sqrt{t_a^T \mathbf{V} \nabla \mathbf{t_a}} = 1 \text{ in } \omega$$

Where

$$t_a = t_0 \text{ in } \gamma$$

where ω is the myocardial muscle and t_a describes the wavefront arrival at location $\mathbf{x}$. The symmetric positive definite velocity tensor $\mathbf{V}(\mathbf{x})$ holds the squared velocities in the transverse, longitudinal and normal fiber directions. These are the equivalent of the conductivities in the more complex bidomain or monodomain formulations of cardiac electrical propagation [160]. The points in γ are the initial activation points which are activated at time t_0. Fibre orientations were assigned using a rule-based algorithm, varying from 60° to −60° in endocardial to epicardial layers with respect to the radial direction [24], based on canine left ventricle ex vivo measurements. In our control model of ventricular activation, anisotropic conduction was considered by assigning longitudinal, transverse and intersheet conduction velocities of 47.8, 31.5 and 29.7 cm/s, respectively, in order to match the activation sequence dynamics of biophysically-detailed models of human ventricular conduction [153] [161].

A.2.2   Purkinje-endocardial root contact point localisation

ECGI was used to inform the Purkinje-endocardial contact points in the RV of the patients, by matching their RV epicardial breakthroughs (Figure A.4). For ECGI, surface potentials were recorded in a previous study [139] at 256 electrode locations on the torso of the patients at resting heart rate, using a portable recording system (ActiveTwo, BioSemi, Netherlands), and used to reconstruct their epicardial break-throughs [139]. The electrodes closest to the standard 12-lead ECG positions, as localised on our torso reconstructions, were selected from the 256 electrode locations to reconstruct the patient clinical ECGs. A high/low pass Butterworth filtering, at 0.5 and 35 Hz frequency cut-offs, were used to remove baseline wandering and high frequency noise, respectively.

A.2.3   Pseudo-ECG calculation

Pseudo-ECGs were derived from ventricular activations using the formula

$$\phi_e(\mathbf{x}') = \mathbf{D} \int_\omega (-\nabla \mathbf{V_m}) . \nabla \frac{\mathbf{1}}{\mathbf{r}} \mathbf{d}\omega$$
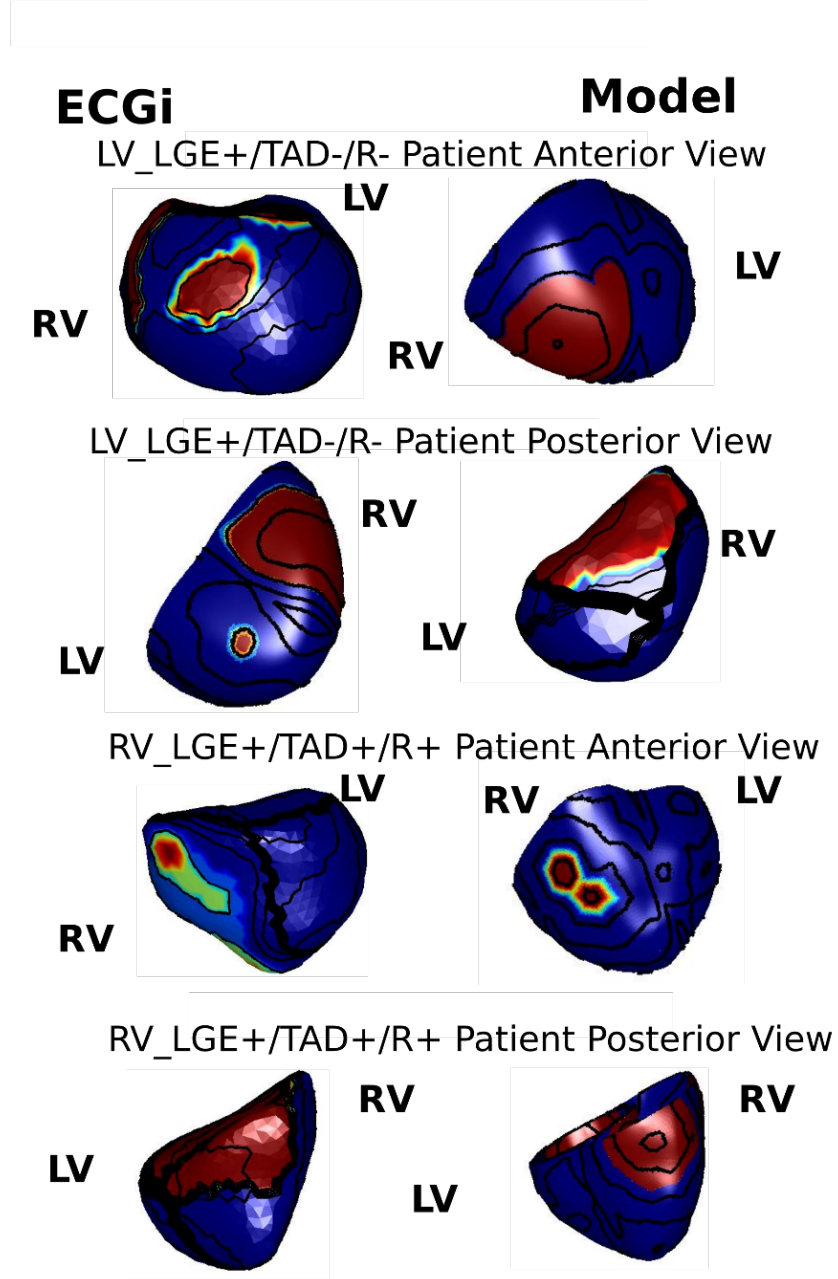
Figure A.4: ECGI-informed placement of Purkinje-endocardial contact points. Left: ECGI epicardial breakthroughs for the representative ACM patients of LV_LGE+/TAD-/R- and RV_LGE+/TAD+/R+ phenotypes, in both anterior and posterior views. Right: resulting epicardial breakthroughs in the control simulation for the same patients.

where D is the diffusion coefficient of the torso, ∇V_m is the spatial gradient of the transmembrane voltage, and r is the Euclidean distance between the electrode position $\mathbf{x}$' and a mesh node $\mathbf{x}$. At each electrode position, the voltage generated by

the ventricles was integrated at a given time and then repeated for all timesteps in the activation sequence, at intervals 1 millisecond apart. The diffusion coefficient D used was 0.1 m^2/s for all the patients studied, as different torso conductivities on the ECG only results into a scaling of the amplitudes [161]. When a myocardial location was stimulated at time t_a, its voltage evolution was approximated by a step function, with resting voltage of -90 mV and an activated voltage of 40 mV.

A.3   LGE-MRI Informed Modelling of Myocardial Fibrosis

LGE-MRI scans were analysed by clinical radiologists as previously published [139], using the Otsu semi-automated technique [186]. The course ECGI mesh were segmented into 21 AHA-style regions by the radiologists [165] and a regional value of fibrosis was specified for each, depending on their fraction of enhanced area. In the LV, pixels of intensity above a given threshold were identified as areas of fibrosis, as previously described [139]. In the RV, as the penetration of the contrast agent is poorer and hence the resolution is lower, the quantification of fibrosis was done visually by two independent experienced radiologists, and for each region either no/some/high contrast was reported. To transfer this information onto the finer simulation meshes (Figure A.5), the coarse and fine meshes were co-registered by the use of anatomical landmarks (centre of the LV and the RV insertion points), using the Thin Spline Deformation algorithm [178].
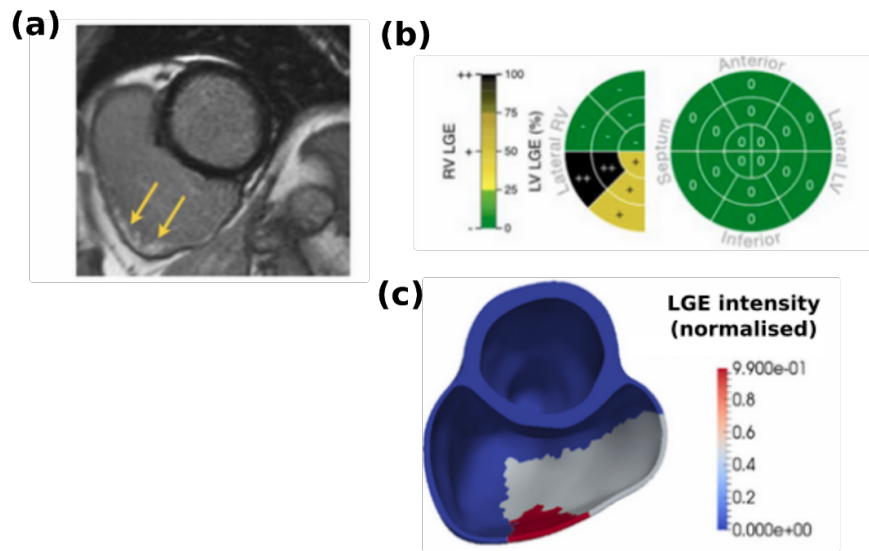
Figure A.5: LGE-MRI data driven models of spatial fibrosis. A. Example of LGE-MRI scan for the representative LV_LGE+/TAD-/R- patient, highlighting a region of fibrosis in the RV free wall. B. Quantification of the AHA-segmented regional level of fibrosis. The lateral free RV wall and the anterior RV are heavily fibrotic. C. Resulting fibrosis region registered in our patient mesh.

Bibliography

[1] M. L. Milstein, H. Musa, D. P. Balbuena, J. M. B. Anumonwo, D. S. Auerbach, P. B. Furspan, L. Hou, B. Hu, S. M. Schumacher, R. Vaidyanathan, J. R. Martens, and J. Jalife, "Dynamic reciprocity of sodium and potassium channel expression in a macromolecular complex controls cardiac excitability and arrhythmia," *Proceedings of the National Academy of Sciences*, vol. 109, pp. E2134–E2143, July 2012.

[2] A. Asimaki, S. Kapoor, E. Plovie, A. Karin Arndt, E. Adams, Z. Liu, C. A. James, D. P. Judge, H. Calkins, J. Churko, J. C. Wu, C. A. MacRae, A. G. Kleber, and J. E. Saffitz, "Identification of a New Modulator of the Intercalated Disc in a Zebrafish Model of Arrhythmogenic Cardiomyopathy," *Science Translational Medicine*, vol. 6, pp. 240ra74–240ra74, June 2014.

[3] F. I. Marcus, W. J. McKenna, D. Sherrill, C. Basso, B. Bauce, D. A. Bluemke, H. Calkins, D. Corrado, M. G. Cox, J. P. Daubert, G. Fontaine, K. Gear, R. Hauer, A. Nava, M. H. Picard, N. Protonotarios, J. E. Saffitz, D. M. Y. Sanborn, J. S. Steinberg, H. Tandri, G. Thiene, J. A. Towbin, A. Tsatsopoulou, T. Wichter, and W. Zareba, "Diagnosis of Arrhythmogenic Right Ventricular Cardiomyopathy/Dysplasia," *Circulation*, vol. 121, no. 13, 2010.

[4] R. Wilders, "Arrhythmogenic right ventricular cardiomyopathy: considerations from in silico experiments.," *Frontiers in physiology*, vol. 3, p. 168, 2012. Publisher: Frontiers Media SA.

[5] F. I. Marcus, G. H. Fontaine, G. Guiraudon, R. Frank, J. L. Laurenceau, C. Malergue, and Y. Grosgogeat, "Right ventricular dysplasia: a report of 24 adult cases.," *Circulation*, vol. 65, pp. 384–98, Feb. 1982.

[6] W. J. Mckenna, G. Thiene, A. Nava, F. Fontaliran, C. Blomstrom-lundqvist, G. Fontaine, F. Camerini, D. Corrado, A. Patologica, B. S. East, and

W. Mckenna, "Diagnosis of arrhythmogenic right ventricular dysplasia / cardiomyopathy," *Br Heart J*, pp. 215–218, 1994.

[7] R. G. Bennett, H. M. Haqqani, A. Berruezo, P. D. Bella, F. E. Marchlinski, C.-J. Hsu, and S. Kumar, "Arrhythmogenic Cardiomyopathy in 2018–2019: ARVC/ALVC or Both?," *Heart, Lung and Circulation*, vol. 28, pp. 164–177, Jan. 2019. Publisher: Elsevier.

[8] C. Gemayel, A. Pelliccia, and P. D. Thompson, "Arrhythmogenic right ventricular cardiomyopathy," *Journal of the American College of Cardiology*, vol. 38, no. 7, pp. 1773–1781, 2001.

[9] B. J. Maron, B. R. Chaitman, M. J. Ackerman, A. Bayés de Luna, D. Corrado, J. E. Crosson, B. J. Deal, D. J. Driscoll, N. M. Estes, C. G. S. Araújo, D. H. Liang, M. J. Mitten, R. J. Myerburg, A. Pelliccia, P. D. Thompson, J. A. Towbin, and S. P. Van Camp, "Recommendations for Physical Activity and Recreational Sports Participation for Young Patients With Genetic Cardiovascular Diseases," *Circulation*, vol. 109, no. 22, 2004.

[10] J. Cadrin-Tourigny, R. Tadros, M. Talajic, L. Rivard, S. Abadir, and P. Khairy, "Risk stratification for sudden death in arrhythmogenic right ventricular cardiomyopathy," *Expert Review of Cardiovascular Therapy*, vol. 13, pp. 653–664, June 2015. Publisher: Informa Healthcare.

[11] D. Corrado, C. Basso, G. Thiene, W. J. McKenna, M. J. Davies, F. Fontaliran, A. Nava, F. Silvestri, C. Blomstrom-Lundqvist, E. K. Wlodarska, G. Fontaine, and F. Camerini, "Spectrum of clinicopathologic manifestations of arrhythmogenic right ventricular cardiomyopathy/dysplasia: a multicenter study.," *Journal of the American College of Cardiology*, vol. 30, pp. 1512–20, Nov. 1997.

[12] G. Fontaine, F. Fontaliran, and R. Frank, "Arrhythmogenic Right Ventricular Cardiomyopathies," *Circulation*, vol. 97, no. 16, 1998.

[13] G. Thiene, A. Nava, D. Corrado, L. Rossi, and N. Pennelli, "Right Ventricular Cardiomyopathy and Sudden Death in Young People," *New England Journal of Medicine*, vol. 318, pp. 129–133, Jan. 1988.

[14] G. Fontaine, F. Fontaliran, R. Frank, G. Chomette, and Y. Grosgogeat, "[Causes of sudden death in athletes].," *Archives des maladies du coeur et des vaisseaux*, pp. 107–11, Aug. 1989.

[15] J. Romero, E. Mejia-Lopez, C. Manrique, and R. Lucariello, "Arrhythmogenic Right Ventricular Cardiomyopathy (ARVC/D): A Systematic Literature Review," *Clinical Medicine Insights. Cardiology*, vol. 7, pp. 97–114, May 2013.

[16] B. Bauce, G. Frigo, F. I. Marcus, C. Basso, A. Rampazzo, F. Maddalena, D. Corrado, M. Winnicki, L. Daliento, I. Rigato, A. Steriotis, E. Mazzotti, G. Thiene, and A. Nava, "Comparison of clinical features of arrhythmogenic right ventricular cardiomyopathy in men versus women," *The American Journal of Cardiology*, vol. 102, pp. 1252–1257, Nov. 2008.

[17] C. Basso, D. Corrado, F. I. Marcus, A. Nava, and G. Thiene, "Arrhythmogenic right ventricular cardiomyopathy," *The Lancet*, vol. 373, no. 9671, pp. 1289–1300, 2009.

[18] D. Corrado, M. S. Link, and H. Calkins, "Arrhythmogenic Right Ventricular Cardiomyopathy," *New England Journal of Medicine*, vol. 376, pp. 61–72, Jan. 2017.

[19] J. A. Towbin, W. J. McKenna, D. J. Abrams, M. J. Ackerman, H. Calkins, F. C. C. Darrieux, J. P. Daubert, C. de Chillou, E. C. DePasquale, M. Y. Desai, N. A. M. Estes III, W. Hua, J. H. Indik, J. Ingles, C. A. James, R. M. John, D. P. Judge, R. Keegan, A. D. Krahn, M. S. Link, F. I. Marcus, C. J. McLeod, L. Mestroni, S. G. Priori, J. E. Saffitz, S. Sanatani, W. Shimizu, J. P. van Tintelen, A. A. M. Wilde, and W. Zareba, "2019 HRS expert consensus statement on evaluation, risk stratification, and management of arrhythmogenic cardiomyopathy," *Heart Rhythm*, vol. 16, pp. e301–e372, Nov. 2019. Publisher: Elsevier.

[20] R. L. Armentano, *Biomechanical Modeling of the Cardiovascular System*. IOP Publishing, 2019.

[21] A. H. Kashou, H. Basit, and L. Chhabra, "Physiology, Sinoatrial Node," in *StatPearls*, Treasure Island (FL): StatPearls Publishing, 2020.

[22] J. Ottesen, M. Olufsen, and J. Larsen, "Applied Mathematical Models in Human Physiology," in *Pflugers Archiv*, vol. 405, Jan. 2004. Journal Abbreviation: Pflugers Archiv.

[23] S. Kanno and J. E. Saffitz, "The role of myocardial gap junctions in electrical conduction and arrhythmogenesis," *Cardiovascular Pathology*, vol. 10, pp. 169–177, July 2001.

[24] D. D. Streeter, H. M. Spotnitz, D. P. Patel, J. Ross, and E. H. Sonnenblick, "Fiber Orientation in the Canine Left Ventricle during Diastole and Systole," *Circulation Research*, vol. 24, pp. 339–347, Mar. 1969.

[25] H. A. Fozzard and W. R. Gibbons, "Action potential and contraction of heart muscle," *American Journal of Cardiology*, vol. 31, pp. 182–192, Feb. 1973. Publisher: Elsevier.

[26] A. O. Grant, "Cardiac Ion Channels," *Circulation: Arrhythmia and Electrophysiology*, vol. 2, pp. 185–194, Apr. 2009. arXiv: 10.1056/NEJM199304293281707 Publisher: Lippincott Williams & Wilkins ISBN: 1941-3149.

[27] C. Antzelevitch and R. Dumaine, "Electrical Heterogeneity in the Heart: Physiological, Pharmacological and Clinical Implications," in *Comprehensive Physiology*, Hoboken, NJ, USA: John Wiley & Sons, Inc., Jan. 2011.

[28] S. M. Bryant, X. Wan, S. J. Shipsey, and G. Hart, "Regional differences in the delayed rectifier current (I(Kr) and I(Ks)) contribute to the differences in action potential duration in basal left ventricular myocytes in guinea-pig," *Cardiovascular Research*, vol. 40, pp. 322–331, Nov. 1998.

[29] M. J. Janse, R. Coronel, T. Opthof, E. A. Sosunov, E. P. Anyukhovsky, and M. R. Rosen, "Repolarization gradients in the intact heart: transmural or apico-basal?," *Progress in biophysics and molecular biology*, vol. 109, pp. 6–15, May 2012.

[30] Eisner David A., Caldwell Jessica L., Kistamás Kornél, and Trafford Andrew W., "Calcium and Excitation-Contraction Coupling in the Heart," *Circulation Research*, vol. 121, pp. 181–195, July 2017. Publisher: American Heart Association.

[31] C. A. Remme and C. R. Bezzina, "REVIEW: Sodium Channel (Dys)Function and Cardiac Arrhythmias," *Cardiovascular Therapeutics*, vol. 28, pp. 287–294, Oct. 2010.

[32] L. Sherwood, *Human physiology : from cells to systems.* Thomson/Brooks/Cole, 2007.

[33] I. Bodi, G. Mikala, S. E. Koch, S. A. Akhter, and A. Schwartz, "The L-type calcium channel in the heart: the beat goes on.," *The Journal of clinical investigation*, vol. 115, pp. 3306–17, Dec. 2005. Publisher: American Society for Clinical Investigation.

[34] W. A. Catterall, "Voltage-Gated Calcium Channels," *Cold Spring Harbor Perspectives in Biology*, vol. 3, pp. a003947–a003947, Aug. 2011.

[35] D. R. Laver and G. D. Lamb, "Inactivation of Ca2+ release channels (ryanodine receptors RyR1 and RyR2) with rapid steps in [Ca2+] and voltage.," *Biophysical journal*, vol. 74, pp. 2352–64, May 1998. Publisher: The Biophysical Society.

[36] J. M. Nerbonne and R. S. Kass, "Molecular Physiology of Cardiac Repolarization," *Physiological Reviews*, vol. 85, no. 4, 2005.

[37] E. Wettwer, G. Amos, J. Gath, H. R. Zerkowski, J. C. Reidemeister, and U. Ravens, "Transient outward current in human and rat ventricular myocytes.," *Cardiovascular research*, vol. 27, pp. 1662–9, Sept. 1993.

[38] E. Wettwer, O. Hála, T. Christ, J. F. Heubach, D. Dobrev, M. Knaut, A. Varró, and U. Ravens, "Role of IKur in Controlling Action Potential Shape and Contractility in the Human Atrium: Influence of Chronic Atrial Fibrillation," *Circulation*, vol. 110, pp. 2299–2306, Oct. 2004.

[39] D. M. Bers, "Cardiac excitation–contraction coupling," *Nature*, vol. 415, pp. 198–205, Jan. 2002.

[40] A. O. Grant, "Cardiac ion channels.," *Circulation. Arrhythmia and electrophysiology*, vol. 2, pp. 185–94, Apr. 2009. Publisher: Lippincott Williams & Wilkins.

[41] M. Periasamy, P. Bhupathy, and G. J. Babu, "Regulation of sarcoplasmic reticulum Ca2+ ATPase pump expression and its relevance to cardiac muscle physiology and pathology," *Cardiovascular Research*, vol. 77, pp. 265–273, Jan. 2008.

[42] M. Vanderheyden, W. T, and e. a. Opthof T, "Molecular aspects of adrenergic modulation of cardiac L-type Ca channels," *Cardiovascular Research*, vol. 65, pp. 28–39, Jan. 2005. Publisher: Oxford University Press.

[43] N. Protonotarios, A. Anastasakis, L. Antoniades, G. Chlouverakis, P. Syrris, C. Basso, A. Asimaki, A. Theopistou, C. Stefanadis, G. Thiene, W. J. McKenna, and A. Tsatsopoulou, "Arrhythmogenic right ventricular cardiomyopathy/dysplasia on the basis of the revised diagnostic criteria in affected families with desmosomal mutations," *European Heart Journal*, vol. 32, pp. 1097–1104, May 2011. Publisher: Oxford Academic.

[44] A. S. te Riele, A. Bhonsale, C. A. James, N. Rastegar, B. Murray, J. R. Burt, C. Tichnell, S. Madhavan, D. P. Judge, D. A. Bluemke, S. L. Zimmerman, I. R. Kamel, H. Calkins, and H. Tandri, "Incremental Value of Cardiac Magnetic Resonance Imaging in Arrhythmic Risk Stratification of Arrhythmogenic Right Ventricular Dysplasia/Cardiomyopathy–Associated Desmosomal Mutation Carriers," *Journal of the American College of Cardiology*, vol. 62, no. 19, pp. 1761–1769, 2013.

[45] A. S. te Riele, C. A. James, N. Rastegar, A. Bhonsale, B. Murray, C. Tichnell, D. P. Judge, D. A. Bluemke, S. L. Zimmerman, I. R. Kamel, H. Calkins, and H. Tandri, "Yield of Serial Evaluation in At-Risk Family Members of Patients With ARVD/C," *Journal of the American College of Cardiology*, vol. 64, no. 3, pp. 293–301, 2014.

[46] C. Kim, J. Wong, J. Wen, S. Wang, C. Wang, S. Spiering, N. G. Kan, S. Forcales, P. L. Puri, T. C. Leone, J. E. Marine, H. Calkins, D. P. Kelly, D. P. Judge, and H.-S. V. Chen, "Studying arrhythmogenic right ventricular dysplasia with patient-specific iPSCs.," *Nature*, vol. 494, pp. 105–10, Feb. 2013.

[47] D. Ma, H. Wei, J. Lu, S. Ho, G. Zhang, X. Sun, Y. Oh, S. H. Tan, M. L. Ng, W. Shim, P. Wong, and R. Liew, "Generation of patient-specific induced pluripotent stem cell-derived cardiomyocytes as a cellular model of arrhythmogenic right ventricular cardiomyopathy," *European Heart Journal*, vol. 34, pp. 1122–1133, Apr. 2013.

[48] K. Takahashi and S. Yamanaka, "Induction of Pluripotent Stem Cells from Mouse Embryonic and Adult Fibroblast Cultures by Defined Factors," *Cell*, vol. 126, pp. 663–676, Aug. 2006.

[49] M. Cerrone, J. Montnach, X. Lin, Y. T. Zhao, M. Zhang, E. Agullo-Pascual, A. Leo-Macias, F. J. Alvarado, I. Dolgalev, T. V. Karathanos, K. Malkani, C. J. Van Opbergen, J. J. Van Bavel, H. Q. Yang, C. Vasquez, D. Tester,

S. Fowler, F. Liang, E. Rothenberg, A. Heguy, G. E. Morley, W. A. Coetzee, N. A. Trayanova, M. J. Ackerman, T. A. Van Veen, H. H. Valdivia, and M. Delmar, "Plakophilin-2 is required for transcription of genes that control calcium cycling and cardiac rhythm," *Nature Communications*, vol. 8, Dec. 2017. Publisher: Nature Publishing Group.

[50] S. Rizzo, E. M. Lodder, A. O. Verkerk, R. Wolswinkel, L. Beekman, K. Pilichou, C. Basso, C. A. Remme, G. Thiene, and C. R. Bezzina, "Intercalated disc abnormalities, reduced Na+ current density, and conduction slowing in desmoglein-2 mutant mice prior to cardiomyopathic changes," *Cardiovascular Research*, vol. 95, pp. 409–418, Sept. 2012.

[51] M. Cerrone, M. Noorman, X. Lin, H. Chkourko, F.-X. Liang, R. van der Nagel, T. Hund, W. Birchmeier, P. Mohler, T. A. van Veen, H. V. van Rijen, and M. Delmar, "Sodium current deficit and arrhythmogenesis in a murine model of plakophilin-2 haploinsufficiency.," *Cardiovascular research*, vol. 95, pp. 460–8, Sept. 2012. Publisher: Oxford University Press.

[52] A. S. te Riele, E. Agullo-Pascual, C. A. James, A. Leo-Macias, M. Cerrone, M. Zhang, X. Lin, B. Lin, N. L. Sobreira, N. Amat-Alarcon, R. F. Marsman, B. Murray, C. Tichnell, J. F. van der Heijden, D. Dooijes, T. A. van Veen, H. Tandri, S. J. Fowler, R. N. Hauer, G. Tomaselli, M. P. van den Berg, M. R. Taylor, F. Brun, G. Sinagra, A. A. Wilde, L. Mestroni, C. R. Bezzina, H. Calkins, J. Peter van Tintelen, L. Bu, M. Delmar, D. P. Judge, and D. P. Judge, "Multilevel analyses of *SCN5A* mutations in arrhythmogenic right ventricular dysplasia/cardiomyopathy suggest non-canonical mechanisms for disease pathogenesis," *Cardiovascular Research*, vol. 113, pp. 102–111, Jan. 2017. Publisher: Oxford University Press.

[53] I. Jóna and P. P. Nánási, "Cardiomyopathies and sudden cardiac death caused by RyR2 mutations: Are the channels the beginning and the end?," *Cardiovascular Research*, vol. 71, no. 3, 2006.

[54] S. O. Marx, S. Reiken, Y. Hisamatsu, T. Jayaraman, D. Burkhoff, N. Rosemblit, and A. R. Marks, "PKA phosphorylation dissociates FKBP12.6 from the calcium release channel (ryanodine receptor): defective regulation in failing hearts.," *Cell*, vol. 101, pp. 365–76, May 2000.

86

[55] M. Yano, K. Ono, T. Ohkusa, M. Suetsugu, M. Kohno, T. Hisaoka, S. Kobayashi, Y. Hisamatsu, T. Yamamoto, M. Kohno, N. Noguchi, S. Takasawa, H. Okamoto, and M. Matsuzaki, "Altered stoichiometry of FKBP12.6 versus ryanodine receptor as a cause of abnormal Ca(2+) leak through ryanodine receptor in heart failure.," *Circulation*, vol. 102, pp. 2131–6, Oct. 2000.

[56] X. H. WEHRENS, S. E. LEHNART, and A. R. MARKS, "Ryanodine Receptor-Targeted Anti-Arrhythmic Therapy," *Annals of the New York Academy of Sciences*, vol. 1047, pp. 366–375, June 2005.

[57] F. Brette, "Calcium polymorphic ventricular tachycardia: a new name for CPVT?," *Cardiovascular research*, vol. 87, pp. 10–1, July 2010. Publisher: Oxford University Press.

[58] X. H. T. Wehrens, S. E. Lehnart, F. Huang, J. A. Vest, S. R. Reiken, P. J. Mohler, J. Sun, S. Guatimosim, L. S. Song, N. Rosemblit, J. M. D'Armiento, C. Napolitano, M. Memmi, S. G. Priori, W. J. Lederer, and A. R. Marks, "FKBP12.6 deficiency and defective calcium release channel (ryanodine receptor) function linked to exercise-induced sudden cardiac death.," *Cell*, vol. 113, pp. 829–40, June 2003.

[59] M. PAUL, M. MEYBORG, P. BOKNIK, U. GERGS, J. GERSS, W. SCHMITZ, G. BREITHARDT, T. WICHTER, and J. NEUMANN, "Autonomic Dysfunction in Patients with Arrhythmogenic Right Ventricular Cardiomyopathy: Biochemical Evidence of Altered Signaling Pathways," *Pacing and Clinical Electrophysiology*, vol. 37, pp. 173–178, Feb. 2014.

[60] P. Rodriguez and E. G. Kranias, "Phospholamban: a key determinant of cardiac function and dysfunction.," *Archives des maladies du coeur et des vaisseaux*, vol. 98, pp. 1239–43, Dec. 2005.

[61] P. A. van der Zwaag, I. A. W. van Rijsingen, A. Asimaki, J. D. H. Jongbloed, D. J. van Veldhuisen, A. C. P. Wiesfeld, M. G. P. J. Cox, L. T. van Lochem, R. A. de Boer, R. M. W. Hofstra, I. Christiaans, K. Y. van Spaendonck-Zwarts, R. H. Lekanne dit Deprez, D. P. Judge, H. Calkins, A. J. H. Suurmeijer, R. N. W. Hauer, J. E. Saffitz, A. A. M. Wilde, M. P. van den Berg, and J. P. van Tintelen, "Phospholamban R14del mutation in patients diagnosed with dilated cardiomyopathy or arrhythmogenic right ventricular cardiomyopathy: evidence supporting the concept of arrhythmogenic cardiomyopathy.," *European journal*

of heart failure, vol. 14, pp. 1199–207, Nov. 2012. Publisher: Oxford University Press.

[62] N. A. Flores, A. N. Botchway, B. M. Stavrou, and D. J. Sheridan, "Cardiac electrophysiological effects of platelet-derived substances.," *Experimental physiology*, vol. 84, no. 2, pp. 253–74, 1999.

[63] S. Cremer, G. Singletary, L. Olsen, K. Wallace, J. H?ggstr?m, I. Ljungvall, K. H?glund, C. Reynolds, N. Pizzinat, and M. Oyama, "Serotonin Concentrations in Platelets, Plasma, Mitral Valve Leaflet, and Left Ventricular Myocardial Tissue in Dogs with Myxomatous Mitral Valve Disease," *Journal of Veterinary Internal Medicine*, vol. 28, pp. 1534–1540, Sept. 2014.

[64] Altun, F. Akın, M. Biteker, N. Köse, G. Güz, F. Öz, Önür, A. K. Bilge, and K. Adalet, "Mean Platelet Volume in Patients with Arrhythmogenic Right Ventricular Cardiomyopathy/Dysplasia," *Haseki Tıp Bülteni*, vol. 53, pp. 303–307, Dec. 2015.

[65] T. J. Craig, F. M. Ashcroft, and P. Proks, "How ATP inhibits the open K(ATP) channel.," *The Journal of general physiology*, vol. 132, pp. 131–44, July 2008. Publisher: The Rockefeller University Press.

[66] P. Bessin, J. Bonnet, D. Apffel, C. Soulard, L. Desgroux, I. Pelas, and J. Benveniste, "Acute circulatory collapse caused by platelet-activating factor (PAF-acether) in dogs," *European Journal of Pharmacology*, vol. 86, pp. 403–413, Jan. 1983.

[67] G. Feuerstein and R. E. Goldstein, "Effect of PAF on the Cardiovascular System," in *Platelet-Activating Factor and Related Lipid Mediators*, pp. 403–424, Boston, MA: Springer US, 1987.

[68] D. S. Damron, D. R. Van Wagoner, C. S. Moravec, and M. Bond, "Arachidonic acid and endothelin potentiate Ca2+ transients in rat cardiac myocytes via inhibition of distinct K+ channels.," *The Journal of biological chemistry*, vol. 268, pp. 27335–44, Dec. 1993.

[69] P. Hoffmann, "Depression of Calcium Dynamics in Cardiac Myocytes-a Common Mechanism of Halogenated Hydrocarbon Anesthetics and Solvents," *Journal of Molecular and Cellular Cardiology*, vol. 26, pp. 579–589, May 1994.

[70] S. Sen-Chowdhry, P. Syrris, and W. J. McKenna, "Genetics of right ventricular cardiomyopathy.," *Journal of cardiovascular electrophysiology*, vol. 16, pp. 927–35, Aug. 2005.

[71] M. M. Awad, H. Calkins, and D. P. Judge, "Mechanisms of disease: molecular genetics of arrhythmogenic right ventricular dysplasia/cardiomyopathy.," *Nature clinical practice. Cardiovascular medicine*, vol. 5, pp. 258–67, May 2008.

[72] D. Corrado, C. Basso, L. Leoni, B. Tokajuk, P. Turrini, B. Bauce, F. Migliore, A. Pavei, G. Tarantini, M. Napodano, A. Ramondo, G. Buja, S. Iliceto, and G. Thiene, "Three-dimensional electroanatomical voltage mapping and histologic evaluation of myocardial substrate in right ventricular outflow tract tachycardia.," *Journal of the American College of Cardiology*, vol. 51, pp. 731–9, Feb. 2008.

[73] C. Kawai, "From Myocarditis to Cardiomyopathy: Mechanisms of Inflammation and Cell Death," *Circulation*, vol. 99, no. 8, 1999.

[74] D. Garrod and M. Chidgey, "Desmosome structure, composition and function," *Biochimica et Biophysica Acta (BBA) - Biomembranes*, vol. 1778, no. 3, pp. 572–587, 2008.

[75] S. Kant, P. Krull, S. Eisner, R. E. Leube, and C. A. Krusche, "Histological and ultrastructural abnormalities in murine desmoglein 2-mutant hearts," *Cell and Tissue Research*, vol. 348, pp. 249–259, May 2012.

[76] K. L. A. Vanderschuren, T. Sieverink, and R. Wilders, "Arrhythmogenic right ventricular dysplasia/cardiomyopathy type 1: a light on molecular mechanisms.," *Genetics research international*, vol. 2013, p. 460805, 2013. Publisher: Hindawi Publishing Corporation.

[77] E. T. Hoorntje, W. P. te Rijdt, C. A. James, K. Pilichou, C. Basso, D. P. Judge, C. R. Bezzina, and J. P. van Tintelen, "Arrhythmogenic cardiomyopathy: pathology, genetics, and concepts in pathogenesis," *Cardiovascular Research*, vol. 113, pp. 1521–1531, Oct. 2017.

[78] R. Ng, H. Manring, N. Papoutsidakis, T. Albertelli, N. Tsai, C. J. See, X. Li, J. Park, T. L. Stevens, P. J. Bobbili, M. Riaz, Y. Ren, C. E. Stoddard, P. M. L. Janssen, T. J. Bunch, S. P. Hall, Y.-C. Lo, D. L. Jacoby, Y. Qyang, N. Wright,

M. A. Ackermann, and S. G. Campbell, "Patient mutations linked to arrhythmogenic cardiomyopathy enhance calpain-mediated desmoplakin degradation," *JCI Insight*, vol. 4, July 2019. Publisher: American Society for Clinical Investigation.

[79] P. J. Scheel, B. Murrary, C. Tichnell, C. James, H. Tandri, H. Calkins, S. P. Chelko, and N. A. Gilotra, "Myocarditis: An Important Presentation of Arrhythmogenic Right Ventricular Cardiomyopathy (ARVC)," *Journal of Cardiac Failure*, vol. 26, pp. S37–S38, Oct. 2020.

[80] J. A. Groeneweg, P. A. van der Zwaag, J. D. Jongbloed, M. G. Cox, A. Vreeker, R. A. de Boer, J. F. van der Heijden, T. A. van Veen, W. J. McKenna, J. P. van Tintelen, D. Dooijes, and R. N. Hauer, "Left-dominant arrhythmogenic cardiomyopathy in a large family: Associated desmosomal or nondesmosomal genotype?," *Heart Rhythm*, vol. 10, pp. 548–559, Apr. 2013.

[81] A. Heuser, E. R. Plovie, P. T. Ellinor, K. S. Grossmann, J. T. Shin, T. Wichter, C. T. Basson, B. B. Lerman, S. Sasse-Klaassen, L. Thierfelder, C. A. MacRae, and B. Gerull, "Mutant Desmocollin-2 Causes Arrhythmogenic Right Ventricular Cardiomyopathy," *The American Journal of Human Genetics*, vol. 79, no. 6, pp. 1081–1088, 2006.

[82] I. Rigato, B. Bauce, A. Rampazzo, A. Zorzi, K. Pilichou, E. Mazzotti, F. Migliore, M. P. Marra, A. Lorenzon, M. De Bortoli, M. Calore, A. Nava, L. Daliento, D. Gregori, S. Iliceto, G. Thiene, C. Basso, and D. Corrado, "Compound and Digenic Heterozygosity Predicts Lifetime Arrhythmic Outcome and Sudden Cardiac Death in Desmosomal Gene-Related Arrhythmogenic Right Ventricular Cardiomyopathy," *Circulation: Cardiovascular Genetics*, vol. 6, pp. 533–542, Dec. 2013.

[83] K. Pilichou, C. A. Remme, C. Basso, M. E. Campian, S. Rizzo, P. Barnett, B. P. Scicluna, B. Bauce, M. J. B. van den Hoff, J. M. T. de Bakker, H. L. Tan, M. Valente, A. Nava, A. A. M. Wilde, A. F. M. Moorman, G. Thiene, and C. R. Bezzina, "Myocyte necrosis underlies progressive myocardial dystrophy in mouse dsg2-related arrhythmogenic right ventricular cardiomyopathy," *The Journal of Experimental Medicine*, vol. 206, pp. 1787–1802, Aug. 2009.

[84] D. Swope, L. Cheng, E. Gao, J. Li, and G. L. Radice, "Loss of cadherin-binding proteins -catenin and plakoglobin in the heart leads to gap junction remodeling

and arrhythmogenesis.," *Molecular and cellular biology*, vol. 32, pp. 1056–67, Mar. 2012. Publisher: American Society for Microbiology (ASM).

[85] R. Lombardi and A. J. Marian, "Arrhythmogenic right ventricular cardiomyopathy is a disease of cardiac stem cells.," *Current opinion in cardiology*, vol. 25, pp. 222–8, May 2010. Publisher: NIH Public Access.

[86] X. Lin, J. Gemel, A. Glass, C. W. Zemlin, E. C. Beyer, and R. D. Veenstra, "Connexin40 and Connexin43 Determine Gating Properties of Atrial Gap Junction Channels," *Journal of molecular and cellular cardiology*, vol. 48, p. 238, Jan. 2010.

[87] D. E. Gutstein, G. E. Morley, D. Vaidya, F. Liu, F. L. Chen, H. Stuhlmann, and G. I. Fishman, "Heterogeneous expression of Gap junction channels in the heart leads to conduction defects and ventricular dysfunction," *Circulation*, vol. 104, pp. 1194–1199, Sept. 2001.

[88] L. M. Fidler, G. J. Wilson, F. Liu, X. Cui, S. W. Scherer, G. P. Taylor, and R. M. Hamilton, "Abnormal connexin43 in arrhythmogenic right ventricular cardiomyopathy caused by plakophilin-2 mutations," *Journal of Cellular and Molecular Medicine*, vol. 13, pp. 4219–4228, Oct. 2009.

[89] V. Bennett and A. J. Baines, "Spectrin and Ankyrin-Based Pathways: Metazoan Inventions for Integrating Cells Into Tissues," *Physiological Reviews*, vol. 81, no. 3, 2001.

[90] P. Y. Sato, W. Coombs, X. Lin, O. Nekrasova, K. J. Green, L. L. Isom, S. M. Taffet, and M. Delmar, "Interactions Between Ankyrin-G, Plakophilin-2, and Connexin43 at the Cardiac Intercalated DiscNovelty and Significance," *Circulation Research*, vol. 109, no. 2, 2011.

[91] D. Corrado and G. Thiene, "Arrhythmogenic Right Ventricular Cardiomyopathy/Dysplasia," *Circulation*, vol. 113, no. 13, 2006.

[92] I. E. A. Li Mura, B. Bauce, A. Nava, M. Fanciulli, G. Vazza, E. Mazzotti, I. Rigato, M. De Bortoli, G. Beffagna, A. Lorenzon, M. Calore, E. Dazzo, C. Nobile, M. L. Mostacciuolo, D. Corrado, C. Basso, L. Daliento, G. Thiene, and A. Rampazzo, "Identification of a PKP2 gene deletion in a family with arrhythmogenic right ventricular cardiomyopathy.," *European journal of human*

genetics : EJHG, vol. 21, pp. 1226–31, Nov. 2013. Publisher: Nature Publishing Group.

[93] M. Hong, L. Bao, E. Kefaloyianni, E. Agullo-Pascual, H. Chkourko, M. Foster, E. Taskin, M. Zhandre, D. A. Reid, E. Rothenberg, M. Delmar, and W. A. Coetzee, "Heterogeneity of ATP-sensitive K+ Channels in Cardiac Myocytes: ENRICHMENT AT THE INTERCALATED DISK," *Journal of Biological Chemistry*, vol. 287, pp. 41258–41267, Nov. 2012.

[94] A. Rampazzo, M. Calore, J. van Hengel, and F. van Roy, "Intercalated Discs and Arrhythmogenic Cardiomyopathy," *Circulation: Cardiovascular Genetics*, vol. 7, no. 6, 2014.

[95] D. Sato, L.-H. Xie, A. A. Sovari, D. X. Tran, N. Morita, F. Xie, H. Karagueuzian, A. Garfinkel, J. N. Weiss, and Z. Qu, "Synchronization of chaotic early afterdepolarizations in the genesis of cardiac arrhythmias.," *Proceedings of the National Academy of Sciences of the United States of America*, vol. 106, pp. 2983–8, Mar. 2009.

[96] M. J. Ackerman, S. G. Priori, S. Willems, C. Berul, R. Brugada, H. Calkins, A. J. Camm, P. T. Ellinor, M. Gollob, R. Hamilton, R. E. Hershberger, D. P. Judge, H. Le Marec, W. J. McKenna, E. Schulze-Bahr, C. Semsarian, J. A. Towbin, H. Watkins, A. Wilde, C. Wolpert, and D. P. Zipes, "HRS/EHRA expert consensus statement on the state of genetic testing for the channelopathies and cardiomyopathies this document was developed as a partnership between the Heart Rhythm Society (HRS) and the European Heart Rhythm Association (EHRA)," *Heart Rhythm*, vol. 8, pp. 1308–1339, Aug. 2011.

[97] M. E. Greene, B. Blumberg, O. W. McBride, H. F. Yi, K. Kronquist, K. Kwan, L. Hsieh, G. Greene, and S. D. Nimer, "Isolation of the human peroxisome proliferator activated receptor gamma cDNA: expression in hematopoietic cells and chromosomal mapping.," *Gene expression*, vol. 4, no. 4-5, pp. 281–99, 1995.

[98] N.-H. Son, T.-S. Park, H. Yamashita, M. Yokoyama, L. A. Huggins, K. Okajima, S. Homma, M. J. Szabolcs, L.-S. Huang, and I. J. Goldberg, "Cardiomyocyte expression of PPARgamma leads to cardiac dysfunction in mice.," *The Journal of clinical investigation*, vol. 117, pp. 2791–801, Oct. 2007. Publisher: American Society for Clinical Investigation.

[99] F. Djouadi, Y. Lecarpentier, J.-L. Hébert, P. Charron, J. Bastin, and C. Coirault, "A potential link between peroxisome proliferator-activated receptor signalling and the pathogenesis of arrhythmogenic right ventricular cardiomyopathy," *Cardiovascular Research*, vol. 84, pp. 83–90, Oct. 2009.

[100] N. Rastegar, A. S. J. M. Te Riele, C. A. James, A. Bhonsale, B. Murray, C. Tichnell, H. Calkins, H. Tandri, D. A. Bluemke, I. R. Kamel, and S. L. Zimmerman, "Fibrofatty Changes: Incidence at Cardiac MR Imaging in Patients with Arrhythmogenic Right Ventricular Dysplasia/Cardiomyopathy," *Radiology*, vol. 280, pp. 405–412, Aug. 2016.

[101] E. Moric, E. Herbert, M. Trusz-Gluza, A. Filipecki, U. Mazurek, and T. Wilczok, "The implications of genetic mutations in the sodium channel gene (SCN5A).," *Europace : European pacing, arrhythmias, and cardiac electrophysiology : journal of the working groups on cardiac pacing, arrhythmias, and cardiac cellular electrophysiology of the European Society of Cardiology*, vol. 5, pp. 325–34, Oct. 2003.

[102] M. Cerrone, "Exercise: A Risky Subject in Arrhythmogenic Cardiomyopathy," *Journal of the American Heart Association*, vol. 7, June 2018.

[103] P. Kong, P. Christia, and N. G. Frangogiannis, "The Pathogenesis of Cardiac Fibrosis," *Cellular and molecular life sciences : CMLS*, vol. 71, pp. 549–574, Feb. 2014.

[104] T. R. Eijgenraam, H. H. W. Silljé, and R. A. de Boer, "Current understanding of fibrosis in genetic cardiomyopathies," *Trends in Cardiovascular Medicine*, vol. 30, pp. 353–361, Aug. 2020.

[105] F. M. Cruz, D. Sanz-Rosa, M. Roche-Molina, J. García-Prieto, J. M. García-Ruiz, G. Pizarro, L. J. Jiménez-Borreguero, M. Torres, A. Bernad, J. Ruíz-Cabello, V. Fuster, B. Ibáñez, and J. A. Bernal, "Exercise triggers ARVC phenotype in mice expressing a disease-causing mutated version of human plakophilin-2," *Journal of the American College of Cardiology*, vol. 65, pp. 1438–1450, Apr. 2015.

[106] S. Weidmann, "Electrical constants of trabecular muscle from mammalian heart.," *The Journal of physiology*, vol. 210, pp. 1041–54, Nov. 1970.

[107] B. Taccardi, B. B. Punske, F. Sachse, X. Tricoche, P. Colli-Franzone, L. F. Pavarino, and C. Zabawa, "Intramural activation and repolarization sequences in canine ventricles. Experimental and simulation studies," *Journal of Electrocardiology*, vol. 38, pp. 131–137, Oct. 2005.

[108] M. Noorman, S. Hakim, E. Kessler, J. A. Groeneweg, M. G. Cox, A. Asimaki, H. V. Van Rijen, L. Van Stuijvenberg, H. Chkourko, M. A. Van Der Heyden, M. A. Vos, N. De Jonge, J. J. Van Der Smagt, D. Dooijes, A. Vink, R. A. De Weger, A. Varro, J. M. De Bakker, J. E. Saffitz, T. J. Hund, P. J. Mohler, M. Delmar, R. N. Hauer, and T. A. Van Veen, "Remodeling of the cardiac sodium channel, connexin43, and plakoglobin at the intercalated disk in patients with arrhythmogenic cardiomyopathy," *Heart Rhythm*, vol. 10, pp. 412–419, Mar. 2013.

[109] X. Chen, L. Chen, Z. Chen, X. Chen, and J. Song, "Remodelling of myocardial intercalated disc protein connexin 43 causes increased susceptibility to malignant arrhythmias in ARVC/D patients," *Forensic Science International*, vol. 275, pp. 14–22, June 2017.

[110] B. C. Eloff, D. L. Lerner, K. A. Yamada, R. B. Schuessler, J. E. Saffitz, and D. S. Rosenbaum, "High resolution optical mapping reveals conduction slowing in connexin43 deficient mice," *Cardiovascular Research*, vol. 51, pp. 681–690, Sept. 2001.

[111] M. Delmar, "Desmosome–Ion Channel Interactions and Their Possible Role in Arrhythmogenic Cardiomyopathy," *Pediatric Cardiology*, vol. 33, pp. 975–979, Aug. 2012.

[112] B. A. Pallante, S. Giovannone, L. Fang-Yu, J. Zhang, N. Liu, G. Kang, W. Dun, P. A. Boyden, and G. I. Fishman, "Contactin-2 Expression in the Cardiac Purkinje Fiber Network," *Circulation. Arrhythmia and electrophysiology*, vol. 3, pp. 186–194, Apr. 2010.

[113] P. Ladenvall, B. Andersson, M. Dellborg, P.-O. Hansson, H. Eriksson, D. Thelle, and P. Eriksson, "Genetic variation at the human connexin 43 locus but not at the connexin 40 locus is associated with left bundle branch block," *Open Heart*, vol. 2, Apr. 2015.

[114] E. L. Kessler, M. Boulaksil, H. V. M. van Rijen, M. A. Vos, and T. A. B. van Veen, "Passive ventricular remodeling in cardiac disease: focus on heterogeneity," *Frontiers in Physiology*, vol. 5, Dec. 2014.

[115] T. P. Nguyen, Z. Qu, and J. N. Weiss, "Cardiac fibrosis and arrhythmogenesis: The road to repair is paved with perils," *Journal of Molecular and Cellular Cardiology*, vol. 70, pp. 83–91, May 2014.

[116] A. Tabib, R. Loire, L. Chalabreysse, D. Meyronnet, A. Miras, D. Malicier, F. Thivolet, P. Chevalier, and P. Bouvagnet, "Circumstances of death and gross and microscopic observations in a series of 200 cases of sudden death associated with arrhythmogenic right ventricular cardiomyopathy and/or dysplasia.," *Circulation*, vol. 108, pp. 3000–3005, Dec. 2003. Place: United States.

[117] H. Cochet, A. Denis, Y. Komatsu, A. S. Jadidi, T. Aït Ali, F. Sacher, N. Derval, J. Relan, M. Sermesant, O. Corneloup, M. Hocini, M. Haïssaguerre, F. Laurent, M. Montaudon, and P. Jaïs, "Automated Quantification of Right Ventricular Fat at Contrast-enhanced Cardiac Multidetector CT in Arrhythmogenic Right Ventricular Cardiomyopathy," *Radiology*, vol. 275, pp. 683–691, Jan. 2015. Publisher: Radiological Society of North America.

[118] R. M. Shaw, "Reduced sodium channels in human ARVC," *Heart rhythm : the official journal of the Heart Rhythm Society*, vol. 10, pp. 420–421, Mar. 2013.

[119] M. Maeder, H. Rickli, C. Sticherling, R. Widmer, and P. Ammann, "Hypokalaemia and sudden cardiac death—lessons from implantable cardioverter defibrillators," *Emergency Medicine Journal : EMJ*, vol. 24, pp. 206–208, Mar. 2007.

[120] K. H. Haugaa, H. Bundgaard, T. Edvardsen, O. Eschen, T. Gilljam, J. Hansen, H. K. Jensen, P. G. Platonov, A. Svensson, and J. H. Svendsen, "Management of patients with Arrhythmogenic Right Ventricular Cardiomyopathy in the Nordic countries," *Scandinavian Cardiovascular Journal*, vol. 49, pp. 299–307, Nov. 2015.

[121] H. Pei, Q. Yu, X. Su, Z. Wang, H. Zhao, D. Yang, Y. Yang, and D. Li, "New Features of Electrocardiogram in a Case Report of Arrhythmogenic Right Ventricular Cardiomyopathy," *Medicine*, vol. 95, Apr. 2016.

[122] Y. Zheng, Y. Xia, J. Carlson, O. Kongstad, and S. Yuan, "Atrial average conduction velocity in patients with and without paroxysmal atrial fibrillation," *Clinical Physiology and Functional Imaging*, Jan. 2016.

[123] P. G. Postema, P. F. van Dessel, J. M. de Bakker, L. R. Dekker, A. C. Linnenbank, M. G. Hoogendijk, R. Coronel, J. G. Tijssen, A. A. Wilde, and H. L. Tan, "Slow and Discontinuous Conduction Conspire in Brugada Syndrome: A Right Ventricular Mapping and Stimulation Study," *Circulation: Arrhythmia and Electrophysiology*, vol. 1, pp. 379–386, Dec. 2008.

[124] J. H. King, C. L.-H. Huang, and J. A. Fraser, "Determinants of myocardial conduction velocity: implications for arrhythmogenesis," *Frontiers in Physiology*, vol. 4, June 2013.

[125] M. C. Finlay, A. K. Ahmed, A. Sugrue, J. Bhar-Amato, G. Quarta, A. Pantazis, E. J. Ciaccio, P. Syrris, S. Sen-Chowdhry, R. Ben-Simon, A. W. Chow, M. D. Lowe, O. R. Segal, W. J. McKenna, and P. D. Lambiase, "Dynamic conduction and repolarisation changes in early arrhythmogenic right ventricular cardiomyopathy versus benign outflow tract ectopy demonstrated by high density mapping & paced surface ECG analysis.," *PloS one*, vol. 9, no. 7, p. e99125, 2014. Publisher: Public Library of Science.

[126] N. Chandra, R. Bastiaenen, M. Papadakis, and S. Sharma, "Sudden Cardiac Death in Young Athletes Practical Challenges and Diagnostic Dilemmas," *JAC*, vol. 61, pp. 1027–1040, 2013.

[127] A. S. Dhamoon and J. Jalife, "The inward rectifier current (IK1) controls cardiac excitability and is involved in arrhythmogenesis," *Heart Rhythm*, vol. 2, pp. 316–324, Mar. 2005.

[128] P. Y. Sato, H. Musa, W. Coombs, G. Guerrero-Serna, G. A. Patiño, S. M. Taffet, L. L. Isom, and M. Delmar, "Loss of Plakophilin-2 Expression Leads to Decreased Sodium Current and Slower Conduction Velocity in Cultured Cardiac Myocytes," *Circulation Research*, vol. 105, no. 6, 2009.

[129] R. Veeraraghavan and S. Poelzing, "Mechanisms underlying increased right ventricular conduction sensitivity to flecainide challenge," *Cardiovascular Research*, vol. 77, pp. 749–756, Mar. 2008.

[130] S. Marx, "Ion channel macromolecular complexes in the heart.," *Journal of molecular and cellular cardiology*, vol. 35, pp. 37–44, Jan. 2003.

[131] V. Y. Sidorov, M. C. Woods, and J. P. Wikswo, "Effects of elevated extracellular potassium on the stimulation mechanism of diastolic cardiac tissue.," *Biophysical journal*, vol. 84, pp. 3470–9, May 2003. Publisher: The Biophysical Society.

[132] Weiss James N., Qu Zhilin, and Shivkumar Kalyanam, "Electrophysiology of Hypokalemia and Hyperkalemia," *Circulation: Arrhythmia and Electrophysiology*, vol. 10, p. e004667, Mar. 2017. Publisher: American Heart Association.

[133] K. Kuwabara, K. Hirata, M. Wake, T. Takahashi, J. Nakazato, N. Yagi, and A. Fukuyama, "A case of arrhythmogenic right ventricular cardiomyopathy presenting with progressive right ventricular failure and recurrent multifocal monomorphic ventricular tachycardia during 15 years of follow-up," *Journal of Cardiology Cases*, vol. 10, pp. 216–220, Dec. 2014.

[134] S. Dutta, K. C. Chang, K. A. Beattie, J. Sheng, P. N. Tran, W. W. Wu, M. Wu, D. G. Strauss, T. Colatsky, and Z. Li, "Optimization of an In silico Cardiac Cell Model for Proarrhythmia Risk Assessment," *Frontiers in Physiology*, vol. 8, p. 616, 2017.

[135] R. E. Kerber, M. G. Kienzle, B. Olshansky, A. L. Waldo, D. Wilber, M. D. Carlson, A. M. Aschoff, S. Birger, L. Fugatt, and S. Walsh, "Ventricular tachycardia rate and morphology determine energy and current requirements for transthoracic cardioversion.," *Circulation*, vol. 85, pp. 158–163, Jan. 1992.

[136] M. L. Milstein, H. Musa, D. P. Balbuena, J. M. B. Anumonwo, D. S. Auerbach, P. B. Furspan, L. Hou, B. Hu, S. M. Schumacher, R. Vaidyanathan, J. R. Martens, and J. Jalife, "Dynamic reciprocity of sodium and potassium channel expression in a macromolecular complex controls cardiac excitability and arrhythmia," p. 10.

[137] M. V. Lima, M. E. Ochiai, J. N. Cardoso, P. C. Morgado, R. T. Munhoz, and A. C. P. Barretto, "Hyperkalemia during spironolactone use in patients with decompensated heart failure," *Arquivos Brasileiros de Cardiologia*, vol. 91, pp. 194–199, Sept. 2008. Publisher: Arquivos Brasileiros de Cardiologia.

[138] V. M. Campese and G. Adenuga, "Electrophysiological and clinical consequences of hyperkalemia," *Kidney International Supplements*, vol. 6, pp. 16–19, 2016.

[139] C. M. Andrews, N. T. Srinivasan, S. Rosmini, H. Bulluck, M. Orini, S. Jenkins, A. Pantazis, W. J. McKenna, J. C. Moon, P. D. Lambiase, and Y. Rudy, "The Electrical and Structural Substrate of Arrhythmogenic Right Ventricular Cardiomyopathy Determined Using Noninvasive Electrocardiographic Imaging and Late Gadolinium Magnetic Resonance Imaging," *Circulation. Arrhythmia and electrophysiology*, vol. 10, July 2017.

[140] D. U. Jeong and K. M. Lim, "The effect of myocardial action potential duration on cardiac pumping efficacy: a computational study," *BioMedical Engineering OnLine*, vol. 17, p. 79, June 2018.

[141] O. E. Osadchii, "Mechanisms of hypokalemia-induced ventricular arrhythmogenicity," *Fundamental & Clinical Pharmacology*, vol. 24, pp. 547–559, June 2010.

[142] F. O. Campos, J. Whitaker, R. Neji, S. Roujol, M. O'Neill, G. Plank, and M. J. Bishop, "Factors Promoting Conduction Slowing as Substrates for Block and Reentry in Infarcted Hearts," *Biophysical Journal*, vol. 117, pp. 2361–2374, Dec. 2019.

[143] J. Heijman and D. Dobrev, "Ion channels as part of macromolecular multiprotein complexes," *Herzschrittmachertherapie + Elektrophysiologie*, vol. 29, pp. 30–35, Mar. 2018.

[144] M. Cerrone and M. Delmar, "Desmosomes and the sodium channel complex: Implications for arrhythmogenic cardiomyopathy and Brugada syndrome," *Trends in Cardiovascular Medicine*, vol. 24, pp. 184–190, July 2014.

[145] Dominguez Graciela and Fozzard Harry A., "Influence of Extracellular K+ Concentration on Cable Properties and Excitability of Sheep Cardiac Purkinje Fibers," *Circulation Research*, vol. 26, pp. 565–574, May 1970. Publisher: American Heart Association.

[146] R. M. Shaw and Y. Rudy, "Ionic mechanisms of propagation in cardiac tissue. Roles of the sodium and L-type calcium currents during reduced excitability and decreased gap junction coupling," *Circulation Research*, vol. 81, pp. 727–741, Nov. 1997.

[147] R. Veeraraghavan, R. G. Gourdie, and S. Poelzing, "Mechanisms of cardiac conduction: a history of revisions," *American Journal of Physiology - Heart and Circulatory Physiology*, vol. 306, pp. H619–H627, Mar. 2014.

[148] D. Corrado, T. Wichter, M. S. Link, R. N. W. Hauer, F. E. Marchlinski, A. Anastasakis, B. Bauce, C. Basso, C. Brunckhorst, A. Tsatsopoulou, H. Tandri, M. Paul, C. Schmied, A. Pelliccia, F. Duru, N. Protonotarios, N. M. Estes, W. J. McKenna, G. Thiene, F. I. Marcus, H. Calkins, and H. Calkins, "Treatment of Arrhythmogenic Right Ventricular Cardiomyopathy/Dysplasia: An International Task Force Consensus Statement.," *Circulation*, vol. 132, pp. 441–53, Aug. 2015. Publisher: Wolters Kluwer Health.

[149] R. Jain, D. Dalal, A. Daly, C. Tichnell, C. James, A. Evenson, R. Jain, T. Abraham, B. Y. Tan, H. Tandri, S. D. Russell, D. Judge, and H. Calkins, "Electrocardiographic features of arrhythmogenic right ventricular dysplasia.," *Circulation*, vol. 120, pp. 477–487, Aug. 2009. Place: United States.

[150] M. Motevali, Z. Siahi, A. Mohammadzadeh, and A. Sangi, "Cardiac Magnetic Resonance Imaging (MRI) Findings in Arrhythmogenic Right Ventricular Dysplasia (ARVD) Compared with Echocardiography," *Medical Sciences*, vol. 6, p. 80, Sept. 2018. Publisher: MDPI AG.

[151] S. Rizzo, E. Carturan, M. De Gaspari, K. Pilichou, G. Thiene, and C. Basso, "Update on cardiomyopathies and sudden cardiac death," *Forensic Sciences Research*, vol. 4, pp. 202–210, July 2019.

[152] A. Lyon, A. Bueno-Orovio, E. Zacur, R. Ariga, V. Grau, S. Neubauer, H. Watkins, B. Rodriguez, and A. Mincholé, "Electrocardiogram phenotypes in hypertrophic cardiomyopathy caused by distinct mechanisms: apico-basal repolarization gradients vs. Purkinje-myocardial coupling abnormalities," *EP Europace*, vol. 20, pp. iii102–iii112, Nov. 2018.

[153] A. Mincholé, E. Zacur, R. Ariga, V. Grau, and B. Rodriguez, "MRI-Based Computational Torso/Biventricular Multiscale Models to Investigate the Impact of Anatomical Variability on the ECG QRS Complex," *Frontiers in Physiology*, vol. 10, 2019.

[154] M. Favino, S. Pozzi, S. Pezzuto, F. W. Prinzen, A. Auricchio, and R. Krause, "Impact of mechanical deformation on pseudo-ECG: a simulation study," *EP Europace*, vol. 18, no. suppl_4, pp. iv77–iv84, 2016.

[155] A. Loewe, W. H. W. Schulze, Y. Jiang, M. Wilhelms, A. Luik, O. Dössel, and G. Seemann, "ECG-Based Detection of Early Myocardial Ischemia in a Computational Model: Impact of Additional Electrodes, Optimal Placement, and a New Feature for ST Deviation," *BioMed Research International*, vol. 2015, p. 530352, Oct. 2015.

[156] C. Sánchez, G. D'Ambrosio, F. Maffessanti, E. G. Caiani, F. W. Prinzen, R. Krause, A. Auricchio, and M. Potse, "Sensitivity analysis of ventricular activation and electrocardiogram in tailored models of heart-failure patients," *Medical & Biological Engineering & Computing*, vol. 56, pp. 491–504, Mar. 2018.

[157] T. P. Mast, A. J. Teske, J. Walmsley, J. F. van der Heijden, R. van Es, F. W. Prinzen, T. Delhaas, T. A. van Veen, P. Loh, P. A. Doevendans, M. J. Cramer, and J. Lumens, "Right Ventricular Imaging and Computer Simulation for Electromechanical Substrate Characterization in Arrhythmogenic Right Ventricular Cardiomyopathy," *Journal of the American College of Cardiology*, vol. 68, pp. 2185–2197, Nov. 2016. Publisher: Elsevier USA.

[158] J. Walmsley, W. van Everdingen, M. J. Cramer, F. W. Prinzen, T. Delhaas, and J. Lumens, "Combining computer modelling and cardiac imaging to understand right ventricular pump function," *Cardiovascular Research*, vol. 113, pp. 1486–1498, Oct. 2017.

[159] H. Tandri, A. Asimaki, T. Abraham, D. Dalal, L. Tops, R. Jain, J. E. Saffitz, D. P. Judge, S. D. Russell, M. Halushka, D. A. Bluemke, D. A. Kass, and H. Calkins, "Prolonged RV endocardial activation duration: a novel marker of arrhythmogenic right ventricular dysplasia/cardiomyopathy.," *Heart rhythm*, vol. 6, pp. 769–775, June 2009.

[160] M. Wallman, N. P. Smith, and B. Rodriguez, "A comparative study of graph-based, eikonal, and monodomain simulations for the estimation of cardiac activation times," *IEEE Transactions on Biomedical Engineering*, vol. 59, no. 6, pp. 1739–1748, 2012.

[161] L. Cardone-Noott, A. Bueno-Orovio, A. Mincholé, N. Zemzemi, and B. Rodriguez, "Human ventricular activation sequence and the simulation of the electrocardiographic QRS complex and its variability in healthy and intraventricular block conditions," *Europace*, vol. 120, pp. 179–88, Dec. 2016. Publisher: Springer, New York, NY.

[162] H. Martinez-Navarro, A. Mincholé, A. Bueno-Orovio, and B. Rodriguez, "High arrhythmic risk in antero-septal acute myocardial ischemia is explained by increased transmural reentry occurrence," *Scientific Reports*, vol. 9, no. 1, p. 16803, 2019. Publisher: Nature Publishing Group.

[163] D. Durrer, R. T. van Dam, G. E. Freud, M. J. Janse, F. L. Meijler, and R. C. Arzbaecher, "Total excitation of the isolated human heart.," *Circulation*, vol. 41, pp. 899–912, June 1970.

[164] N. Kudryashova, V. Tsvelaya, K. Agladze, and A. Panfilov, "Virtual cardiac monolayers for electrical wave propagation," *Scientific Reports*, vol. 7, p. 7887, Dec. 2017.

[165] S. Oeltze-Jafra, A. Kuß, F. Grothues, A. Hennemuth, and B. Preim, "Integrated Visualization of Morphologic and Perfusion Data for the Analysis of Coronary Artery Disease," pp. 131–138, Jan. 2006.

[166] J. H. King, C. L.-H. Huang, and J. A. Fraser, "Determinants of myocardial conduction velocity: implications for arrhythmogenesis.," *Frontiers in physiology*, vol. 4, p. 154, 2013. Publisher: Frontiers Media SA.

[167] C. Basso, G. Thiene, D. Corrado, A. Angelini, A. Nava, and M. Valente, "Arrhythmogenic Right Ventricular Cardiomyopathy," *Circulation*, vol. 94, no. 5, pp. 983–991, 1996.

[168] J. N. Euan Ashley, *Cardiology Explained*. Remedica, 2004.

[169] K. Calloe, G. L. Aistrup, J. M. Di Diego, R. J. Goodrow, J. A. Treat, and J. M. Cordeiro, "Interventricular differences in sodium current and its potential role in Brugada syndrome.," *Physiological reports*, vol. 6, p. e13787, July 2018. Place: United States.

[170] K. Nasir, C. Bomma, H. Tandri, A. Roguin, D. Dalal, K. Prakasa, C. Tichnell, C. James, P. Jspevak, F. Marcus, H. Calkins, and H. Calkins, "Electrocardiographic Features of Arrhythmogenic Right Ventricular Dysplasia/Cardiomyopathy According to Disease Severity," *Circulation*, vol. 110, pp. 1527–1534, Sept. 2004.

[171] H. U. H. Virk, S. Farooq, A. R. Ghani, and S. Arora, "QRS fragmentation: its role in sherlocking the arrhythmogenic heart," *Journal of Community Hospital Internal Medicine Perspectives*, vol. 6, July 2016.

[172] T. Mast, A. Teske, A. te Riele, J. Groeneweg, J. Van der Heijden, B. Velthuis, P. Loh, P. Doevendans, T. van Veen, D. Dooijes, J. Bakker, R. Hauer, and M.-J. Cramer, "Prolonged Electromechanical Interval Unmasks Arrhythmogenic Right Ventricular Dysplasia/Cardiomyopathy in the Subclinical Stage," *Journal of cardiovascular electrophysiology*, vol. 27, Nov. 2015.

[173] A. K. Steriotis, B. Bauce, L. Daliento, I. Rigato, E. Mazzotti, A. F. Folino, M. P. Marra, L. Brugnaro, and A. Nava, "Electrocardiographic pattern in arrhythmogenic right ventricular cardiomyopathy.," *The American journal of cardiology*, vol. 103, pp. 1302–1308, May 2009. Place: United States.

[174] R. C. Lyon, V. Mezzano, A. T. Wright, E. Pfeiffer, J. Chuang, K. Banares, A. Castaneda, K. Ouyang, L. Cui, R. Contu, Y. Gu, S. M. Evans, J. H. Omens, K. L. Peterson, A. D. McCulloch, and F. Sheikh, "Connexin defects underlie arrhythmogenic right ventricular cardiomyopathy in a novel mouse model.," *Human molecular genetics*, vol. 23, pp. 1134–1150, Mar. 2014.

[175] R. Joshi-Mukherjee, W. Coombs, H. Musa, E. Oxford, S. Taffet, and M. Delmar, "Characterization of the molecular phenotype of two ARVC-related PKP2 mutations," *Heart rhythm : the official journal of the Heart Rhythm Society*, vol. 5, pp. 1715–1723, Dec. 2008.

[176] K. H. Haugaa and I. S. Leren, "Prevalence, Clinical Presentation, and Management of Channelopathies and Cardiomyopathies, Long QT Syndrome, Brugada Syndrome, Arrhythmogenic Cardiomyopathy, and Hypertrophic Cardiomyopathy," *Current Cardiovascular Risk Reports*, vol. 13, p. 16, May 2019.

[177] B. Villard, V. Carapella, R. Ariga, V. Grau, and E. Zacur, "Cardiac Mesh Reconstruction from Sparse, Heterogeneous Contours," in *Medical Image Understanding and Analysis* (M. Valdés Hernández and V. González-Castro, eds.), Communications in Computer and Information Science, (Cham), pp. 169–181, Springer International Publishing, 2017.

[178] R. Sprengel, K. Rohr, and H. Stiehl, "Thin-plate spline approximation for image registration," in *Proceedings of 18th Annual International Conference of the IEEE Engineering in Medicine and Biology Society*, vol. 3, pp. 1190–1191, IEEE.

[179] K. Rohr, H. Stiehl, R. Sprengel, T. Buzug, J. Weese, and M. Kuhn, "Landmark-based elastic registration using approximating thin-plate splines," *IEEE Transactions on Medical Imaging*, vol. 20, pp. 526–534, June 2001.

[180] J. Dardenne, N. Siauve, S. Valette, R. Prost, and N. Burais, "Impact of Tetra-hedral Mesh Quality for Electromagnetic and Thermal Simulations," p. 1044, Nov. 2009.

[181] C. Geuzaine and J.-F. Remacle, "Gmsh: A 3-D finite element mesh generator with built-in pre- and post-processing facilities," *International Journal for Numerical Methods in Engineering*, vol. 79, pp. 1309–1331, Sept. 2009. Publisher: John Wiley & Sons, Ltd.

[182] L. Pishchulin, S. Wuhrer, T. Helten, C. Theobalt, and B. Schiele, "Building statistical shape spaces for 3D human modeling," *Pattern Recognition*, vol. 67, pp. 276–286, July 2017. Publisher: Pergamon.

[183] B. Villard, V. Carapella, R. Ariga, V. Grau, and E. Zacur, "Cardiac Mesh Reconstruction from Sparse, Heterogeneous Contours," pp. 169–181, Springer, Cham, 2017.

[184] E. Zacur, A. Minchole, B. Villard, V. Carapella, R. Ariga, B. Rodriguez, and V. Grau, *MRI-based heart and torso personalization for computer modeling and simulation of cardiac electrophysiology*, vol. 10549. Springer, Cham, 2017. ISSN: 0302-9743.

[185] S. Rohr, "Role of gap junctions in the propagation of the cardiac action potential.," *Cardiovascular research*, vol. 62, pp. 309–22, May 2004.

[186] N. Otsu, "A Threshold Selection Method from Gray-Level Histograms," *IEEE Transactions on Systems, Man, and Cybernetics*, vol. 9, pp. 62–66, Jan. 1979.